Title

A MEASUREMENT OF THE MAGNETIC DIPOLE MOMENT OF THE A ++ (1232) FROM THE BREMSSTRAHLUNG PROCESS n p ->npr

Permalink

https://escholarship.org/uc/item/9bw9x262

Author

Meyer, C.A.

Publication Date

1987-06-01

LBL-23688

c.2

Lawrence Berkeley Laboratory
UNIVERSITY OF CALIFORNIA

A MEASUREMENT OF THE MAGNETIC DIPOLE MOMENT OF THE $\Delta^{++}(1232)$ FROM THE BREMSSTRAHLUNG PROCESS $\pi p \rightarrow \pi p \gamma$

C.A. Meyer
(Ph.D. Thesis)

June 1987

NUCLEAR SCIENCE DIVISION

Prepared for the U.S. Department of Energy under Contract DE-AC03-76SF00098

DISCLAIMER

A Measurement of the Magnetic Dipole Moment of the $\Delta^{++}(1232)$ from the Bremsstrahlung Process $\pi p \rightarrow \pi p \gamma$

Curtis Anthony Meyer

Ph.D. Thesis

Lawrence Berkeley Laboratory
University of California
Berkeley, California 94720

June 1987

This work was supported by the Director, Office of Energy Research, Division of Nuclear Physics of the Office of High Energy and Nuclear Physics of the U.S. Department of Energy under Contracts DE-AC03-76SF00098 and DE-AS03-81ER40004.

Abstract

We have measured the cross–section $\frac{d^5\sigma}{d\Omega_\pi d\Omega_\gamma dE_\gamma}$ from the bremsstrahlung process $\pi^+\mathrm{p} \rightarrow \pi^+\mathrm{p}\gamma$ for incident pions of energy 299MeV. We detected the out going pion in the angular range from 55° to 95° in the lab, and photons were detected near 240° in the lab. We compare this measured cross–section to the MIT theory[1] in order to extract a measurement of the magnetic dipole moment of the $\Delta^{++}(1232)$, μ_Δ. In order to compare our results with the MIT theory, we have folded the MIT theory into the acceptance of our apparatus. We find that for pion angles between 55° and 75° the theory gives us a dipole moment of:

$$2.3\mu_p < \mu_\Delta < 3.3\mu_p$$

where the quoted error arises from an experimental uncertainty of $\pm 0.25\mu_p$ and from theoretical uncertainties[2] of $\pm 0.25\mu_p$. However, for pion angles between 75° and 95° we find that the MIT theory predicts a cross–section which is larger than our measured cross–section ,and makes it difficult to extract a value of μ_Δ. This over prediction is not understood, but consistent with a similar effect when the MIT theory is fit to previous data.

---

[1] L. Heller, S. Kumano, J.C. Martinez and E.J. Moniz, **Phys. Rev. C35**, 718 (1987).

[2] Because of the nature of the theoretical uncertainties, it is necessary that they be added linearly with the experimental error.

Contents

List of Figures

List of Tables

Acknowledgements

I have placed this acknowledgement at the beginning of my thesis to make sure that all of those people that have made contributions are recognized. It would not seem fair if the reader never got far enough in reading this thesis to see the people that deserve thanks and mentioning.

First there are my collaborators on this experiment without whose help this experiment could not have been done. I wish to thank C. Amsler, J. Bistirlich, A. Bosshard, K.M. Crowe, M. Doebeli[1], M. Doser, R.P. Haddock, S. Ljungfelt, J.F. Loude, J.P. Perroud, D. Renker, J. Riedlberger, M. Schaad, D. Sober, U. Straumann, P. Truöl and L. van Elmbt for all of their efforts in the running of this experiment, and analysis of this experiment. I also want to express appreciation to the Swiss Armed Forces for keeping the lab safe from invasion[2] during several of our runs.

I also want to especially thank my thesis advisor Ken Crowe. Ken took me off the street of first year graduate students and turned me into an experimental physicist. Working in Ken's group has been both a pleasure and a challenge. It exposed me to many different experiments, and many different people, and challenged me to do the most that I could.

Amongst the collaborators on the experiment, I want to thank Peter Truöl. I felt quite fortunate in having been able to work with Peter, and have always been amazed at how quickly he can arrive at an essentially correct answer with very little work. The most important thing that I feel I've learned from Peter is before you go and apply the obvious brute force solution, think about it for awhile. I also enjoyed many dinners and beers with Peter while at SIN.

I also want to thank Andreas Bosshard, the other graduate student on this experiment.

---

[1] I especially want to thank Max for keeping Switzerland safe during the Chernobel accident.

[2] It is not clear from whom they were protecting us, but they were certainly doing a bang-up job of it.

Andreas was responsible for getting the hardware converted to that which we used in the experiment, a task for which I thank him profusely. He also shared the long shifts during the runs, and without him many of the hardware problems might have plagued us much longer. I also want to thank him for some culinary tricks.

Jim Bistirlich also deserves a special thanks. Jim was someone off whom I could always bounce problems, and when I listened to his response I always saved a lot of time. I also enjoyed many pleasant lunch time conversations with Jim.

There are also the other members of the Crowe group that were always willing to listen and provide suggestions and insight on solutions to problems. Here I want to thank Roy Bossingham, Dean Chacon and Sven Ljungfelt. Roy was especially helpful in providing unsolicited software tips that saved a lot of time.

I want to thank my parents, Peter and Sheron Meyer without whose many years of efforts this would not have been possible. In this same regard I also want to thank Marian MacLean.

Finally, I gratefully thank the taxpayers of the United States of America without whose gracious support none of this would have been possible. This work was supported by the Director, Office of Energy Research, Division of Nuclear Physics of the Office of High Energy and Nuclear Physics of the U.S. Department of Energy under contracts DE–AS03–81ER40004 and DE–AC03–76SF00098.

Chapter 1

Introduction

The interest in studying the process $\pi p \rightarrow \pi p \gamma$ arises from several sources. One can presumably probe the strong πp interaction with the much better understood electromagnetic interaction. From this one can obtain information about magnet dipole moments of intermediate resonances. It is also possible to examine off shell effects in the πp interaction by looking at processes where the photon has been emitted by an external particle. In this experiment our primary motivation is to measure the magnetic dipole moment of the Δ^{++}. This is motivated by recent theoretical calculations from M.I.T., (see section 2.3) which indicate that measuring the the polarization asymmetry of the cross-section for $\pi^+ p \rightarrow \pi^+ p \gamma$ is a very sensitive probe of $\mu_{\Delta^{++}}$.

In trying to measure the magnetic dipole moment of the $\Delta(1232)$, μ_Δ, one wants to look at a kinematic situation where radiation from the intermediate Δ is a maximum with respect to the radiation from the external particles. This situation is particularly good in the $\pi^+ p$ system where external radiation from the pion and proton interfere destructively for photons at backward angles. Also as the Δ^{++} has a non-zero charge, it radiates via both this charge, and its magnetic dipole moment.

If one wants to look at off shell effects, then Picciotto[1] points out that the $\pi^- p$ system is the better candidate. In the $\pi^- p$ system the intermediate Δ^0 has zero charge and according to SU(6), zero magnetic moment. This gives a minimum contribution to the radiation from the internal particle. There is also the advantage that there is constructive interference between the external pion and proton radiation in the geometry used in the $\pi^+ p$ experiments.

---

[1] Charles Picciotto, **Phys. Rev. C31**, 1036 (1985).

Finally the radiation terms from the external lines are nearly gauge invariant, simplifying the problem of making the entire expression gauge invariant.

1.1 Magnetic Moments of Baryons

The usual techniques for measuring magnetic dipole moments of particles involve either putting the particle in a strong magnetic field and observing how fast its spin precesses, or forming an exotic atom with the particle and looking at an M1 atomic transition in the resulting system. These techniques work very well for members of the baryon octet where the most recent measurements for these particles are shown in table 1.1[2]. In this table, comparisons are made to SU(6)[3], Quark model[4] and Bag model corrections to the quark model[5]. Unfortunately neither of these approaches works for a strongly unstable particle.

Particle	Type of Measurement	μ $\frac{e\hbar}{2m_pc}$	SU(6) μ	Quark μ	Bag μ
p	Spin Prec.	2.7928	input	input	input
n	Spin Prec.	-1.9130	-1.87	-1.87	-1.87
Λ	Spin prec.	-0.613 ± 0.004	-0.93	-0.60	-0.61
Σ^-	Exotic Atom	-1.14 ± 0.05	-0.88	-1.05	-0.54 to -0.64
Σ^0	—	—	0.93	0.82	0.82
Σ^+	Spin prec.	2.379 ± 0.020	2.79	2.67	2.18 to 2.28
Ξ^-	Spin prec.	-0.69 ± 0.04	-0.88	-0.46	-0.60 to -0.63
Ξ^0	Spin prec.	-1.25 ± 0.014	-0.93	-1.39	-1.31 to -1.33

Table 1.1: Measured and predicted magnetic moments of the baryon octet.

One would need a 10^{17} gauss field in order to obtain any measurable precession , and the Δ lifetime is so short when compared to typical atomic lifetimes that even if one could form an exotic atom, the Δ would have long since decayed before any atomic transitions could take place. If one is interested in measuring μ_Δ, then different techniques need to be used.

---

[2] Values are taken from the 1986 edition of the **Particle Data Handbook**.

[3] M.A.B. Bĕg, B.W. Lee A. Pais, **Phys. Rev. Lett. 13**, 514 (1964).

[4] A. De Rújula, Howard Georgi and S.L. Glashow, **Phys. Rev. D12**, 147 (1975).

[5] G.E. Brown, Mannque Rho and Vincent Vento, **Phys. Lett 97B**, 423 (1980).

One such approach is to look at radiation emitted from the particle. Since this measures the coupling of photons to the particles, and photons can couple through the particle's magnetic dipole moment one can obtain information about the magnetic moments.

$$e(\gamma_\mu + \mu\sigma_{\mu\nu}k^\nu + \cdots)$$

As for predictions of the values of the magnetic moments of strongly unstable particles, the situation is in much better shape. Any model that predicts a magnetic moment of the baryon octet can also be used to predict values for the baryon decuplet. SU(6)[6,7] and quark model[8] calculations both predict that $\mu_{\Delta^{++}} = 2\mu_p$. Recent bag model calculations[9] predict that the dipole moment should be smaller than that of the quark model by 17 to 21%.

1.2 Previous Experiments

The largest amount of data on πp bremsstrahlung was obtained from the UCLA[10,11,12] experiment. This experiment was performed at the Berkeley 184–inch cyclotron and looked at $\pi p \rightarrow \pi p \gamma$ on a liquid hydrogen target. They looked at both π^+p and π^-p data at incident pion energies of 269Mev, 298MeV and 324MeV for eighteen different photon angles. The UCLA experiment did a very broad examination of the energy and angular dependence of the cross–sections, but in many cases their statistics were rather low; this being due to the intensities of pion beams available at the Berkeley 184–inch cyclotron. There is also some data on the π^-p system from the OMICRON experiment[13].

---

[6] Sidney Coleman and Sheldon Lee Glashow, **Phys. Rev. Lett 6**, 423 (1961).

[7] M.A. Bĕg,B.W. Lee and A. Pais, **Phys. Rev. Lett. 13**, 514 (1964).

[8] J.J.J. Kokkedee, **The Quark Model**, W.A. Benjamin Inc., New York (1969).

[9] G.E. Brown, Mannque Rho and Vincent Vento, **Phys. Lett 97B**, 423 (1980).

[10] D.I. Sober *et.al.*, **Phys. Rev. D11**, 1017 (1975).

[11] K.C. Leung *et.al.*, **Phys. Rev. D14**, 698 (1976).

[12] B.M.K. Nefkens *et.al.*, **Phys. Rev. D18**, 3911 (1978).

[13] S. Playfer, **π^-p Bremsstrahlung at the $\Delta(1232)$ Resonance**, Ph.D. Thesis from the University of Birmingham, (1981).

1.3 The Present Experiment

Our measurement has been divided into two parts. First we performed a measurement on a liquid hydrogen target of the unpolarized cross-section. This measurement is close, but not exactly in the same kinematic configuration as the UCLA experiment. Whereas their final state pions were detected near 50° in the lab with a large vertical aperture, our experiment detected pions between 55° and 95° in the lab, with a much smaller vertical aperture. This part was done first to assure us that we could indeed recognize our signal, and extract it from the backgrounds. We also wanted to understand the backgrounds in the experiment and remove or reduce as many of them as possible before performing the second half of the experiment. The second half of our measurement used a spin polarized proton target with which we measured the asymmetry of the cross-section. This measurement was made in essentially the same kinematic configuration as our unpolarized measurements.

In this thesis I will discuss both aspects of the experiment, but only the unpolarized data is presented here. The polarized data is being analyzed by Andreas Bosshard of Zürich, the other graduate student on this experiment.

Chapter 2

The Theory of Pion Proton Bremsstrahlung

At present there are essentially two approaches for calculating the process $\pi p \rightarrow \pi p\gamma$. The most simple minded of these models are the result of applying the low energy photon theorem to the elastic process $\pi p \rightarrow \pi p$. This type of calculation is referred to as the *Soft Photon Approximation* or *SPA*. A more fundamental approach to the problem is to consider the scattering process to be mediated by an isobar (Δ). In this sort of approach one tries to calculate $\pi p \rightarrow \pi p$ in terms of an isobar model in order to fix various free parameters. Then one tries to calculate the bremsstrahlung process $\pi p \rightarrow \pi p\gamma$ in terms of the fixed parameters.

It is possible to include terms for the possible radiation from an intermediate isobar in both these models, although it seems much more physically intuitive to do so in terms of an isobar model, and rather ad–hoc in the SPA calculations. This possible Δ radiation includes charge, magnetic dipole, electric quadrupole and magnetic octupole terms, (it turns out that only the charge and magnetic dipole terms make 'measurable' contributions to the spectrum). However, even if one does include terms for the charge and magnetic dipole it is still not clear exactly what all these terms mean. The dipole moment of a strongly unstable particle like the Δ is not well defined, and it is not at all clear that the moment used above and that from a prediction such as SU(6) or a bag model calculation are related. What is generally done is to define the dipole moment as if the the particle were stable; a situation which may or may not make any sense.

Finally, the coordinate system used throughout this experiment is one used by the UCLA experiment. In this coordinate system, the two 'polar' angles are α and β. Where α is the angle measured clockwise from the beamline in the horizontal plane, and β is the elevation angle from the horizontal plane. These are related to the conventional spherical polar angles θ and ϕ via the transformations:

$$\begin{aligned} \cos\theta &= \cos\alpha\cdot\cos\beta \\ \tan\phi &= \tan\beta\cdot\csc\alpha \\ \tan\alpha &= \tan\theta\cdot\cos\phi \\ \sin\beta &= \sin\theta\cdot\sin\phi \end{aligned} \tag{2.1}$$

All of these angles are given in the lab frame.

2.1 Soft Photon Theories

In Soft Photon Theories, one tries to express the bremsstrahlung cross–section for low energy photons as an expansion in powers of the photon energy, k.

$$\sigma = \frac{\sigma_0}{k} + \sigma_1 + \sigma_2\cdot k + \cdots \tag{2.2}$$

Low[14] showed that one can obtain a unique value of both σ_0 and σ_1 in terms of the cross–section where no photon is involved. In the case of $\pi p \rightarrow \pi p\gamma$, σ_0 and σ_1 are calculated in terms of the cross–section for $\pi p \rightarrow \pi p$. To obtain the expansion in powers of k, one starts by writing down the amplitude for all bremsstrahlung from external lines, (for $\pi p \rightarrow \pi p\gamma$, these are shown in figure 2.1). One then calculates what terms need to be added to the amplitude to make it gauge invariant through the desired order of k. If the amplitude calculated from the diagrams is $\mathcal{M}^1_\mu\epsilon^\mu$ and the gauge term is $\mathcal{M}^2_\mu\epsilon^\mu$, then gauge invariance requires that $(\mathcal{M}^1_\mu + \mathcal{M}^2_\mu)k^\mu = 0$. To obtain the gauge term, one expands the amplitude $\mathcal{M}^1_\mu k^\mu$ in powers of k, and then retain only those terms which are at most linear in k.

In 1972, Fischer and Minkowski[15] examined $\pi p \rightarrow \pi p\gamma$ in terms of the Soft Photon Approximation. They calculated the amplitude for the process shown in figure 2.1; $T(s,t,m_1^2,m_2^2)$

---

[14] F.E.Low **Phys. Rev. 110**, 974 (1958).

[15] W.E. Fischer and P. Minkowski, **Nucl. Phys. B36**, 519 (1972).

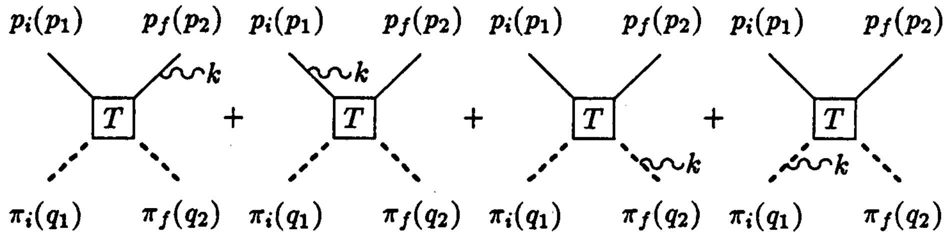

Figure 2.1: Diagrams involved in πp → πpγ.

was the πp elastic scattering amplitude, s and t were the usual Mandelstam variables and m_1 and m_2 were the masses of the incoming and outgoing pions. The counter term they added to make the amplitude gauge invariant was good through $\mathcal{O}(k^1)$, and the calculation of the amplitude,(equation 2.3) was good through $\mathcal{O}(k^0)$.

$$\begin{aligned}
\mathcal{M}_\mu &= \overline{u}(p_2)\left\{e(\gamma_\mu - \frac{i}{2M}\lambda\sigma_{\mu\nu}k^\nu)\frac{\not{p}_2 + \not{k} + M}{2p_2\cdot k}T\right. \\
&- T\frac{\not{p}_1 - \not{k} + M}{2p_1\cdot k}e(\gamma_\mu - \frac{i}{2M}\lambda\sigma_{\mu\nu}k^\nu) + e\left(\frac{q_{2\mu}}{q_2\cdot k} - \frac{q_{1\mu}}{q_1\cdot k}\right)T \\
&+ e\left[(k\cdot p_1 - k\cdot q_1)\left(\frac{q_{1\mu}}{q_1\cdot k} - \frac{p_{1\mu}}{p_1\cdot k}\right)\right. \\
&+ \left.(k\cdot p_2 - k\cdot q_2)\left(\frac{q_{2\mu}}{q_2\cdot k} - \frac{p_{2\mu}}{p_2\cdot k}\right)\right]\frac{\partial T}{\partial\nu} \\
&+ e\left[(k\cdot p_2 - k\cdot q_2)\left(\frac{q_{2\mu}}{q_2\cdot k} - \frac{p_{2\mu}}{p_2\cdot k}\right)\right. \\
&+ \left.\left.(k\cdot p_2 - k\cdot p_1)\left(\frac{p_{1\mu}}{p_1\cdot k} - \frac{p_{2\mu}}{p_2\cdot k}\right)\right]\frac{\partial T}{\partial\Delta}\right\}u(p_1) \qquad (2.3)
\end{aligned}$$

Where M was the proton mass, m was the pion mass and ν and Δ were given by:

$$\begin{aligned}
\nu &= p_1\cdot q_1 + p_2\cdot q_2 \\
\Delta &= p_1\cdot q_2 + p_2\cdot q_1 \qquad (2.4)
\end{aligned}$$

and λ is the anomalous magnetic moment of the proton.

The five-fold differential cross-section is then given in equation 2.5. This cross-section is plotted versus photon energy in figure 2.2 . It is seen that the theory breaks down at about 50MeV, as the theoretical cross-section begins to deviate from the expected $\frac{1}{k}$ falloff for bremsstrahlung.

$$\frac{d^5\sigma}{d\Omega_\pi d\Omega_\gamma dE_\gamma} = \frac{1}{(4\pi)^5}\int \frac{p_2^2 dp_2}{E_{p_2}}\frac{q_2^2 dq_2}{E_{q_2}}\frac{d\Omega_p}{\sqrt{(p_1\cdot q_1)^2 - M^2m^2}}\delta^4(\sum P_i)\sum_{spins} \mid \mathcal{M}_\mu\epsilon^\mu \mid^2 \quad (2.5)$$

Fischer and Minkowski also tried to extend the model to higher energy photons by calculating additional terms in equation 2.2 . In addition to the higher order terms in the expansion, they found that radiation terms from internal processes were important, being of the same order as the k^1 term. To calculate what sort of deviations from the *SPA* internal radiation terms would give, they included terms for charge, magnetic dipole, electric quadrupole and magnetic octupole radiation from an internal Δ. Finally, they concluded that it would be necessary to measure the spin polarization of either the incoming or outgoing proton in order to measure the dipole moment of the Δ.

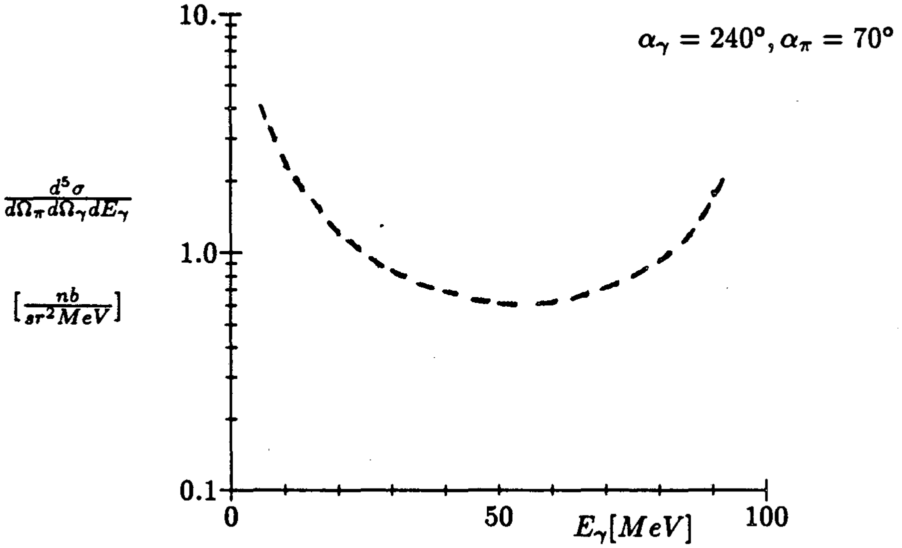

Figure 2.2: Bremsstrahlung spectrum as predicted by *SPA*.

After the UCLA experiment had been performed Nefkens and Sober[16] developed the External-Emission Dominance model, (*EED*). This model had no theoretical footing; it just gave a very good fit to the existing data. In *EED*, only the first terms in the *SPA* model are retained. At the time that *EED* was proposed, it gave the best available fit to the existing data, but no understanding as to why that fit should be so good. There is also no way of extracting a magnetic dipole moment of the Δ from *EED*.

---

[16] B.M. Nefkens and D.I. Sober, **Phys. Rev. D9**, 2434 (1976).

Finally, the most recent calculation of the *SPA* type was performed by Liou and Nutt[17]. In this calculation, Liou and Nutt pointed out that the previous *SPA* calculations had been performed incorrectly. In the expansion in equation 2.2 all expansion parameters are by definition independent of k. However, in all the previous calculations these parameters were not independent of k.

$$\begin{aligned}\sigma_0 &= \lim_{k\to 0}(k\sigma)\\ \sigma_1 &= \lim_{k\to 0}\frac{\partial}{\partial k}(k\sigma)\end{aligned}$$

They indicated that instead of using equation 2.2, previous authors had used:

$$\sigma = \frac{\sigma_0(k)}{k} + \sigma_1(k) + \cdots$$

When the calculation was done correctly, *SPA* made what they concluded was the best fit to the UCLA data. Other *SPA* calculations have been performed by Haddock and Leung[18], but these will not be discussed here.

2.2 Isobar Calculations

In an isobar calculation, one begins with an interaction Lagrangian which describes πp scattering in terms of one or more intermediate states. To this Lagrangian, one adds couplings to photons, and then tries to calculate bremsstrahlung in the model. The first isobar calculation of $\pi p \to \pi p\gamma$ was performed by Kondratyuk and Ponomarev in 1967[19]. They noted that if one chose a kinematic situation in which the π and p came out of the reaction in the forward direction, then bremsstrahlung from the π and p would destructively interfere for photons in a backward direction. By looking for photons in a backward direction, any effects due to the intermediate states should be a maximum with respect to the external radiation.

In the Kondratyuk–Ponomarev calculation,(*KP*) they assumed that the only intermediate state was the P_{33} wave, the $\Delta(1232)$, giving the elastic cross-section as:

$$\frac{d\sigma}{d\Omega} = \frac{\sin^2\delta_{33}}{|\,q\,|^2}(3\cos^2\theta + 1).$$

---

[17] M.K. Liou and W.T. Nutt, **Phys. Rev. D16**, 2176 (1977).

[18] R.P. Haddock and K.C. Leung, **Phys. Rev. D9**, 2151 (1974).

[19] L.A. Kondratyuk and L.A. Ponomarev, **Yad. Fiz.** 7, 111 (1967) and **Sov. J. Nucl. Phys.** 7, 82 (1968).

They used an interaction Lagrangian given in equation 2.6 . This Lagrangian included radiation coupling only to the charge and magnetic dipole moment of the intermediate Δ. All higher order terms were assumed to have a very small contribution to the amplitude, and were ignored. There were no off shell effects included in this calculation.

$$\begin{aligned}\mathcal{L}_{int} &= \left\{\frac{\lambda}{im_\pi}\overline{\psi}_p(x)\psi^\mu_\Delta(x)\left[\partial_\mu + ieA_\mu(x)\right]\phi_\pi(x) + h.c.\right\} \\ &+ \; e\psi^\rho_\Delta(x)\left[Q_\Delta\Gamma^\mu_{\rho\sigma}A_\mu(x) + \frac{2}{3}\frac{\mu_\Delta}{2m_p}iS^{\mu\nu}_{\rho\sigma}F^{\mu\nu}(x)\right]\psi^\sigma(x) \qquad (2.6)\end{aligned}$$

In equation 2.6, ψ^α was the Rarita-Schwinger wave function for a spin $\frac{3}{2}$ particle and Γ and S were given by:

$$\begin{aligned}\Gamma^\mu_{\rho\sigma} &= -\gamma^\mu(\delta_{\rho\sigma} - \frac{1}{3}\gamma_\rho\gamma_\sigma) + \frac{1}{3}(\gamma_\rho\delta^\mu_\sigma - \gamma_\sigma\delta^\mu_\rho) \\ S^{\mu\nu}_{\rho\sigma} &= -\frac{1}{2}\sigma^{\mu\nu}\delta_{\rho\sigma} - (\delta^\mu_\rho\delta^\nu_\sigma - \delta^\mu_\sigma\delta^\nu_\rho)\end{aligned}$$

The propagator for the spin $\frac{3}{2}$ particle in the nonrelativistic limit was expressed as

$$G_{ik} = \begin{pmatrix} d_{ik} & 0 \\ 0 & 0 \end{pmatrix}\frac{1}{P_0 - M + \frac{i\Gamma(s)}{2}}$$

where

$$d_{ik} = \delta_{ik} - \frac{1}{3}\sigma_i\sigma_k$$

The terms λ and $\Gamma(s)$ were adjusted to fit the P_{33} scattering amplitude. With the interaction Lagrangian, and the spin $\frac{3}{2}$ propagator, the bremsstrahlung cross-section was calculated. They predicted a large bump in the bremsstrahlung spectrum which was highly dependent upon the magnetic dipole moment of the Δ^{++}, (see figure 2.3). It was because of this bump that the UCLA experiment was performed, and the most striking result of that experiment was that this predicted bump was not present.

In a later paper[20], Kondratyuk and Ponomarev generalized their discussion to intermediate states of higher spin. For more discussion one should consult the cited reference. Additional calculations performed by Baier *et.al.*[21] and by Beder[22] continued to show the

---

[20] V.I. Zakharov, L.A. Kondratyuk and L.A. Ponomarev, Yad. Fiz. 8, 783 (1968) and Sov. J. Nucl. Phys., 456 (1969).

[21] R. Baier, L. Pittner and P. Urban Nucl. Phys. B27, 589 (1971).

[22] D.S. Beder, Nucl. Phys. B84, 362 (1975).

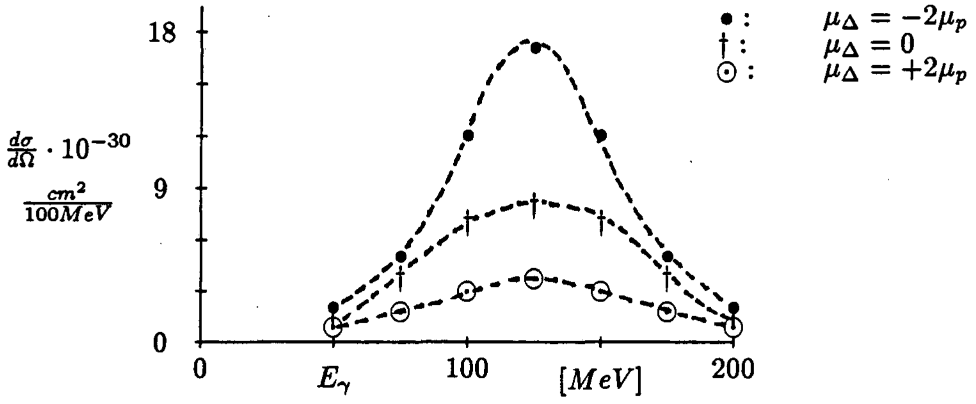

Figure 2.3: KP prediction for $\pi p \rightarrow \pi p\gamma$.

bump in the bremsstrahlung spectrum. The lack of such a bump in the UCLA experiment remained a mystery for several years.

Finally, in 1978 Pascual and Tarrach[23] were able to extract a magnetic dipole moment for the Δ^{++} from the UCLA data. They noted that the previous works had used a propagator for the spin $\frac{3}{2}\Delta$ which ignored the finite width of the Δ. Effects due to the finite width were then included in their propagator. They also avoided the ambiguities in the previous calculations that result from the imposition of gauge invariance by calculating only the contribution from the photon that leads to a final state Δ at the center of the Δ resonance. This eliminated the non–negligible ambiguities that arose from making the amplitudes gauge invariant. There was one obvious problem with their calculation, that being it did not include external radiation from the final state pion and proton. From their calculation, one could express the cross-section as

$$\frac{d^5\sigma}{d\Omega_\pi d\Omega_\gamma dE_\gamma} = a + b\mu_{\Delta^{++}} + c\mu^2_{\Delta^{++}}$$

where the a, b and c coefficients could be easily calculated. They then extracted a value for $\mu_{\Delta^{++}}$ from the UCLA data. They found that data was best fit if $\mu_{\Delta^{++}} = (2.4 \pm 0.9)\mu_p$. In their calculation, it was found that this value of the Δ^{++} magnetic dipole moment was the only value that gave no bump in the bremsstrahlung spectrum. Later, Nefkens of the UCLA experiment went back and fit their data with the Pascual and Tarrach model[24]. In this fit he monte–carlo'd the acceptance of their system and folded in the Pascual and

---

[23] P. Pascual and R. Tarrach **Nucl. Phys. B134**, 133 (1978).

[24] B.M.K. Nefkens, *et.al.*, **Phys. Rev. D18**, 3911 (1978).

Tarrach model. From this he obtained that $1.7\mu_p < \mu_\Delta < 2.4\mu_p$, the value of $\mu_{\Delta^{++}}$ which has been listed in the **Particle Data Book**. All calculations after that of Pascual and Tarrach using an isobar model have been performed at MIT and are discussed in the next section.

2.3 The MIT Calculations

The most recent calculation was performed at MIT by Heller, Kumano, Martinez and Moniz[25,26,27,28]. The most striking prediction of this model was that a spin asymmetry measurement of $\frac{d^5\sigma}{d\Omega_\pi d\Omega_\gamma dE_\gamma}$ would be very sensitive to the magnetic dipole moment of the Δ^{++}. This was supported by calculations which showed what the effects would be. This prediction was one of the principal motivations for performing the present experiment.

The MIT group begins their calculation by looking at the scattering amplitude for $\pi p \rightarrow \pi p$. Initially they only consider one partial wave in the scattering amplitude, the P_{33} wave and use phase shifts to fix various free parameters in their theory. To do this, they equate the two diagrams in figure 2.4; the propagator for the intermediate Δ is given in equation 2.7.

$$G_\Delta = (E - m_\Delta - \Sigma_\Delta)^{-1} \tag{2.7}$$

The self energy correction to this propagator Σ_Δ is given in equation 2.8, and shown in figure 2.5.

$$\Sigma_\Delta = \left(\frac{f_{\pi N\Delta}}{m_\pi}\right)^2 \int \frac{d\mathbf{q}}{(2\pi)^3} \frac{\mathbf{S}^\dagger\cdot\mathbf{q}\,\mathbf{S}\cdot\mathbf{q}\,h^2(q^2)}{(E' - \frac{q^2}{2m})^2 - \omega_q^2}(T^+)^\dagger T^+ \tag{2.8}$$

In equation 2.8 $E' = E - m_p$, which for a proton at rest is just the total pion energy. The operators T and S are isospin and spin transition operators respectively, and $\omega_q^2 = q^2 + m_\pi^2$. The $\pi N\Delta$ vertex term is given by formula 2.9, and the $\pi N\Delta$ coupling is parameterized by equation 2.10.

$$\frac{i f_{\pi N\Delta}}{m_\pi} h(q^2)\mathbf{S}^+\cdot\mathbf{q}\,\mathbf{T}_\alpha^+ \tag{2.9}$$

$$\frac{f_{\pi N\Delta}}{m_\pi} h(q^2) = \frac{g}{\alpha^2 + q^2} \tag{2.10}$$

---

[25] Jose C. Martinez **πN Bremsstrahlung in the Isobar Model**, MIT Ph.D Thesis (1981).

[26] E.J. Moniz **Nucl. Phys. A374**, 557c (1982).

[27] Shunzo Kumano, **Nucleon Substructure and Nuclear Properties**, MIT Ph.D. Thesis, (1985).

[28] L. Heller, S. Kumano, J.C. Martinez and E.J. Moniz, **Phys. Rev. C35**, 718 (1987).

In this calculation, m_Δ, g and α are free parameters which are fit to the 33–phase shifts. The value of m_Δ used here is a bare mass, and not the measured mass of $1232 MeV$. The self energy of the Δ generated by internal coupling to the πN channel shifts the mass to the measured mass, and generates the width of the Δ.

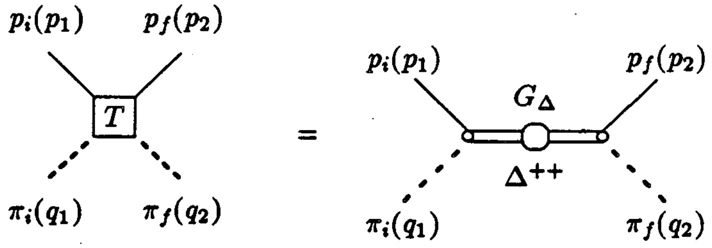

Figure 2.4: Elastic Diagram of the MIT theory.

Figure 2.5: Self energy corrections to Δ propagator.

When they perform their fit to the P_{33} phase shifts, they get two sets of parameters which can describe the elastic cross-section. These are presented in table 2.1. Both of these sets of coefficients give good fits over the region of interest, but the first set is slightly better. In all of the later calculations, they use this set of parameters.

	g	α $[fm^{-1}]$	m_Δ $[MeV]$
1	$2.12/m_\pi^{-\frac{3}{2}}$	1.2	1445
2	$1.79/m_\pi^{-\frac{3}{2}}$	2.2	1322

Table 2.1: Parameters fit by the P_{33} phase shifts in the MIT theory.

With these coefficients, they then calculated the process $\pi p \rightarrow \pi p \gamma$. Figure 2.6 shows the diagrams involved in $\pi p \rightarrow \pi p \gamma$ from the P_{33} partial wave. The '$\pi N \Delta \gamma$ vertex' shown in those diagrams is not a true vertex, it is just shorthand for the diagram shown in figure

2.7, and is a gauge fixing term. They do not include terms due to couplings to the $\pi\pi$N channel in the intermediate state, but argue that its effects are small.

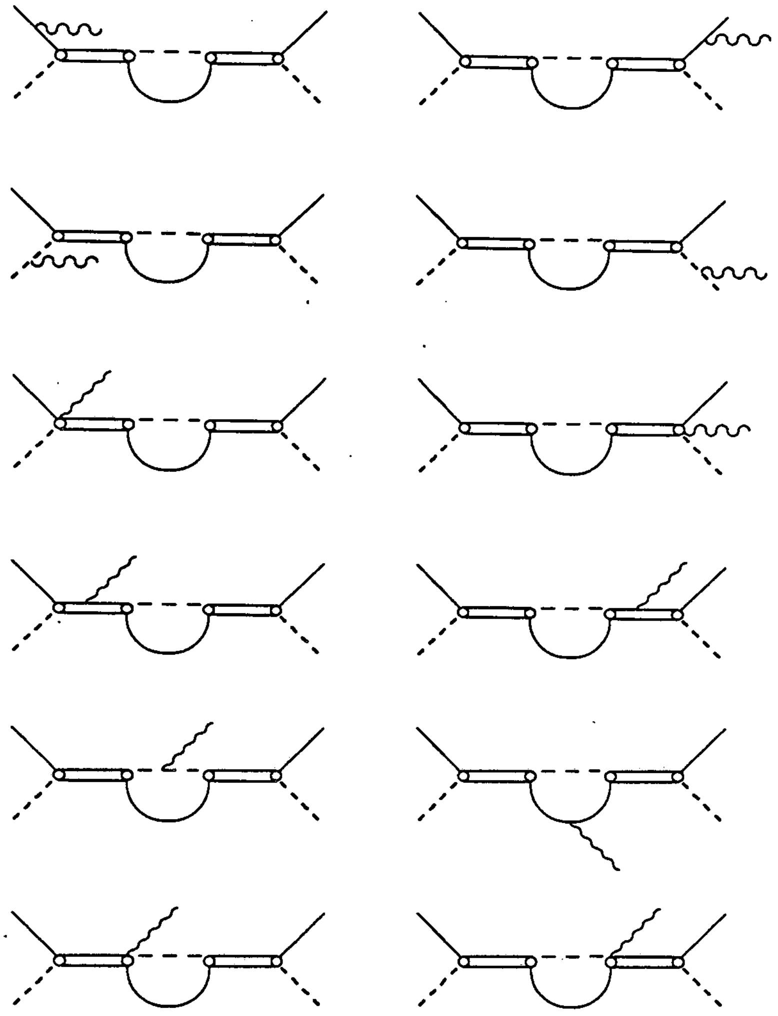

Figure 2.6: Diagrams involved in πp → πpγ through the P_{33} partial wave.

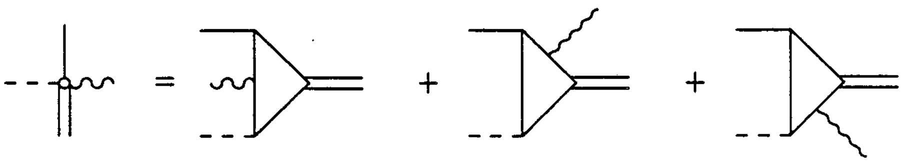

Figure 2.7: Four–point vertices.

As the calculation stands now, it is possible to calculate the cross–sections with good accuracy, the P_{33} wave being responsible for over 90% of the elastic cross–sections at these energies. However, to be able to calculate a spin asymmetry it is necessary to include effects for other partial waves. The asymmetry in the elastic cross–section arises from interference between the different partial waves. As such, to have a calculation for the asymmetry in $\pi p \rightarrow \pi p \gamma$ agree with the elastics at low photon energy, it is imperative to include more partial waves. To this regard, the MIT group also include effects from the S_{31} and P_{31} partial waves. The vertex terms for these resonances coupling to the $N\pi$ channel are parameterized exactly as in equation 2.10.

$$\frac{f_{\pi N \Delta_s}}{m_\pi} h(q^2) = \frac{g_s}{\alpha_s^2 + q^2}$$

$$\frac{f_{\pi N \Delta_p}}{m_\pi} h(q^2) = \frac{g_p}{\alpha_p^2 + q^2}$$

The spin $\frac{1}{2}$ propagators for these two waves are the normal propagators with self–energy corrections included. With this there are then two free parameters for each of these partial waves which are fit to the experimental phase shifts. The results of these fits are presented in table 2.2.

S_{31}	$\alpha_s = 5.75 fm^{-1}$	$g_s = 0.36/m_\pi$
P_{31}	$\alpha_p = 2.09 fm^{-1}$	$g_p = 2.74/m_\pi^2$

Table 2.2: The fit parameters for the S_{31} and P_{31} partial waves.

When this calculation is done, the best fit to the UCLA data is found if μ_Δ^{++} is between $2.5\mu_p$ and $3.5\mu_p$. All $\pi^- p$ data are consistent with a value of $\mu_\Delta^0 = 0\mu_p$. In figure 2.8 is shown the MIT theory fit to the UCLA data for one of their photon counters. In figure 2.9, the prediction for the present experimental geometry are presented.

As well as fitting cross–sections, this theory also predicts that a spin asymmetry measurement would be a very sensitive probe of μ_Δ^{++}. It is also found that this asymmetry is not particularly sensitive to the choice of the parameter α in the P_{33} partial wave, see table 2.1. Figure 2.10[29] shows the prediction of the asymmetry for the UCLA experiment in one of their geometries. In this figure, there are four curves displayed. The upper two curves are for $\mu_\Delta = 2.5$ and the two values of α, while the lower two curves are for $\mu_\Delta = 1.8$, again

---

[29] The data in this figure is taken from the Ph.D. thesis of Jose Martinez.

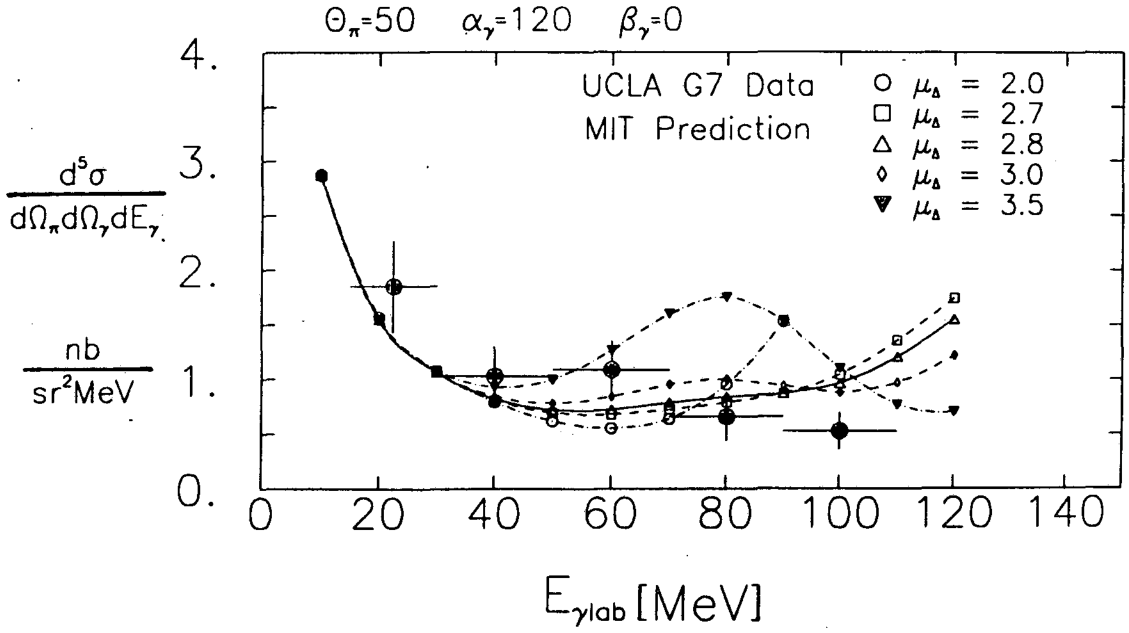

Figure 2.8: MIT Theory fit to the UCLA data.

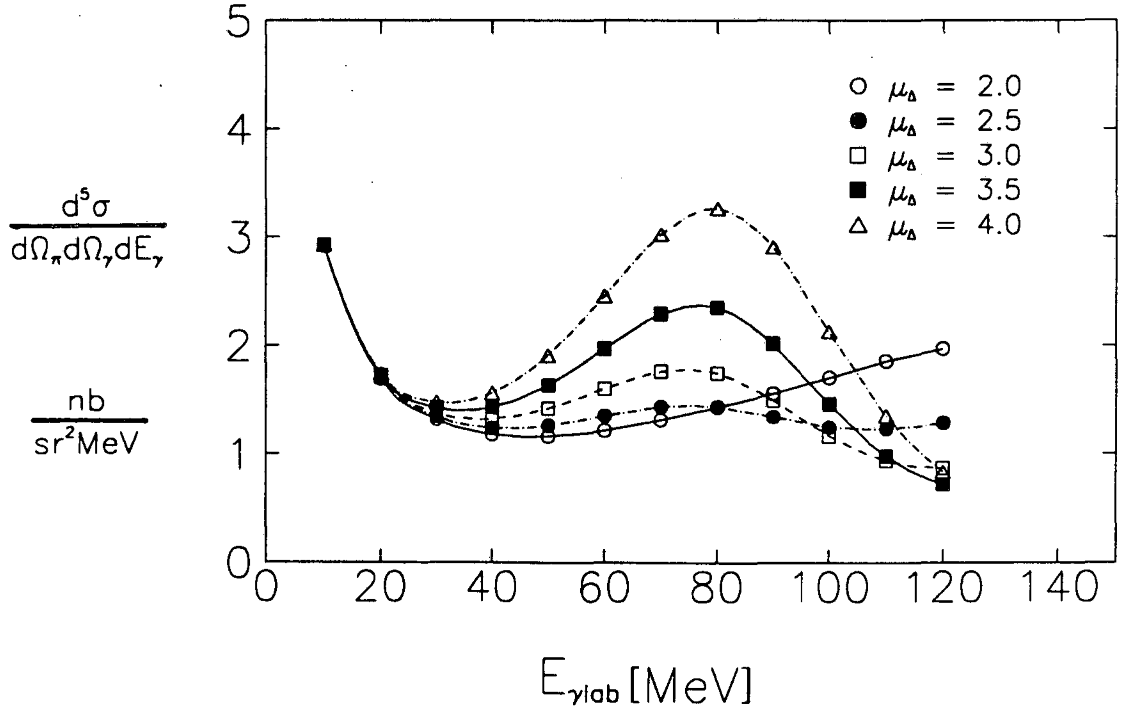

Figure 2.9: MIT Theory predictions for this experiment.

with the two accepted values of α. In figure 2.11 are shown the asymmetry predictions of the MIT theory for our experimental geometry, all of these curves are for the first value of α.

Finally there is the question of higher order multipole radiation from the Δ^{++}. As was stated earlier in this chapter, the Δ can couple to radiation through its quadrupole and octupole moment. The MIT theory has the quadrupole moment of the Δ as a parameter. In figure 2.12[30] are plotted the asymmetries with the maximum and minimum allowed values of the quadrupole moment. The variation seen in these plots is too small to be measured with the sort of an asymmetry experiment we have performed. Essentially the quadrupole is too small to have any observable effects on the calculation.

There are several uncertainties in this model which limit the precision with which one can measure the dipole moment of the Δ. For the unpolarized cross–section, theoretical ambiguities limit the precision to $\pm 0.25\mu_p$. These ambiguities arise from the uncertainty in the choice of α as well as the treatment of off–shell effects in the πN transition matrix. This arises from the reduction of the theory from a fully relativistic treatment to a Schrödinger type equation. The theory is also only valid for photon energies less than the width of the Δ resonance, 116MeV. With the polarization asymmetry measurement, the theoretical uncertainties are not as limiting as in the cross–section measurements. In this case one is limited by a theoretical error of $\pm 0.10\mu_p$.

It is because of this theory that our measurement was performed. It is believed that the theoretical understanding of pion proton bremsstrahlung is at a point that one can reasonably interpret any new data. Because of this, all comparisons to theory are made with this theory, and it is the one we use to extract the dipole moment of the Δ^{++}. It is clear that this method of measuring the dipole moment of an unstable particle is very theory dependent, and that a new theory could come along from which a completely different value of μ_Δ will be extracted from our data, (as in the case of the UCLA data between the Pascual and Tarrach value and the MIT value). However, regardless of this the actual cross–section and asymmetry remains the same and will hopefully provide theorist with enough information to develop better models of these processes.

---

[30] This data in this figure is taken from the Ph.D. thesis of Shunzo Kumano.

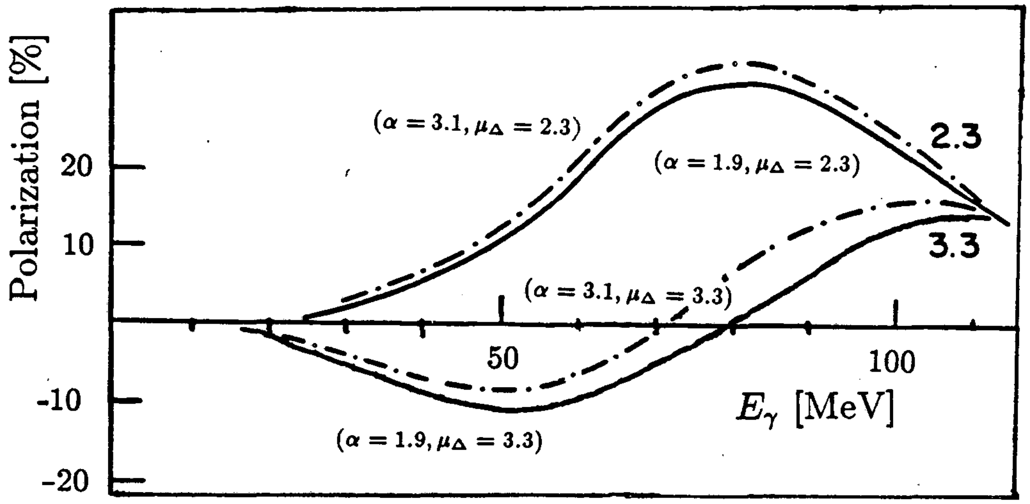

Figure 2.10: MIT Theory polarization asymmetry predictions for the UCLA experiment comparing the two values of α.

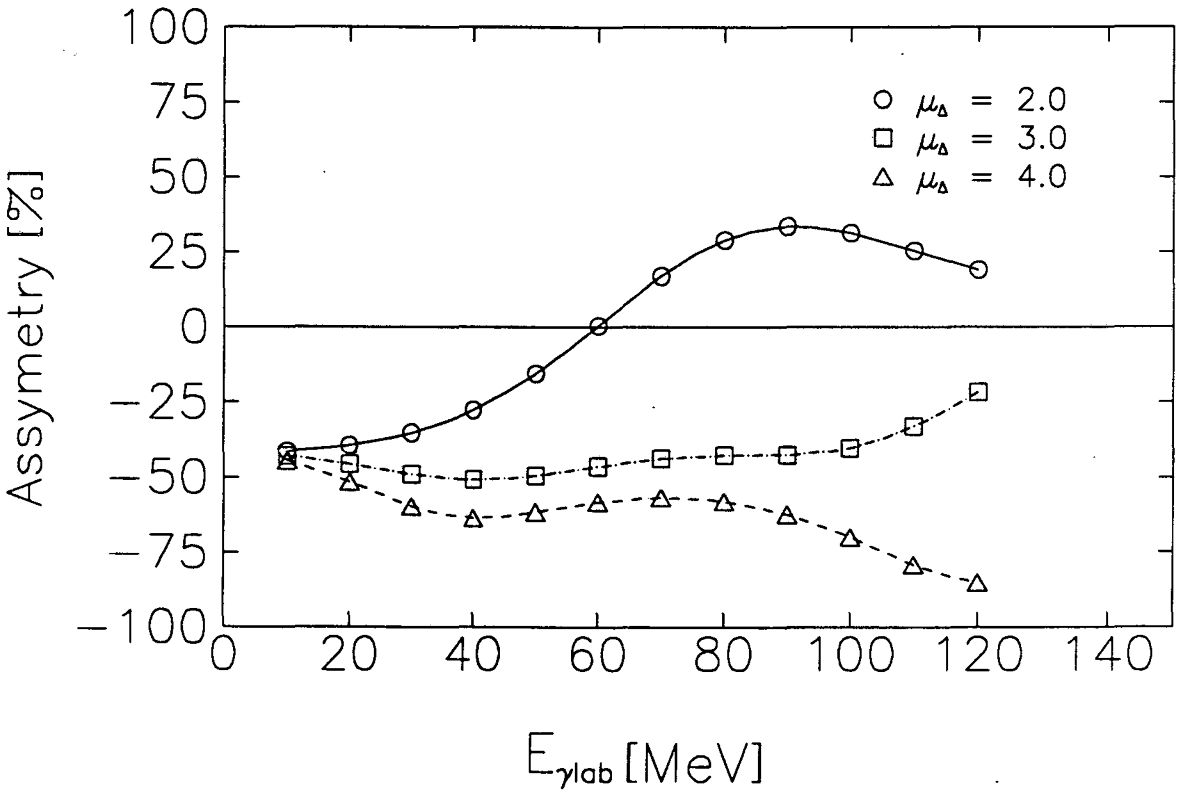

Figure 2.11: MIT Theory polarization asymmetry predictions for this experiment.

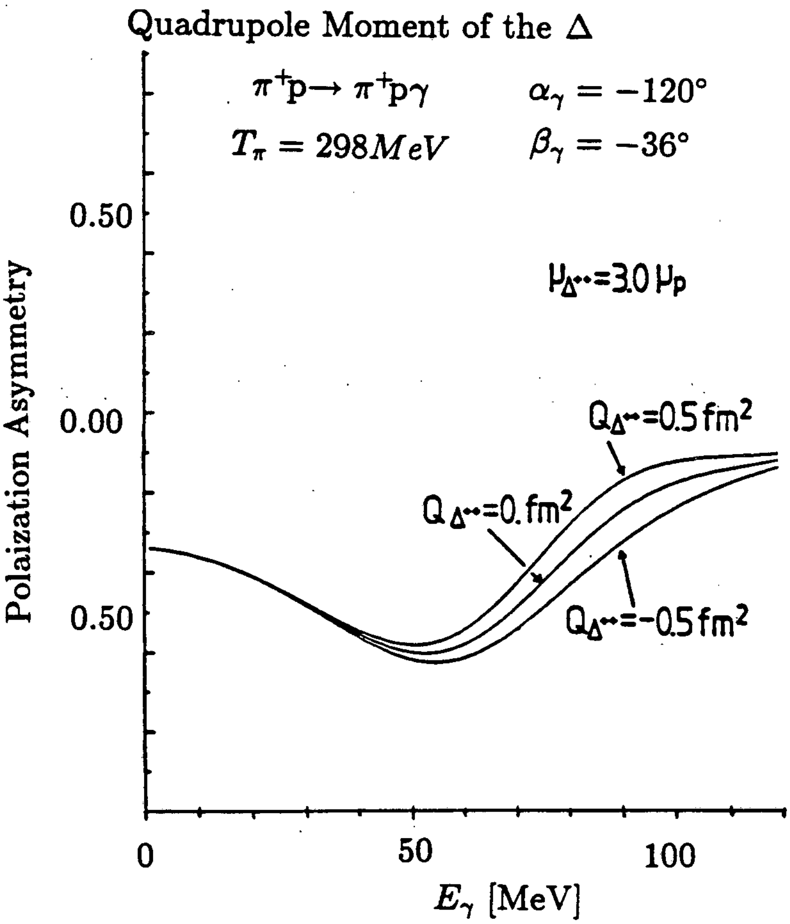

Figure 2.12: Effects of the Δ quadrupole moment on the asymmetry.

Chapter 3

The Apparatus

In order to accurately measure the bremsstrahlung spectrum, one wants to measure the momentum and energy of the three particles in the final state of $\pi p \rightarrow \pi p \gamma$. By using three existing particle detectors at SIN (Schweizerisches Institut für Nuklearforschung) it has been possible to put together a detector which is capable of making these measurements. The pion spectrometer is a large picture–frame magnet with multiwire proportional chambers, (MWPC) mounted on both the front and back sides. The desired pions travel through the magnet, and the MWPC information allows accurate track reconstruction. The proton detector consists of large blocks of plastic scintillator behind thin strips of the same scintillator. The thin strips allow one to make a $\frac{dE}{dx}$ measurement, while the large blocks will stop up to 150 MeV protons giving E. Finally the photon detector is a square array of 64 sodium iodide crystals. A diagram of the entire setup is shown in figure 3.1.

Two different targets are utilized in this experiment. In the measurement on unpolarized protons, a mylar target vessel in the shape of a cylinder with domes on each end and containing liquid hydrogen, (LH_2) is used. For the polarized measurement an SIN polarized proton target is operated. The polarized material is a 2cm in diameter by 3cm high cylinder of butanol, ($C_4H_{10}O$).

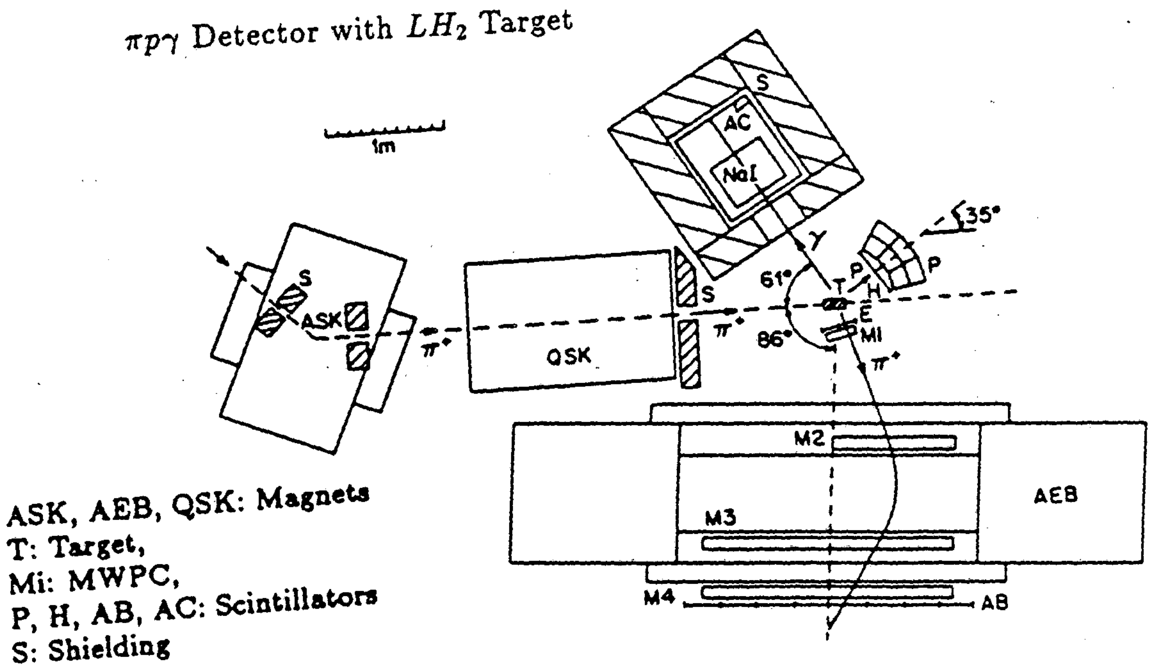

Figure 3.1: Experimental setup for the liquid hydrogen target.

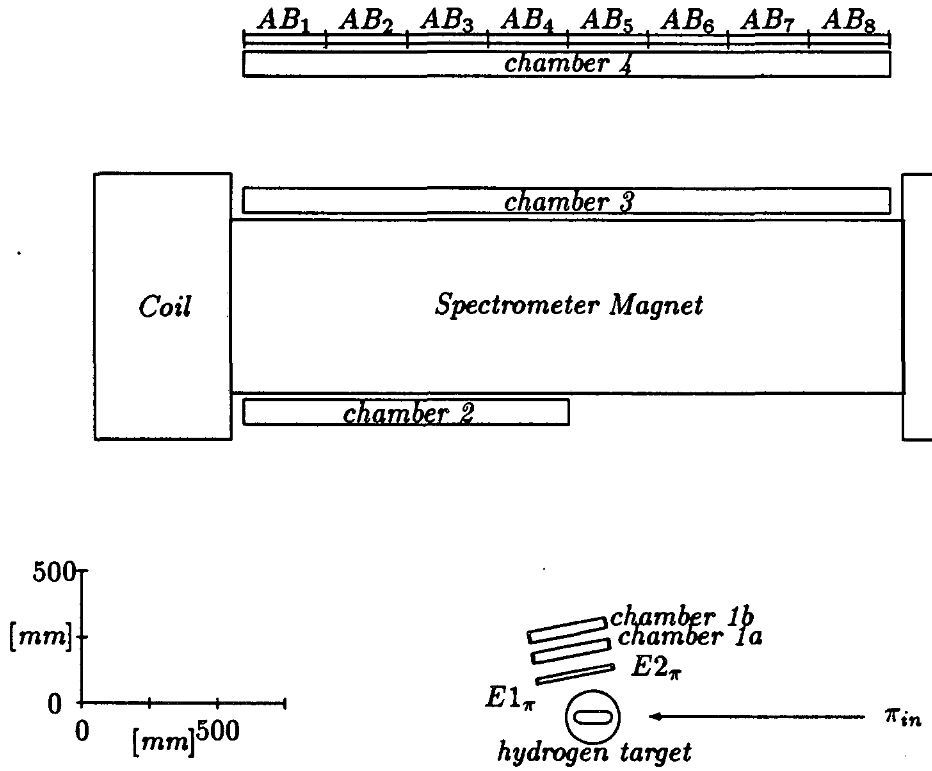

Figure 3.2: The pion spectrometer in unpolarized configuration.

3.1 The Pion Spectrometer

The pion detector is the SIN pair spectrometer[31,32] with modifications to allow the pions to travel entirely through the spectrometer; the pions of interest are not turned around as are electrons when running in pair spectrometer mode. A diagram of the pion spectrometer operated with the LH_2 target is shown in figure 3.2; when the polarized target is in place, the spectrometer configuration is changed to that shown in figure 3.3. This change is necessary because of the $25KG$ polarizing field which bends the pion tracks towards the upstream end of the spectrometer magnet.

3.1.1 Spectrometer Magnet

The central part of the pion detector is a large, ($2500mm \times 650mm \times 520mm$ usable volume) picture frame magnet. The maximum central field strength is $11.2KG$ while the operating

---

[31] J.C. Alder *et.al.*, NIM **160** ,93 (1979).

[32] SIN User's Handbook, 87 (1981).

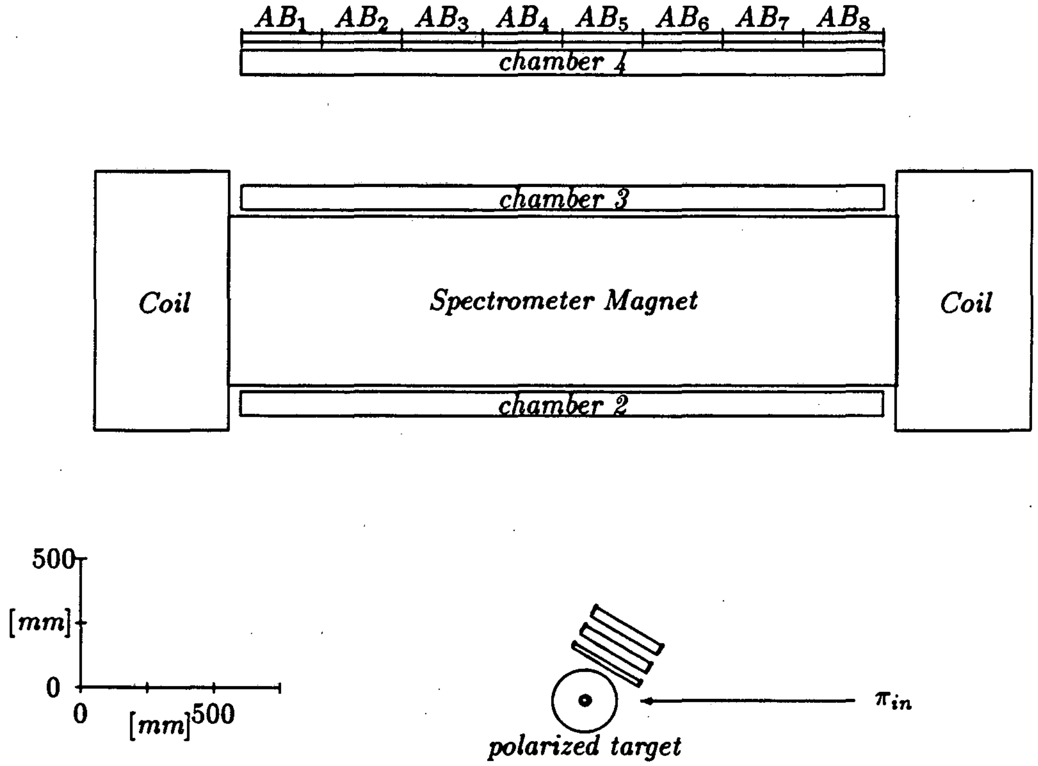

Figure 3.3: The pion spectrometer in polarized configuration.

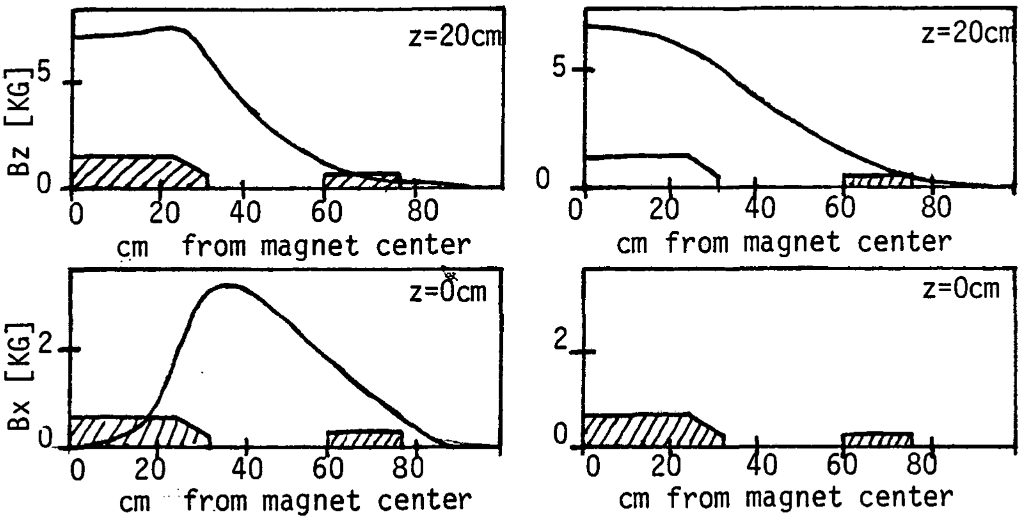

Figure 3.4: Field maps of the pion spectrometer magnet.

strength for this experiment is $+6.8KG$ in the polarized configuration and $-6.8KG$ in the unpolarized configuration, (see section 3.1.4 for an explanation for these choices). The magnetic volume has been mapped at a strength of $8KG$; the map being scaled linearly down to the field strengths used in this experiment. Figure 3.4 shows a plot of field strength vs. both elevation and distance from the magnet center, this field distribution is seen to be rather inhomogeneous. Because of the inhomogeneity, all particle tracking is performed via a monte–carlo program, (see section 4.1.1) which makes use of the measured field map.

3.1.2 The Pion Trigger Counters

There are three arrays of plastic scintillator paddles used to define the pion trigger, the E-array, the B-array and the A-array. The E-array consists of two $300mm \times 500mm \times 3mm$ pieces of scintillator sitting directly in front of the first wire chamber, and is used as a start for all TDC's in the experiment. The B and A arrays sit immediately after the last wire chamber and each contains 8 $300mm \times 500mm \times 3mm$ paddles. In order to have a pion event it is necessary for both the B and A paddle in a given column to fire, however only the TDC and ADC information from the B array is recorded. The electronic logic diagram for the pion spectrometer can be found in Appendix D.

The information obtained from these plastic counters is sufficient to cleanly discriminate between pions and protons in the pion spectrometer. The time of flight of the particle is measured between the E array and the B array which gives a sharp timing peak for the pions with a width of 3.08ns FWHM, whereas the protons come in a long tail extending from the pion time out 100 ns. There is also a clear separation in pulse height; the pions which we detect are all minimum ionizing, while the protons are on the low–energy rise in their energy loss. A combination of pulse height and time of flight is used at the lowest level of our analysis procedure to make sure that we have a pion in the spectrometer.

The efficiencies of the various arrays were measured in elastic runs in which the particular array was left out of the trigger. From these measurements we have that the efficiency of the E–array for pions was $99.88 \pm 0.12\%$ and that for the AB combination was $97.6 \pm 1.4\%$.

3.1.3 The Multiwire Proportional Chambers

There are five wire chambers in the pion spectrometer. Three in front of the magnet, and two behind it. The first two chambers are small 2-plane chambers, while the last three are large three plane chambers. Because of the presence of the additional magnetic field when using the polarized target, it is necessary to use a different chamber in the 2^{nd} position than for the unpolarized target. This modification can be seen by comparing figures 3.1 and 3.2. The front two chambers are clamped to a *camp table* which is attached to the magnet. The third chamber is bolted directly to the spectrometer magnet, and the fourth and fifth chambers are bolted to a moveable rack that rides on rails attached to the top of the magnet. The rack is located relative to the magnet with four locating pins, which allow accurate positioning of the entire assembly.

The efficiencies of the wire chambers were measured with respect to the plastic scintillator arrays. We required a pion, as identified by the pion scintillator arrays, (see previous section) to have passed through one of three specific counters in the AB array. By restricting ourselves to only three of the eight counters, we knew from monte–carlo calculations that the pion had to go through all 4 wire chambers. We then totaled the number of times that we reconstructed at least one triangle in a given chamber and from this obtained a chamber efficiency. During the unpolarized run, there was readout difficulty with the 2nd chamber, particularly under conditions of high trigger rates. Because of this we had a substantially lower efficiency in that chamber than the other two. There was also a problem with a part of the readout system for the 3'rd chamber. About 2.5% of the time, it randomly changed the state of the 16's bit in the readout data from one of the wire planes. For such a small fraction this problem was corrected in the offline software. The effect of this bug after the offline corrections was a systematic shift in the pion's momentum of about 10MeV/c for less than 0.5% of the data.The measured chamber efficiencies for the $\pi p \rightarrow \pi p \gamma$ runs is presented in table 3.1, and that for the $\pi p \rightarrow \pi p$ runs is presented in table 3.2. The large efficiency difference between $\pi p \rightarrow \pi p \gamma$ and $\pi p \rightarrow \pi p$ runs is due to the rate problem mentioned above. For $\pi p \rightarrow \pi p \gamma$ the trigger rate was about 7 per second, while for $\pi p \rightarrow \pi p$ the rate was about 95 per second[33]. The low rate elastic run was triggered at about 46 per second[34]. This rate related efficiency problem only caused a reduction in the final statistics.

MWPC	Average Eff.	Highest eff.	Lowest eff.
1	0.966	0.972	0.961
2	0.566	0.703	0.403
3	0.867	0.875	0.859
4	0.907	0.913	0.897

Table 3.1: Efficiency of the wire chambers for $\pi p \rightarrow \pi p \gamma$ runs.

MWPC	Average Eff.	Highest eff.	Lowest eff.	Low trigger rate
1	0.963	0.967	0.954	0.976
2	0.174	0.119	0.194	0.558
3	0.863	0.874	0.842	0.870
4	0.904	0.915	0.877	0.909

Table 3.2: Efficiency of the wire chambers for $\pi p \rightarrow \pi p$ runs.

---

[33] This rate is limited by dead time. The true elastic rate is measured in KHz.

[34] This is the rate at which the wire chambers were read out.

3.1.4 Acceptance of the Pion Spectrometer

The acceptance of the pion spectrometer is calculated using the STINGO[35] monte–carlo code, (see section 4.1.1). This calculation is performed by throwing pions uniformly in $\cos\theta$ and ϕ at several pion energies; the solid angle acceptance is then just the fraction of pions accepted times the thrown solid angle. Because the polarized target has a $25KG$ magnetic field around it, (see section 3.4.2), the acceptance with the polarized target and that with the unpolarized target are different. However, it has been observed that if the magnetic field of the spectrometer magnet is reversed between the two configurations, it is possible to reasonably match the two acceptances. In this regard, acceptances are calculated for several field strengths between $5.0KG$ and $8.0KG$ and it is found that for a field strength of $6.8KG$ the best matching occurs. In figures 3.5 and 3.6 the acceptance and range of accepted θ_π's are shown for both the polarized and unpolarized configuration.

When the pion spectrometer is coupled to the other two detectors, the effective solid angles are modified. Calculations of the effective solid angle of the pion spectrometer coupled to the photon detector and to both the photon detector and the proton detector are shown in figure 3.7. The curve labeled Ω_γ is the solid angle of the NaI(Tl) array, that labeled Ω_π is the effective solid angle of the pion spectrometer when only coupled to the NaI(Tl) array and the curve labeled $\Omega_{\pi p}$ is the effective solid angle of the pion spectrometer coupled to both the NaI(Tl) and the proton detector. The rapid falloff of the $\Omega_{\pi p}$ curve at high photon energies is due to the protons coming out closer to the beam direction than our proton detector is able to sit. Figures 3.8 and 3.9 show the same sort of calculation, but the first has θ_π restricted to be between 50° and 75° while the second restricts the pions to be between 75° and 105°.

3.2 The Proton Detector

The proton detector is from the SUSY group at SIN[36,37] with modifications for the present experiment. These modifications involve removing multi-wire proportional chambers in

---

[35] This program was written by the author, and is not a standard package.

[36] Th.S. Bauer, *et.al.* SIN Jahresbericht 1981, NL 51.

[37] Rainer Stamminger, Koinzidente Messung der Reaktion $O^{16}(\pi^\pm,\pi^\pm p)$ bei 240 MeV, Ph.D. Thesis from the Friedrich-Alexander-Universität Erlangen-Nürnberg.

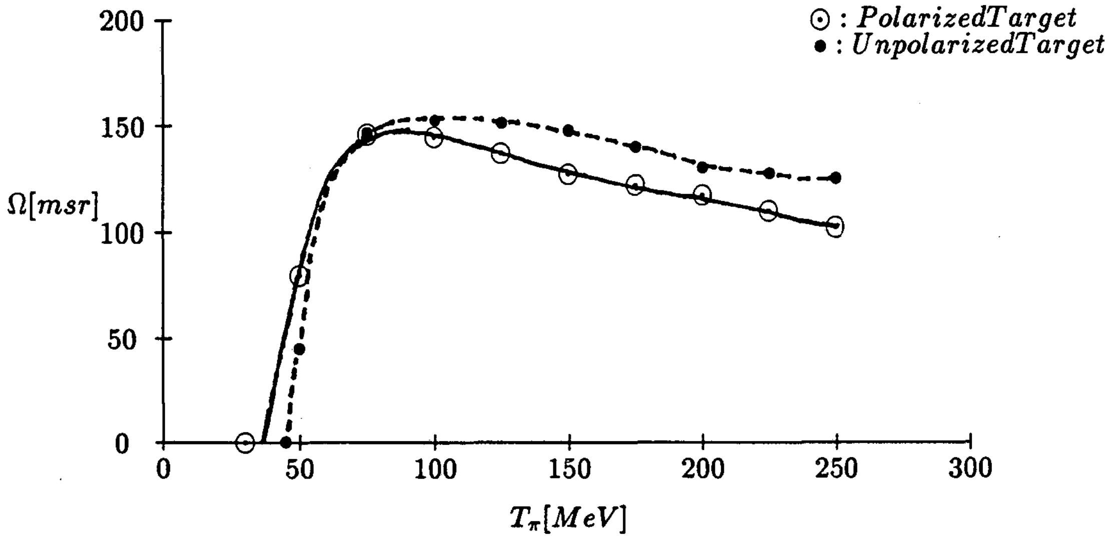

Figure 3.5: Acceptance of pion spectrometer at $B_z = 6.8KG$.

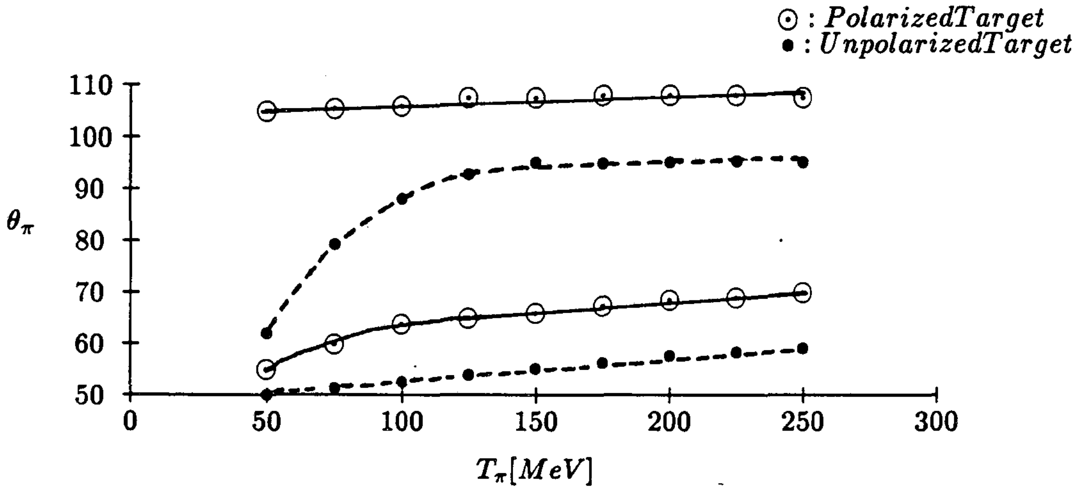

Figure 3.6: Range of accepted θ's in the pion spectrometer.

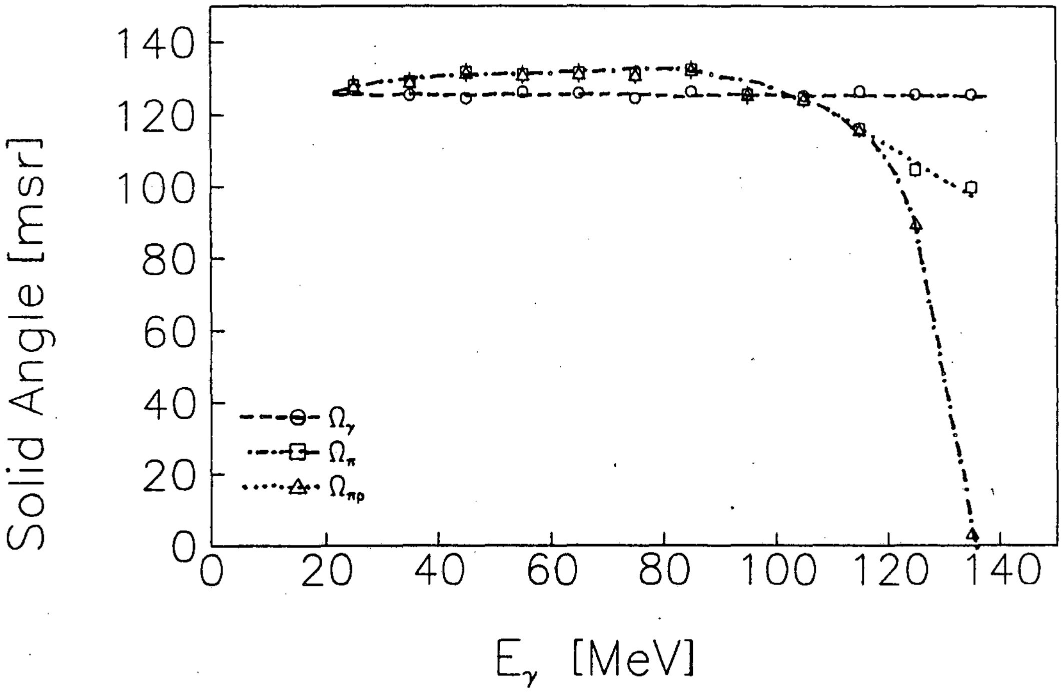

Figure 3.7: Effective solid angle of the NaI(Tl) and the pion spectrometer averaged over all pion angles.

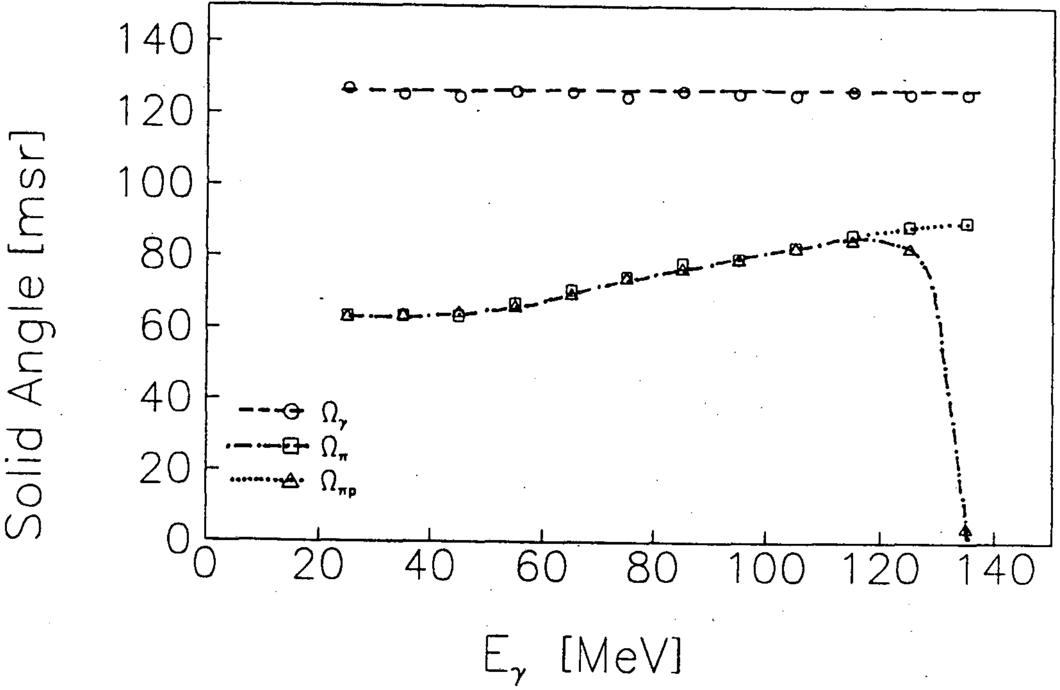

Figure 3.8: Effective solid angle of the NaI(Tl) and the pion spectrometer with $50° < \theta_\pi < 75°$.

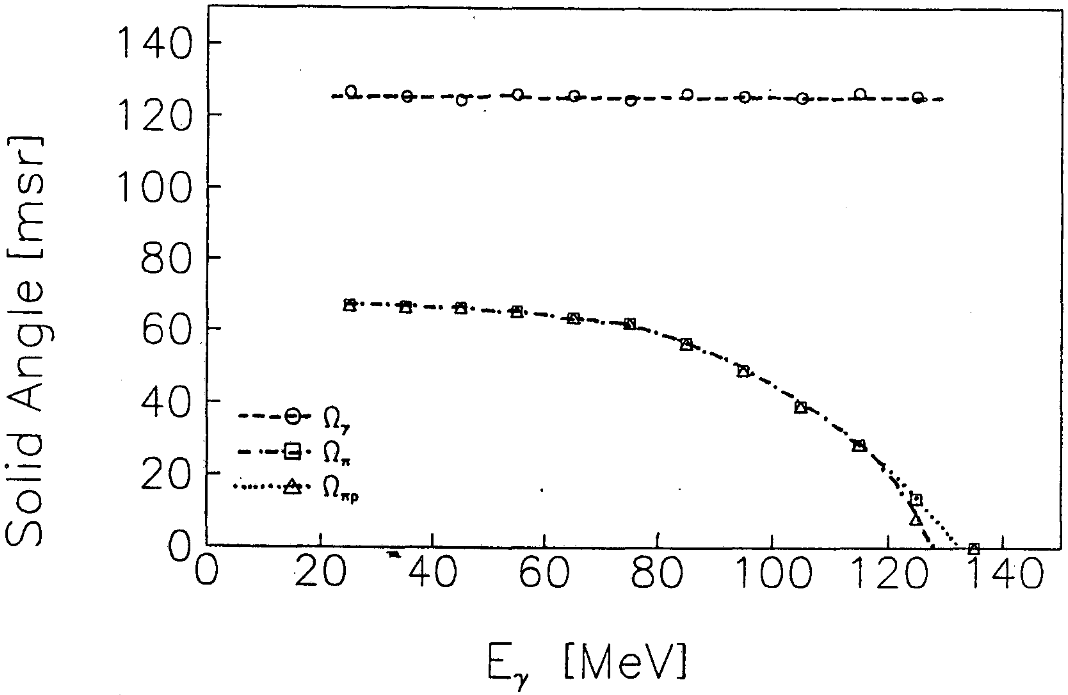

Figure 3.9: Effective solid angle of the NaI(Tl) and the pion spectrometer with $75° < \theta_\pi < 105°$.

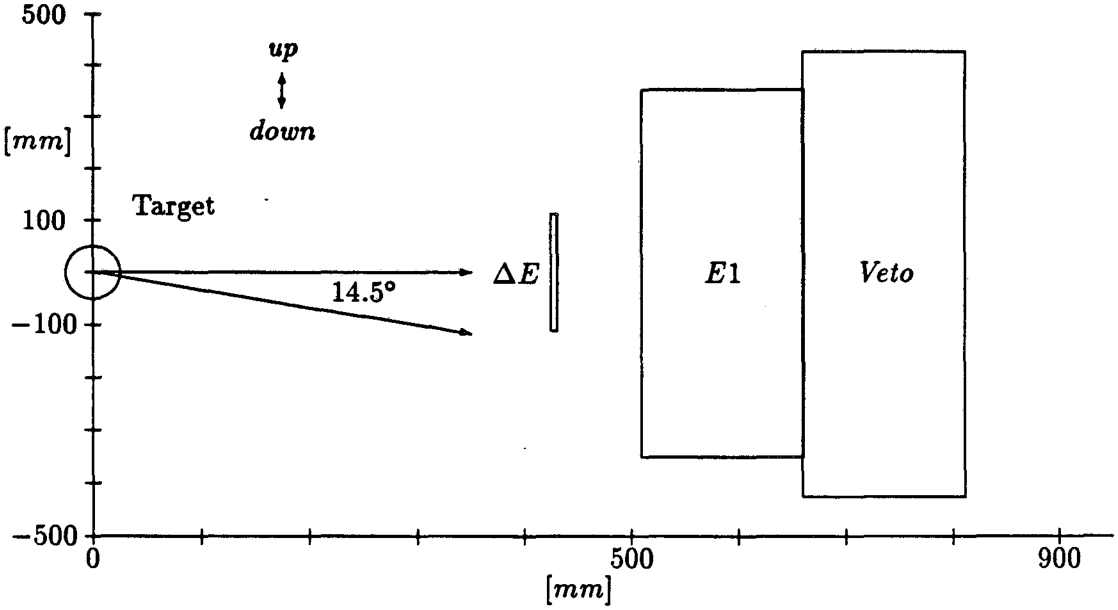

Figure 3.10: The proton detector, side view.

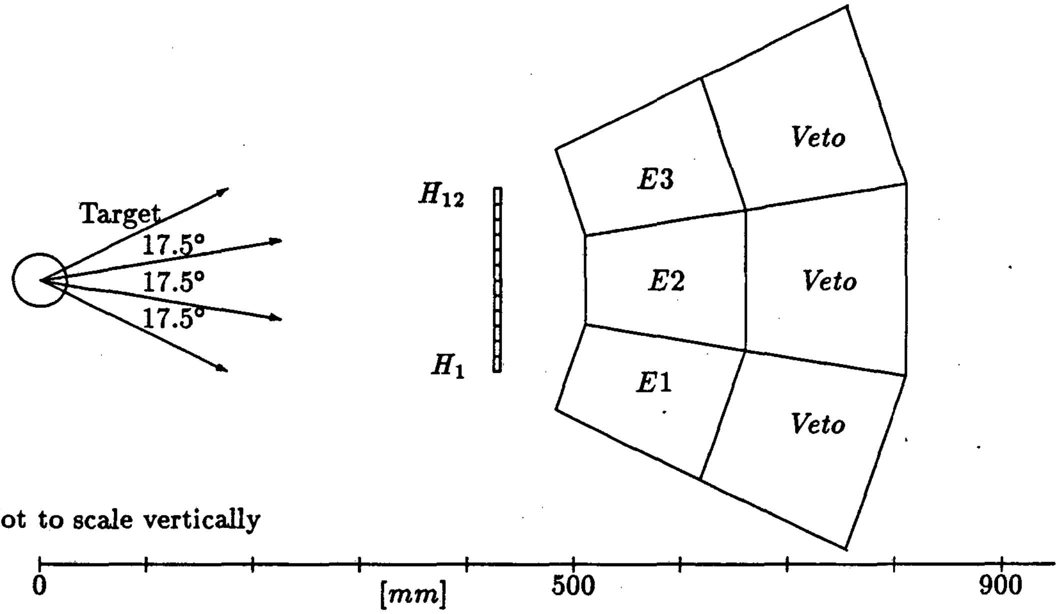

Figure 3.11: The proton detector, top view.

front of all the plastic detectors and replacing 3 large ΔE counters with a hodoscope array of 12 narrow ΔE counters. The proton detector as used in this experiment consists of three parts: a hodoscope of 12 ΔE counters, an array of three large plastic blocks, and an array of three veto counters, (see figure 3.10 and figure 3.11). An event in the proton detector is defined as a hodoscope counter in coincidence with the plastic block behind it firing. Because it is possible to have more than one proton per event, the veto counters are set to both hardware–veto their particular arm, and to set a bit in a pattern unit. This pattern bit is necessary because all counters in the proton arm are read out for a good event; without the pattern information a vetoed arm would appear good to the offline program. There is also pile-up logic which assures that there is no more than one event in a given arm per $150ns$. If a pile-up occurs, another pattern bit is set. The proton trigger electronics is shown in Appendix D.

3.2.1 The Hodoscope Array

After the wire chambers on the original SUSY detector were removed the angular resolution provided by the remainder of the detector was found insufficient for event reconstruction when using the polarized target. In order to correct this problem, the three ΔE counters were replaced with a hodoscope array.

The ΔE hodoscope array consists of 12 $34mm \times 480mm \times 5mm$ strips of NE102A plastic scintillator. Each strip has a Hamamatsu R1450 photomultipler tube on each end. With *ADC* and *TDC* information from both tubes, it is possible to reconstruct the height of the hit to within $\pm 30mm (1\sigma)$. This combined with the $34mm$ width of the counter allows us to reconstruct α_p to within $\pm 1.9°$ and β_p to within $\pm 4.2°$, (see equation 2.1 for definitions of α and β). It is also possible to clearly distinguish between pions and protons by looking at the summed ADC signal from a hodoscope.

3.2.2 The Proton Energy Blocks

The three large blocks labeled $E1$,$E2$ and $E3$ in figure 3.9 are $150mm$ thick blocks of plastic scintillator which will stop protons of energy less than $150MeV$[38]. Each of these counters is viewed from above by a Phillips XP-2030 photomultiplier tube whose output is fed into an ADC. The stability of these counters is monitored with an LED flash system which is fired every few events.

The full acceptance of the proton arm is about $890msr$, but due to height limitations in the Sodium Iodide detector a large amount of the available up-down acceptance is unused. The effective solid angle is then about $225msr$.

Finally, the *E1* block is the rate limiting counter of the experiment. This limitation comes about because this counter is sitting in the muon cone produced from decaying beam pions. The three blocks are able to operate at rates of up to 1MHz without substantial resolution loss, so it is necessary to adjust the incoming pion flux so that there is no more than 1MHz in the *E1* block. (A 1MHz rate leads to 15% losses from pile–up in the detector.)

---

[38] In the original detector, the blocks labeled *VETO* were a second row of energy blocks. The two rows were then able to stop up to 300MeV protons. As the most energetic proton observed in this experiment is under 150MeV, the second row of E blocks was made into veto counters.

3.3 The Gamma Detector

The Photon detector is an array of 64 NaI(Tl) crystals which had previously been used in a measurement of the decay $\pi \rightarrow e\nu\gamma$ at SIN[39,40]. The crystals are 63.5mm by 63.5mm by 400mm or 2.45 radiation lengths on a side and 15.4 radiation lengths long; they are arranged in a square grid, (8 crystals by 8 crystals). Figures 3.11 and 3.12 are drawings of the Sodium Iodide detector. In the center are the 64 NaI crystals, which are surrounded on the top, bottom, left and right by 1cm thick plastic scintillators which are used for vetoing cosmic events. In front of the crystals is a 1cm thick plastic scintillator used to veto charged particles in the detector. Around this scintillator box is a 5cm thick wall of lead, which is contained in a 20cm thick layer of borated polyethylene for slowing and partially stopping neutrons. This layer is inside a 0.15cm thick cadmium layer which is all contained in a 10cm thick lead box. The crystals are each looked at with a Philips 2202 photomultiplier tube. Stability of the tubes can be maintained via a flash system which is optically connected to each of the crystals. There is also a 65^{th} crystal which monitors the stability of the flash system by looking at a Cs source.

The gamma detector is centered at $\alpha = 240°$ and $\beta = 0°$ at a radius of 109cm from the target center. Because a gamma which is centered in one of the 28 crystals around the outside of the detector has a high chance of having some of its shower exit the crystal array, only gammas which are centered in the center 36 (6 by 6) crystals are accepted, see figure 3.12. This limits photons to the range $210.1° \leq \alpha \leq 229.9°$ and $-9.9° \leq \beta \leq 9.9°$, which gives a solid angle for photons of about 126 msr.

3.4 The Targets

Two different hydrogen targets have been utilized in this experiment, a polarized target and a liquid hydrogen target. In principle it would have been possible to use the polarized target for both the polarized and unpolarized measurements. However, by using just a liquid hydrogen target in the unpolarized case, the signal was much cleaner – there seemed

---

[39] Aurillio Bay, *et.al*, **SIN Physics Report No. 3**, 58 (April 1981), SIN experiment R-78-13.

[40] Aurillio Bay, **Détermination du rapport des facteurs de forms axial et vectoriel du Meson PI par la mesure de la désintégration $\pi^+ \rightarrow e^+\nu\gamma$ et contribution à la réalisation d'un détecteur de photons.** Ph.D. Thesis from Institut de Physique Nucléaire, Université de Lausanne, 1986.

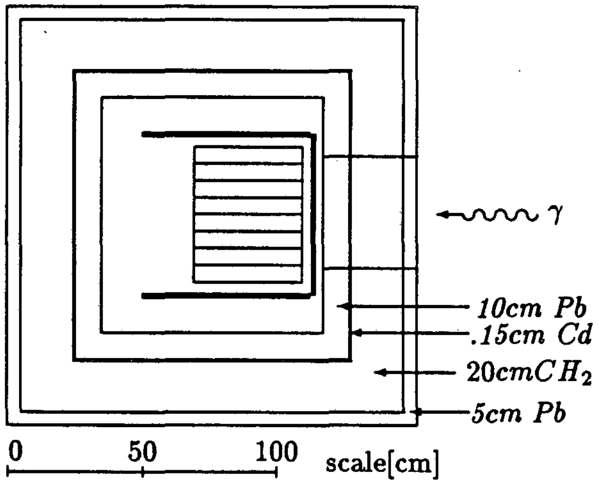

Figure 3.12: The sodium iodide detector, top view.

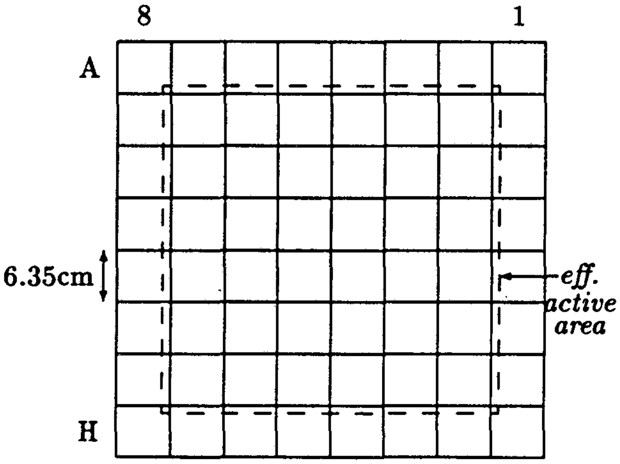

Figure 3.13: The sodium iodide detector, front view.

no reason to make the measurement more difficult by adding more material, and a second magnetic field.

3.4.1 The Liquid Hydrogen Target

The liquid hydrogen target is an oval shaped mylar vessel as shown in figures 3.14 and 3.15. The target is built from three pieces of formed mylar: two end domes, a hollow cylinder and the filling pipe. The domes are formed from 178μm, (7mil), mylar that is heated and sucked into a form. The final dome is about 76μm, (3mil) thick at the center, and remains close to 178μm thick around the lower edge. The cylinder is made from a sheet of 127μm, (5mil), thick mylar rolled into a cylinder. The seam is located along the target's bottom to minimize variations of thickness in the exit particle paths. Finally, the filling joint is made from 127μm ,(5mil), thick mylar and is positioned so as to be above the beam, and out of particles way. The target is 140mm long, and 45mm in diameter. The target contains 199cm^3 of liquid hydrogen, and presents 1$\frac{gm}{cm^2}$ of liquid hydrogen to the incoming pion beam.

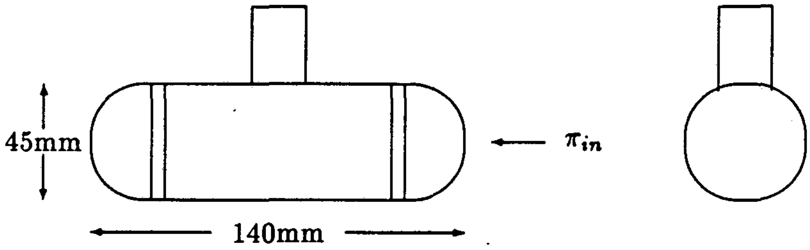

Figure 3.14: The liquid hydrogen target vessel.

3.4.2 The Polarized Target

The polarized target is from the SIN polarized target group[41]. The target material is a 2cm in diameter by 3cm high cylinder of butanol, $C_4H_{10}O$ which sits in the center of a 25KG field produced by a superconducting Helmholtz coil. The target is maintained at a temperature of 0.5 K, and a proton polarization of 70 to 75% is obtained and maintained through the use of a nuclear magnetic resonance system. The target material is enclosed in a 50μm thick Cu box which is inside a 2cm radius, 100μm thick Fe cylinder. This is

---

[41] SIN Users' Handbook p.105 (1981).

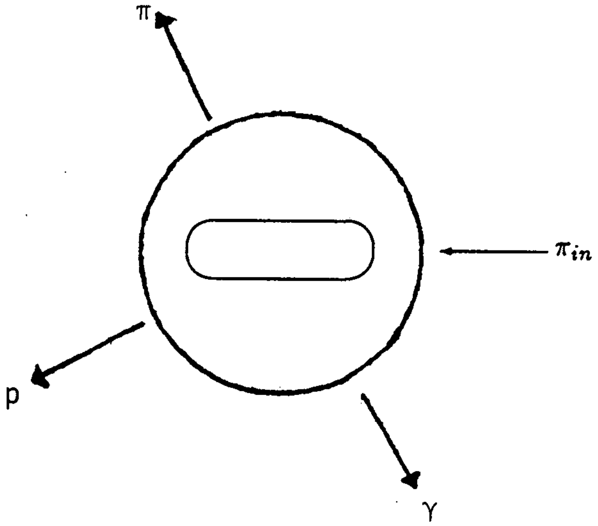

Figure 3.15: The liquid hydrogen target containment vessel.

surrounded by by two $5\mu m$ thick Al foils at 11.5 and 12.5cm, and a $70\mu m$ thick kapton sheet at 13.5 cm. Only the free protons in the target are polarized, these constituting about 21.5% of all protons in the target. Table 3.2 shows the constituents of the polarized target.

Material	Protons	Neutrons
H	21.5%	none
C	51.6%	64.5%
O	17.7%	21.4%
Cu and Fe	9.7%	14.1%

Table 3.3: Fraction of target nuclei in all materials in the polarized target.

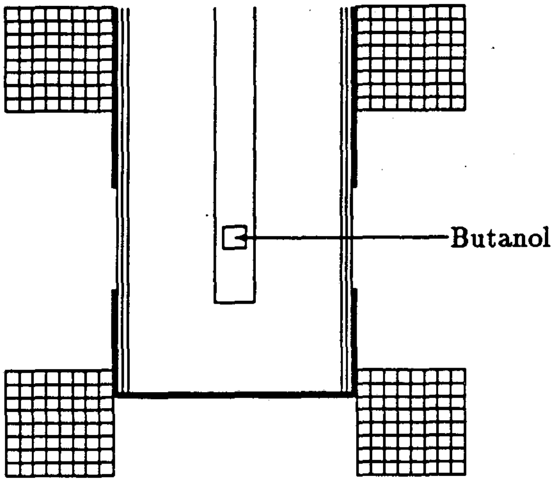

Figure 3.16: The polarized proton target.

Chapter 4

The Calibration of Detectors

4.1 Calibration of the Pion Spectrometer

Reconstruction of the pion is done with a set of tracking functions. The arguments of the functions are the fired wires in an event, and the values of the functions are the pion momentum, angles and target traceback. Calibration of the pion spectrometer then consists of determining these functions.

In order to obtain the tracking functions, one generates a large number of monte–carlo pion trajectories through the spectrometer. These trajectories are chosen to fill the available phase-space of the spectrometer. For each of these monte–carlo tracks one records the hit wire in each plane, the momentum of the pion, the original angle of the pion and the point from which the pion came in the target. With this information for a few thousand tracks, polynomials of the wire numbers can be fit to the other recorded information. Using the polynomials it is possible to reconstruct the monte–carlo pion momentum to $\pm 1.8 \frac{MeV}{c} (1\sigma)$ over all accepted momentum. The θ and ϕ angles can be reconstructed to about $\pm 0.34^\circ (1\sigma)$, (this includes effects due to multiple scattering in the detector), and the target traceback is good to about $\pm 1mm(1\sigma)$. This procedure depends upon the monte–carlo, and very accurate knowledge of the wire chamber positions. Finally, because the pion spectrometer is the only arm that gives us a target traceback, we are unable to determine the depth in the target at which the interaction took place. This of course leads to some broadening of energy peaks, particularly in the proton detector.

4.1.1 The Monte–carlo

The monte–carlo program STINGO was written by the author to study particle trajectories in the pion arm of the apparatus. However, it has been extended from its initial form to cover all three arms of the apparatus; this made it possible to generate full monte–carlo events, which could be run through the analysis code. The monte–carlo includes effects for both energy loss and multiple scattering in all substances in the detector; switches are provided for individually turning on and off both these effects in all the material.

Tracking of particles is performed using a Runge-Kutta[42] integration procedure on the equations of motion.

$$\frac{d\vec{\mathbf{p}}}{dt} = \frac{eZ}{c}\vec{\mathbf{u}} \times \vec{\mathbf{B}}$$

The step size used by the routine is varied depending on the particle momentum and the magnetic field strength so that the arc traversed by the particle never sweeps out more than 0.3°. This limitation minimizes errors coming from the particle *sliding* off its true track in strong magnetic fields.

$$\Delta s = \min\left[8mm, \frac{\pi}{180}\cdot 0.30^\circ \cdot \frac{|\vec{\mathbf{p}}|}{e\,|\vec{\mathbf{B}}|}\right]$$

The magnetic field is obtained from a field map stored in computer memory. The map has been measured at 8.0KG and is linearly scaled to the value used in the experiment, (a plot of this map can be found in section 3.1.1). When the magnet is far below saturation, the field is found to be independent of the y coordinate in the magnet, and is symmetric in the four quadrants of the $x - z$ plane. As such, the map for only one quadrant is stored, and the field in the other three is obtained through symmetry arguments. The map grid is 1cm by 1cm, and contains 22 points in the z direction and 75 points in the x direction. Finally, the map has been smoothed by requiring that $\nabla^2 B = 0$ at all points within the volume; this smoothing will smear mapping errors out over a large region, allowing one to do more accurate tracking.

Within the mapped volume, all fields are interpolated through 2^{nd} order, see equation 4.1 . Application of Maxwell's equations to the expansion allows one to cut down the number of calculations performed by the computer. Extrapolation in the z direction is also

---

[42] Kendall E. Atkinson **An Introduction to Numerical Analysis**, p.366 John Wiley and Sons, New York (1978).

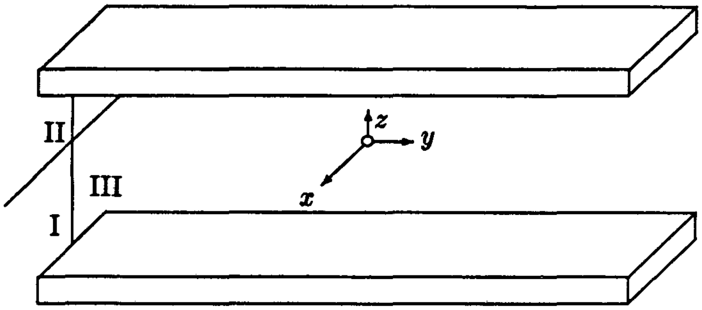

Figure 4.1: Coordinates of spectrometer magnet.

performed with the same routines. In the z direction it is safe to make this assumption because if a particle gets more than 2cm above or below the map, it will miss one or more of the detector planes, and thereby be lost.

$$B_i(\vec{\mathbf{x}}+\delta\vec{\mathbf{x}}) = B_i(\vec{\mathbf{x}}) + \vec{\nabla}B_i\cdot\delta\vec{\mathbf{x}} + \frac{1}{2}\vec{\nabla}(\vec{\nabla}B_i\cdot\delta\vec{\mathbf{x}})\cdot\delta\vec{\mathbf{x}} \tag{4.1}$$

Extrapolation beyond the end of the map in the x direction is done with an elevation dependent linear falloff. This correction is important for very accurate tracking of pions in the region between the target and the second wire chamber. If one ignores the field in this region, then a systematic shift of about $0.4MeV/c$ occurs in the pion momentum. This correction agrees well with a calculated map for the region performed for the polarized experiment.

Finally, in order that the monte–carlo be accurate, the position of the wire chambers, and in particular the wires themselves need to be well known. The position of the wires within a chamber have been accurately measured with a walking microscope while the chambers were being cleaned. These measurements are summarized for each plane in Table C.1, and typically give the position of a wire within a given plane to better than 0.5mm (1σ). The physical positions of each of the chambers were surveyed at the end of each run. Also during the run a set of pion data was taken with all magnets turned off. With this straight–through data it was then possible to check all of the position measurements, and make any necessary corrections. A discussion of this analysis is found in the next section.

4.1.2 The Straight–Through Analysis

In order to locate the positions of the wire chambers to the level of ±0.5mm, we performed a straight–through analysis to check the surveyed chamber positions. The data for the straight through analysis was obtained by turning the spectrometer magnet off, and triggering on a scattered pion. For this analysis, a program STRAIGHTS was written by the author. The program first looked at the chamber data from an event and reconstructed all the triangles in the four wire chambers, (see Appendix C). It then selected only those events which had exactly one triangle per chamber. This criteria was imposed to prevent any confusion in identifying which triangles belonged to a given track.

The (x, y, z) coordinate of each triangle was then calculated using the information found in tables C4 to C9. It was found that the elevation in the wire chambers had a calculable systematic error dependent on the angle at which the pion trajectory crossed the chamber face. This was essentially a parallax effect arising from the finite thickness of the chambers, and the fact that the planes that determine elevation were at $+60°$ and $-60°$. This correction is given as

$$\Delta y = -2 \cdot \frac{l}{a} \cdot \cot\theta_{\pi} \cdot \sin\theta_{w}$$

where l is the distance between wire planes, a is the distance between wires, θ_{π} is the angle between the π and the face of the chamber and θ_{w} is $60°$.

The program then looks at the back two chambers and predicts the position in the second chamber. The positions of these three chambers are aligned with respect to each other to give the best straight line through them by means of a least squares fit. With this information, we then project back to the target with the back three chambers. Around the target was a vacuum window which provided a sharp peak in front of and behind the target. We then allowed the measured position of the magnet center and the angle at which the magnet was rotated to best match straight through position to the surveyed position of the target. Finally we minimized the difference between the position predicted in the first chamber from the back three chambers and that measured in the first chamber by varying the position of the first chamber. The deviations between the measured and the straight through positions were generally within the survey error, so we used the results of the straight through analysis as input to the monte–carlo program.

4.1.3 Pion Reconstruction

After the monte–carlo tracks are generated, a set of polynomial functions are generated that allow one to input *wire numbers* and get as output *momentum*, *angles* and *target traceback*. The program that performs this is a multidimensional correlation and fitting code called ERIKA[43]. Given a large data sample, ERIKA first performs a *Principal Component Analysis*[44,45], and then fits products of either Chebychev, Hermite or Legendre Polynomials to the data. A discussion of *Principal Component Analysis* can be found in Appendix A, and the fitting of polynomials is discussed in Appendix B. The fits are generated using monte–carlo data in which multiple scattering has been turned off, and only the mean energy loss of particles has been considered. When checking the fits, one uses monte–carlo data in which multiple scattering and Landau smearing of the energy loss is included. The results so obtained give us the resolution of each of the desired quantities.

The uncertainty in reconstructed pion momentum associated with the uncertainty of wire position is checked by generating monte–carlo data in which one or more of the wire planes have been shifted from their true positions. We found that to keep this contribution to the momentum resolution at the level of 1%, (1σ), we had to know the horizontal position of all chambers to within ±2.0mm. The largest effect was observed in chamber four, which was expected, as the vector between chambers 3 and 4 essentially determines the pion momentum. Any uncertainty in the chamber position enters the momentum as a systematic shift, and not as a random error.

4.1.4 Track Finding

Reconstruction of the pion is carried out by the track finder program. The data are first checked to make sure that an AB array element fired within the allowed time of flight windows. If an event has at least one good AB paddle, we examine the wire chamber

---

[43] The ERIKA code was originally written by Harald Von Fellenberg at the Physik-Institut der Universität Zürich for use with the SIN Pair Spectrometer. It has been documented and altered by the author for the present experiment.

[44] H. Wind **Principal Component Analysis and its Application to Track Finding** printed in **Formulae and Methods in Experimental Data Evaluation, Vol 3**, CERN-Service d'information Scientifique-RD1617-2000 décembre 1983.

[45] Helmut Eichinger **Review of Track Fitting Methods in Counter Experiments**, CERN 81-06 22-June-1981.

information. The chambers are searched for sets of wires in each of the three planes which form triangles, (see Appendix C). All found triangles are then arranged in order of size, smallest to largest. If a big triangle shares a wire with a smaller triangle, we remove the shared wire from the larger one. This then leaves us with the set of smallest triangles which have no wires in common. Next we examine the unused wires to determine if they form crosses. If so we calculate which wire would be needed to complete a size zero triangle and generate it. These generated triangles are then placed at the bottom of the list of good triangles. In this way we get a list of triangles for each of the four chambers. During the $\pi p \rightarrow \pi p \gamma$ experiment we had on the average 1.02 to 1.2 triangles per chamber per event.

In order to determine which triangles could possibly form a good event, we loop over all possible combinations of triangles in the four chambers. First we check to see if the position of the triangle in the fourth chamber matches an AB paddle that fired within the time of flight window. If so then we examine a straight line traceback to the target from the first two chambers and require that it be close to the target position. If both of these conditions are met, then we pass the set of 12 wires found to a program which rotates them into a set of Principal components, (see Appendix A). This routine returns the 12 coordinates of the hit in the principal component space arranged from most significant to least significant. If the track is real, then it should be uniquely determined by exactly 6 coordinates, $(x_0, y_0, z_0, p_x, p_y, p_z)$. What this means is that for a real track, the first 6 PCA coordinates should be non zero, and the remaining 6 should be very small. By forming a geometric sum of the smallest 5 PCA coordinates, we have a quantity which should be very small for good tracks, and random for other things. We then arrange all tracks found in order of this residual sum.

With all of these located tracks, we then use the ERIKA coefficients to reconstruct a target traceback. All tracks that reconstruct to inside the target volume then have their momentum and angles reconstructed. We have not prevented the tracks from sharing triangles at this level. This is because if the two triangles are in the first wire chamber, they are quite likely rather close together. The only criteria we have to determine which one is more likely is to correlate them with the other particles detected. This is done in a later program. Finally, the track finding efficiency is estimated from monte–carlo events to be about $95 \pm 2\%$ and is measured using the elastic πp cross–sections to be 94%.

4.1.5 Resolution of the Pion Spectrometer

The resolution of the pion spectrometer is measured using elastic events. We reconstruct the pions from an elastic run (triggered on $\pi p \rightarrow \pi p$ rather than $\pi p \rightarrow \pi p\gamma$) and the difference between the reconstructed pion momentum and that of an elastic pion at the measured angle, (θ_π) is formed. This quantity is then a measure of the momentum resolution folded with the angular resolution and the resolution in the incident pion momentum. We also form a quantity which is the difference between the measured pion angle and the pion angle as expected for an elastic pion of the measured momentum. Both of these quantities are plotted in figure 4.2; we see that $\Delta p_\pi = 6.49\text{MeV/c}$ (FWHM) and $\Delta\theta_\pi = 3.4°$ (FWHM). These two quantities are not independent of each other, but are coupled through the equation

$$p_\pi = \frac{(m_\pi^2 + m_p E_{in})\cos\theta_\pi \pm (m_p + E_{in})\sqrt{m_p^2 - m_\pi^2 \sin^2\theta_\pi}}{\frac{1}{P_{in}}(E_{in} + m_p)^2 - P_{in}\cos^2\theta_\pi},$$

which can be approximated within our magnet acceptance as

$$p_\pi = 448.9\frac{MeV}{c} - 1.874 \cdot \theta_\pi[degrees].$$

This says that $\Delta p_\pi = -1.874\Delta\theta_\pi$, which agrees quite well with the ratio of 1.87 obtained from figure 4.2. In order to extract the true resolutions, we need an independent measure of either quantity.

A good estimate for the uncertainty in the pion angle can be obtained by examining the resolution of monte–carlo data with multiple scattering included. This effect is found to give $\Delta\theta_\pi = 0.34°$ (1σ). There is also a contribution to this angle from the incident pion direction which was measured as $\Delta\theta_{in} = 0.36°$ (1σ). Combining these effects gives us that $\Delta\theta_\pi = 1.16°$, (FWHM). This then gives a contribution to the momentum of 2.17MeV/c (FWHM). The contribution from the uncertainty in the incident beam momentum is 2.83MeV/c FWHM. Finally there is a contribution from the depth in the target at which the pion originated. This arises because we only have one arm giving us a target traceback, and this leads to an uncertainty in the depth. This contributes about 1.MeV/c to the width of the pion momentum. From all of this we obtain that the pion momentum resolution is 5.33 MeV/c at (FWHM). The monte–carlo predicts a resolution of 4.21 MeV/c, but this is made ignoring multiple scattering in the spectrometer.

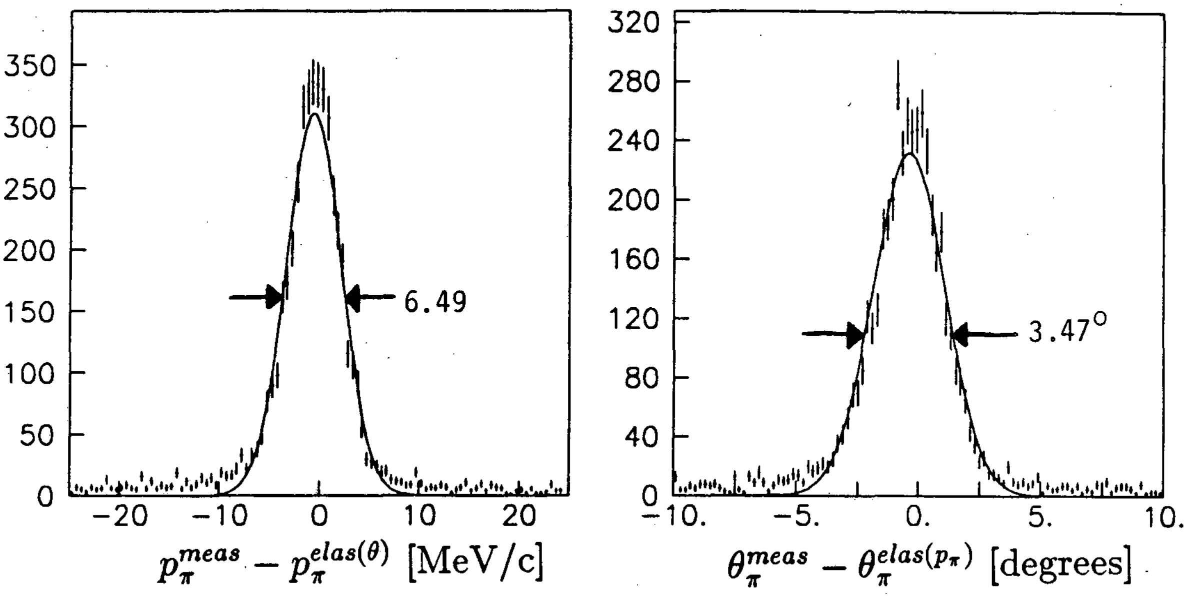

Figure 4.2: The difference between the measured pion momentum and angles, and that of an elastic pion.

4.1.6 The Target Position

The uncertainty in the target position is calculated to be ±1mm from the monte–carlo. In order to measure this, we examined the target traceback for an empty target run. This traceback, and its projection along the beam axis are shown in figure 4.3. We can get a very good idea of the resolution along the axis by measuring the reconstructed widths of the entrance and exit windows of the target. This gives us that traceback is better than ±3mm (1σ). This is worse than the monte–carlo prediction because we have no depth information on the event.

4.2 Momentum of the Incoming Pion Beam

The[46] nominal momentum of the incident pions was given by an SIN calculation as $421 \pm 2MeV/c$ with $\frac{\Delta p}{p} = 0.293\%$. In order to check this number, a measurement was made of the time–

---

[46] This section is a synopsis of **A Momentum Measurement of the $\Pi E1$–Beamline** by Andreas Bosshard.

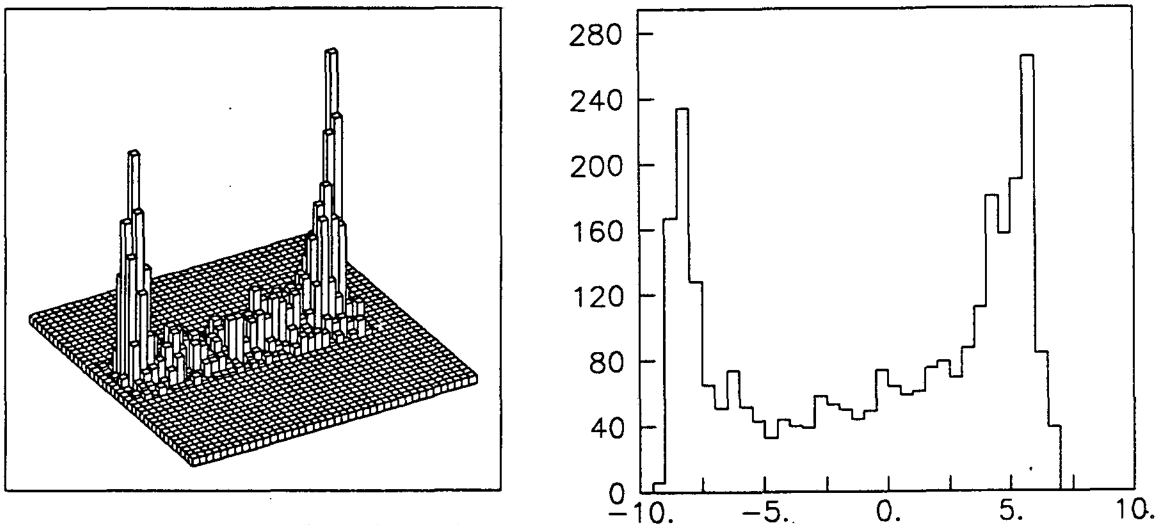

Target traceback, elevation
versus z position.

Figure 4.3: The target traceback for an empty target. The two two peaks are entrance and exit windows.

of–flight difference between pions and protons in the beamline. The measured time of flight difference can be given as

$$\tau_p - \tau_\pi = -(y_p - y_\pi)\cdot C + (n_p - n_\pi)\cdot \tau_0$$

where τ_0 is th cyclotron frequency (19.750 ns), n_p and n_π are the number of τ_0 periods that the protons and pions travel, y_p and y_π are the positions of the proton and pion TDC peaks and C is the TDC calibration constant. One then calculates the expected time–of–flight difference based on pion and proton momenta, and the material in the beam. From this one defines an error, ϵ

$$\epsilon = (x_p - x_\pi) + (y_p - y_\pi)\cdot C - (n_p - n_\pi)\cdot \tau_0$$

This ϵ is then minimized to give the momentum with the result that the beamline momentum is $421.60 MeV/c$ and the pion momentum entering the target is $417.79 \pm 1.2 MeV/c$. This momentum is lower because of energy loss in carbon absorbers for removing beam protons.

The angular resolution of the beam was measured by moving a small wire along the path of the incident pion beam and measuring its vertical and horizontal width at several positions. This gave us that the incident beam had an angular width of 0.850° (FWHM).

We also obtained a measurement of the density of the liquid hydrogen target by examining the energy loss of protons passing through it. This analysis gives us that $\rho_{H_2} = 0.0762 \pm 0.0043 g/cm^2$. This is compared to the true density of liquid hydrogen of $0.0727 \pm 0.0014 g/cm^2$ as an average over all temperatures at which hydrogen is liquid.

4.3 Calibration of the Proton Detector

The proton detector measures energy by stopping the protons in large blocks of plastic scintillator. Position and $\frac{dE}{dx}$ are measured by using the hodoscope counters in front of the plastic blocks. The large plastic blocks are looked at by one photomultipler tube from above whose output is fed into an ADC module. This gives a measurement E^i_{adc}. The hodoscope counters are each looked at by two photomultiplier tubes, one from above and one from below. The output from these tubes are fed into ADC and TDC modules which then give four measurements: $H^{j\uparrow}_{adc}$, $H^{j\downarrow}_{adc}$, $H^{j\uparrow}_{tdc}$ and $H^{j\downarrow}_{tdc}$. These quantities then need to be turned into an energy and position measurement.

4.3.1 Position of the Proton

If one looks at the hodoscope as an $x - y$ plane, then the x coordinate is just given by the number of the hodoscope counter which fired. The y position is obtained by examining the time difference between the signal from the top and bottom of the strip. The signals from the top and bottom tube are fed into constant fraction discriminators, (CFD) , and the output from both goes to a mean timer. The mean time signal is used for triggering, and the CFD signals go to the TDC's to generate the up and down times. If one defines

$$\Delta t_j = H^{j\uparrow}_{tdc} - H^{j\downarrow}_{tdc},$$

then the elevation in the counter is given by

$$y_j = \alpha_j + \beta_j \cdot \Delta t_j. \tag{4.2}$$

We obtained the alpha and beta coefficients for each of the 12 hodoscopes by placing a Ru^{106} source in front of the array at several different heights. The best straight–line fits all have slopes which are 5cm/ns, while the α terms vary from counter to counter. The elevation resolution that we can obtain with this method is $\pm$3cm (1σ).

4.3.2 The Energy of the Proton

The hodoscope array also gives us $\frac{dE}{dx}$ in 5mm of plastic scintillator of the particles, while the large plastic blocks measure most of the energy of the proton. The total energy of the proton can be expressed as the sum:

$$E = E_{plastic} + dE_{Hodo} + \Delta E_{target} + \Delta E_{air} + \Delta E_{wrappings}$$

where $E_{plastic}$ and dE_{hodo} are measured in the detector. The energy lost in the target, air and counter wrappings are then calculated based on what is known about the proton from the detector. One can then distinguish between pions and protons in the proton detector by looking at the energy deposited in the hodoscope array. The pions and muons are all minimum ionizing while the protons are slower than minimum ionizing protons. The time of flight of the proton is not sufficient to distinguish between anything in the hodoscope, this being because the flight path is only 41cm in length.

In order to obtain $\frac{dE}{dx}$ from the hodoscope counter and the energy lost in the plastic blocks, we use the following parameterizations:

$$\frac{dE}{dx} \cdot 5mm = A_j \cdot (H^{j\uparrow}_{adc} + H^{j\downarrow}_{adc}) + B_j \cdot (H^{j\uparrow}_{adc} - H^{j\downarrow}_{adc}) \tag{4.3}$$

$$E_{plastic} = D_j \cdot (E^{j}_{adc} - p^{j}) \tag{4.4}$$

Where the A, B and D coefficients are determined by looking at elastic events in the pion and proton arms of the detector and p^j is a pedestal subtraction to the ADC. The pedestal subtraction is performed before the event is written to tape, and is ignored from here on. To calibrate the proton detector, we take elastic runs and reconstruct all events which have pions near elastic pions, ($p_\pi - p_\pi^{elastic}$ is small). We then calculate the expected energy of an elastic proton that will balance the pion. Next we calculate how much energy this proton will loose between the center of the target and the hodoscope array, and finally calculate how much energy it would deposit in the hodoscope and proton counter. By repeating this procedure for the several thousand events in a typical elastic run we obtain a set of calibrations for hodoscopes 5 through 12, and proton counters 2 and 3. In the nominal position of the proton detector, we do not see elastic protons in the first counter. In order to calibrate it, we have taken runs with the first proton counter rolled around to the position of the second counter. This then yields the remaining constants.

During the analysis of the data it is necessary to monitor the gains of the phototubes on the three plastic blocks. This is done by sampling the ADC spectra of blocks 2 and 3 for very narrow bands in pion momentum and angle. It is not possible to do this for block 1 as no elastic events are detected there. For these sampled pions we plot the ADC spectra in the proton counters and compare it to the same spectra obtained during calibration. We also monitor the position of the peak in the LED spectra for each of the three counters. We find that the variations in the LED follow quite closely those from the sampled pions, and as such use the LED spectra to stabilize the gain in proton 1. We find that the gain factors change by no more than 8% from their calibrated values in any of the runs.

4.3.3 Proton Reconstruction

Reconstruction of the protons is done by first searching through the hodoscope array to identify all bars which fired, and all which fired within allowed time of flights and pulse height windows. Next a search is made of the three proton blocks to identify which ones fired and did not have their veto or pile–up bits set. The fired proton blocks were then arranged in order of energy deposited in them, most to least. We then started at the top of the list of fired proton blocks and tried to find a hodoscope which fired within the allowed time of flight windows and which sat in front of the fired block. For this search, hodoscope bars 1 to 5 were allowed to match proton one, bars 4 to 9 were allowed to match proton 2 and bars 8 to 12 were allowed to match proton 3. We did not allow hodoscopes to be shared between proton blocks, so once one that matched was found, it was removed from the allowed search list. This then gave us a set of nominal protons.

For a small percentage of the protons, it was possible to see energy deposited in either two proton blocks or two hodoscopes. In order to see if this had happened, and to correct for it we initiated the following search. If the proton contains a hodoscope which could be shared between two proton blocks, then we checked the second block to see if any energy was seen in it. If so, we checked the veto and pile–up bits for that block to make sure they didn't fire, and finally checked to make sure that no hodoscopes in front of the block fired at any time during the event, (not just within the allowed time of flight windows). If these conditions were all satisfied, we added the energy seen in this bar into the event energy. We did not try to correct for the energy lost in the wrappings between the blocks. Finally, we examined the hodoscopes adjacent to the fired hodoscope to see if they fired within the allowed time of flight window. If so, then the energy deposited in them was also added into the event.

Finally, we calculated the x and z position at the center of the fired hodoscope, and left the elevation at 0. The energy in the allowed blocks and hodoscopes was then summed and returned to the main program. Corrections for the energy lost in the liquid hydrogen target, mylar windows, foils and the air were calculated in the main program using the pion to provide a vertex position in the target. Because the depth in the target from which the event came is unknown, we calculated the corrections at several points along the pion trajectory and averaged them. However, the angle, α_p was calculated assuming that the event came from exactly on the beam axis.

4.3.4 Resolution of the Proton Detector

In the proton detector, we have a somewhat more direct measurement of the energy resolution coming from the calibration data. Figure 4.4 is a plot of the predicted energy from the pion arm of the spectrometer minus the calculated energy deposited in the proton E counter. The width of 9.6MeV has the resolution of the incident beam energy, (2.66MeV FWHM), the pion energy resolution, (5.8MeV FWHM) and the effects due to uncertainty in the target depth, (6.0MeV FWHM) folded into it. When these are unfolded, we arrive at a width of 3.9MeV FWHM at 82MeV, which is about 4.8% FWHM. This resolution does not include the the resolution of the hodoscope array which makes things somewhat worse.

It is clear that a large source of uncertainty in the proton energy comes from the uncertainty in target depth. In correcting for the energy lost by the proton when leaving the target, we average the energy loss over the trajectory of the pion through the target. This prevents introducing systematic shifts in the correction that would arise if we had assumed that the proton just came from the center of the target.

Finally, we can also look at the resolution of the entire proton detector in the same manner that we examined the pion spectrometer. In figure 4.5 is plotted the difference between the measured proton momentum and the momentum of an elastic proton at the measured proton angle, and the same difference in the measured and predicted angle, while in figure 4.6 are plotted the resulting energy balance and the difference between measured and predicted angle of the proton in the πp system. The angular resolution of the proton detector can be obtained directly from figure 4.6 as 3.80°FWHM, which can be compared to

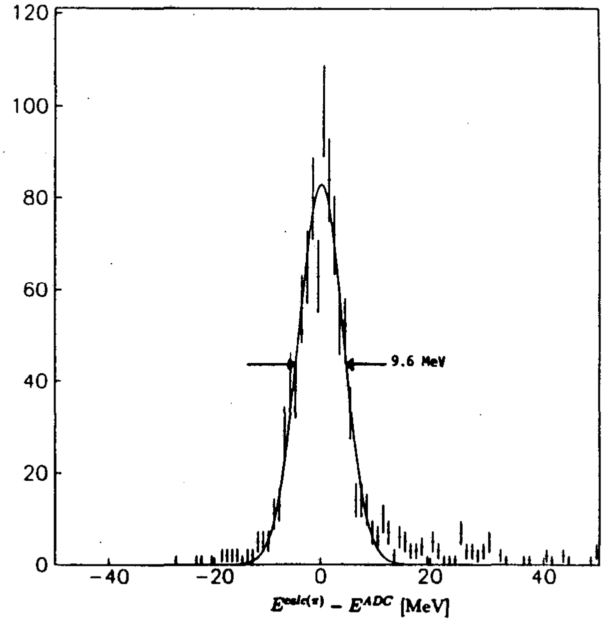

Figure 4.4: The difference between the energy calculated from the pion and that obtained from the ADC in the proton detector.

the angular width of a hodoscope strip of 4.75°. The energy resolution contains the same contributions as before, giving us a 5.23MeV FWHM at 100 MeV, or 5.2% FWHM.

4.4 Calibration of the Gamma Detector

The energy deposited in one of the 64 NaI crystals is given by

$$E_i = k_i \cdot (ADC_i - p_i)$$

where ADC_i is the ADC channel number for the crystal, k_i is the linear conversion from ADC channel to energy and p_i is a pedestal subtraction which is made before the event is written to tape. To obtain the calibration constants for each of the crystals, we look at several sources of photons which vary in energy between 662KeV and 129MeV.

4.4.1 Individual Crystal Calibrations

For low energy photons, gammas from the radioactive decay of ^{137}Cs (0.6616 MeV) and ^{88}Y (0.8980 and 1.8361 MeV) are used. When this data is taken, the attenuation in the input line to the ADC is decreased by a factor of 10. This causes the gamma energies to appear as 6.616, 8.980 and 18.361 MeV. Unfortunately, during the unpolarized run the ^{88}Y

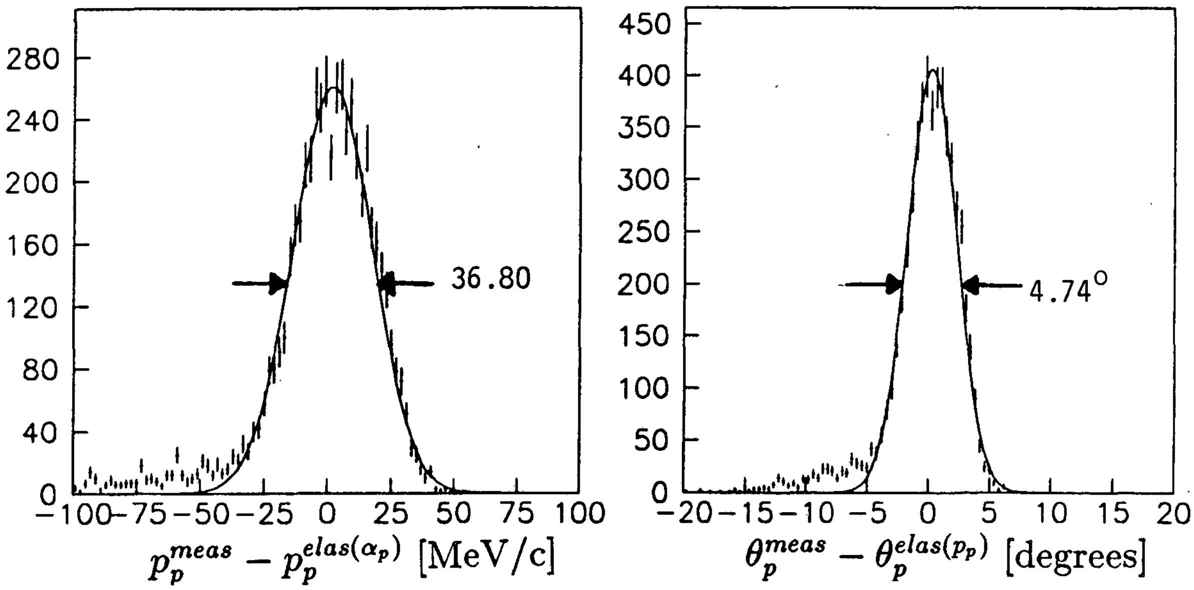

Figure 4.5: The difference between the measured proton momentum and angles from those of an elastic proton.

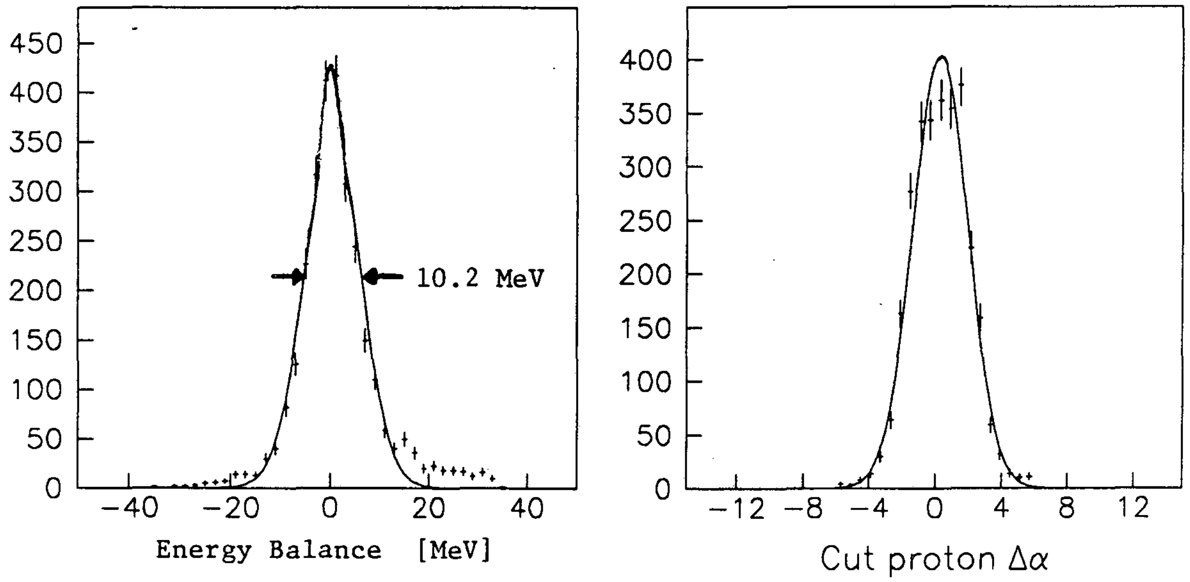

Figure 4.6: The overall energy balance and the difference between the measured proton angle and that predicted from the pion for the πp system.

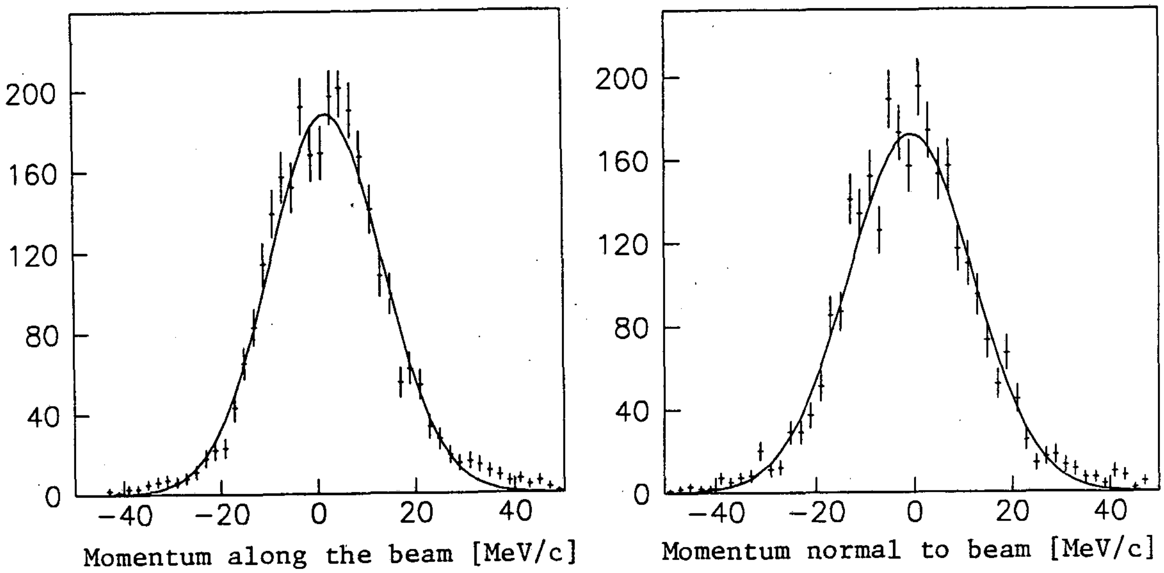

Figure 4.7: Measured momentum balances for the πp system.

source was dead, and we were unable to obtain two of our low energy calibration points, (the halflife of ^{88}Y is 106.6 days). Figure 4.8 shows a plot of the ADC spectra for the cesium source in several of the 64 crystals. Note that these are raw ADC spectra, and not energy plotted. The typical crystal resolution at 0.6616 MeV is 19.3%.

For intermediate energy photons, the energy deposited by cosmic muons has been studied by monte–carlo methods, and the entire spectrum is well understood (see Bay's Thesis as referenced in section 3.3). The midpoint of the rising edge of this spectrum is calculated to be at $28.7 \pm 0.3 MeV$. By measuring the spectra with a special trigger that requires the top and bottom anti–counters to fire in coincidence with a column of crystals we obtain a second calibration point. Figure 4.9 shows the measured cosmic spectra averaged over all of the 64 crystals. The tail below 200 channels in the ADC spectra is due to muons that go slightly diagonally through the array, only depositing a fraction of their energy in the top or bottom counter in a given column.

Finally for higher energy photons, the reaction

$$\pi^- p \rightarrow n\gamma$$

is examined by stopping π^-'s in the liquid hydrogen target. Since the 129MeV photons from this reaction are typically spread over several crystals, one can only use this as a check of the calibration from the lower energy photons. By examining only events whose

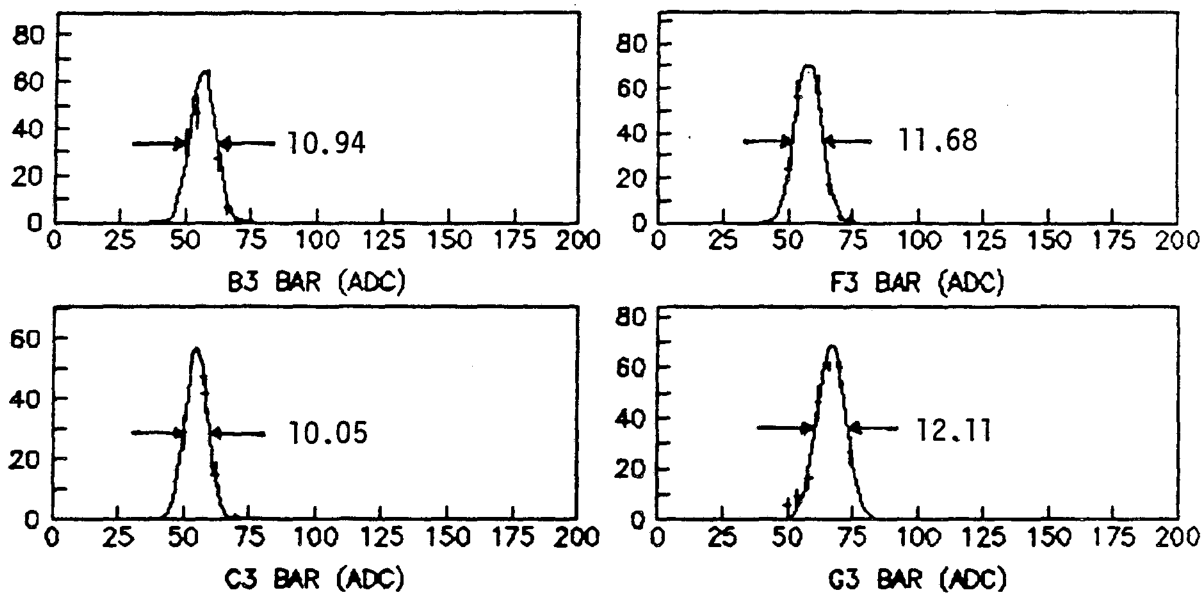

Figure 4.8: Cesium ADC Spectrum in several NaI crystal.

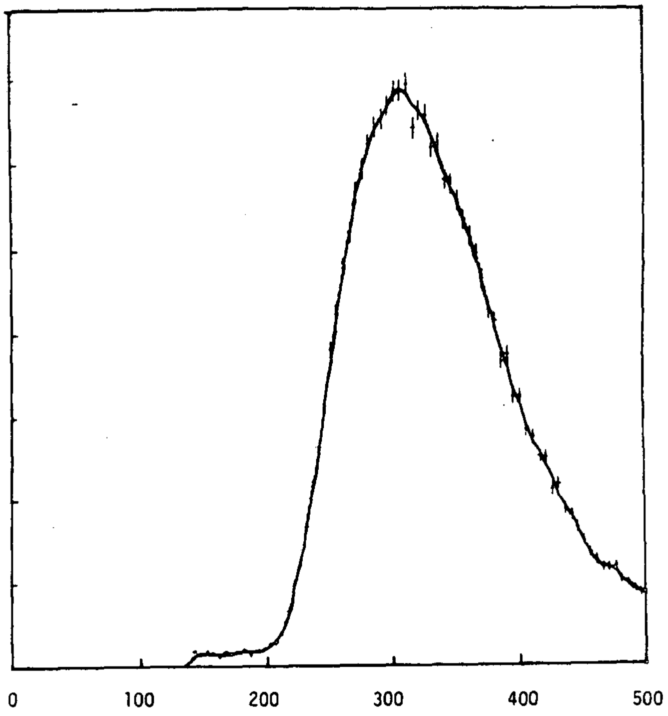

ADC channel number

Figure 4.9: Cosmic muon measured energy spectrum.

most energetic crystal is some fixed crystal one can do a rough check each of the individual calibrations and by repeating the process several times we iterate to a final set of calibration coefficients. Then by putting all of the π^- data together, the energy spectrum as shown in figure 4.10 is obtained. Monte–carlo calculations give that the center of the 129 MeV peak is at 125. MeV when the threshold for writing to tape is set at 0.4 MeV. This shift is caused by energy lost in the wrappings around crystals, energy leaking out of the detector and crystals with insufficient energy to be written out. From the higher peak, one obtains the resolution at 129 MeV to be about 9.5%. The large amount of background between the $\pi^-p \rightarrow \pi^0 n$ gammas and the $\pi^-p \rightarrow n\gamma$ gammas is due to electrons in the beam scattering off a collimator and into the NaI(Tl) array.

This resolution is poor when compared to the results in Bay's thesis (6% FWHM on the 129 MeV line), but the reasons are understood. We did not have the ^{8}8Y source, which caused us to lose two of our low energy calibration points. We also lost some of our Cs calibration data when the computer neglected to write any data to tape, (it is not clear what it wrote, but it certainly wasn't data). Also when Bay did his π^- runs, he detected a neutron in coincidence with the gamma. This eliminated almost all the background around the 129 MeV line. Finally, the NaI detector is several years older than it was during Bay's experiment, and yellowing may have occurred.

We can also obtain the time resolution of the NaI(Tl) detector by looking at the time spectra from the π^- data. Figure 4.11 is a plot of this time spectrum. The narrow sharp peak is gammas, while the broad later–time peak is from neutrons. One can also see a background under both these peaks which is the electron contamination. The width of the time peak for gammas gives us a time resolution of 1.78ns FWHM.

4.4.2 Reconstruction of Photons

Reconstruction of the photon begins with a search through all the fired crystals in the NaI(Tl) array to identify which one had the most energy deposited in it. Also during this search, all bars with less than 0.4MeV deposited in them were set to zero. This removes most of the noise coming from pedestal subtractions and activation of the crystals. This low energy cutoff was used in making all calculations on the NaI(Tl) array. Once the bar with the most energy in it was found, we checked to see it it was within allowed time of

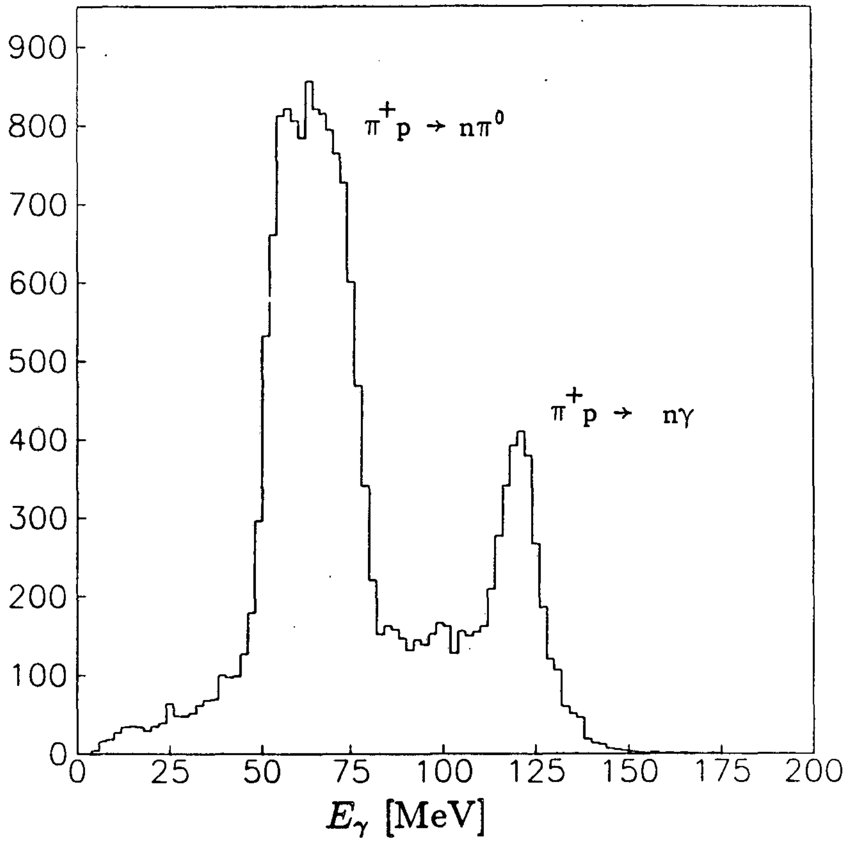

Figure 4.10: Energy spectrum from $\pi^-p \rightarrow n\gamma, n\ \pi^\circ$.

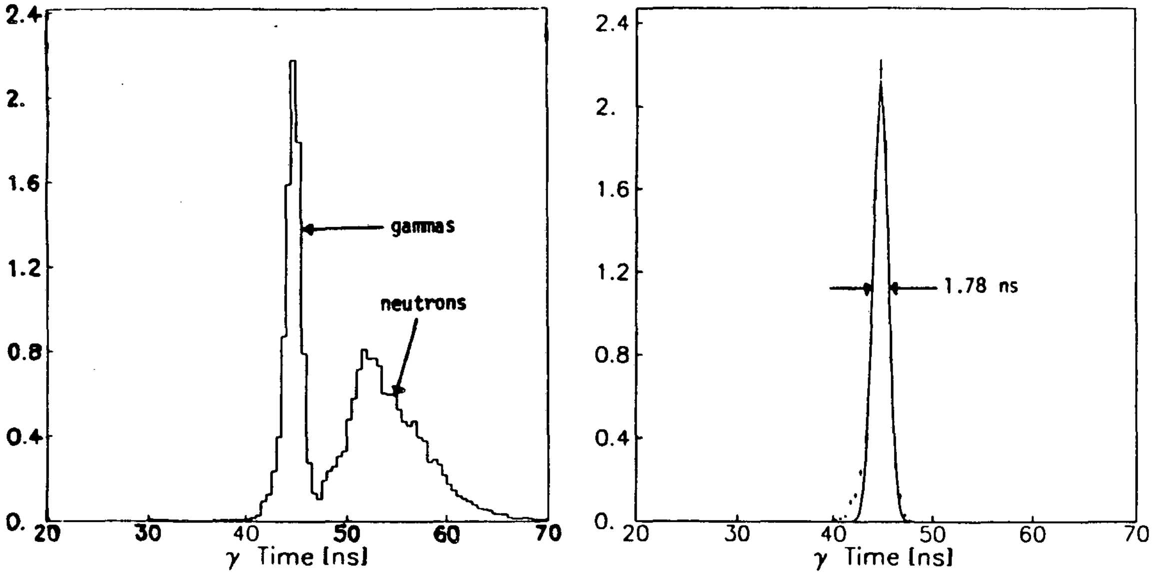

Figure 4.11: Time spectra of γ's from $\pi^-p \rightarrow n\gamma$.

flight windows and that it was not one of the 28 bars around the outside of the NaI(Tl) array.

If the above conditions were met, then we searched all of the 5 by 5 array of bars centered on the one with the most energy, and all those with any non-zero ADC readings were added into the total energy. There were no time of flight cuts placed on any of the secondary bars because if the energy deposited was small, then it was unlikely that we would have had a TDC reading from the bar. This then gave us the energy of the photon. Next we went back and examined all the secondary bars which had a time of flight within ±3ns of the bar with the most energy in it. From these we calculated a new time of the event by forming an energy averaged sum,

$$t_\gamma = \frac{\sum_{i=1}^{n} t_i \cdot E_i}{\sum_{i=1}^{n} E_i}.$$

This time is then checked to make sure that it comes within the allowed time of flight windows.

Finally, we calculate the position of the hit on the face of the NaI(Tl) array by forming an energy weighted sum of the center of each crystal which fired.

$$x_\gamma = \frac{\sum_{i=1}^{n} x_i \cdot E_i}{\sum_{i=1}^{n} E_i}$$

$$y_\gamma = \frac{\sum_{i=1}^{n} y_i \cdot E_i}{\sum_{i=1}^{n} E_i}$$

The angles of the photon are later calculated in the main program using the pion target traceback to the beam axis.

4.4.3 The Resolution and Efficiency of the NaI(Tl) Detector

The resolution of the NaI(Tl) array can be parameterized, following Bay, as

$$\sigma = \sigma_{129} - a \cdot (129 - E_\gamma).$$

From our $\pi^- p \rightarrow n\gamma$ measurement we obtain that $\sigma_{129} = 5.20$MeV. A resolution of between 16% and 21% is expected at 20MeV based on the resolution of 19% for the Cs data. From this we get a value of 0.033 for a. This can then be parameterized as:

$$R = \frac{229}{E_\gamma} + 8.02[\%FWHM]. \tag{4.5}$$

This formula is needed when we calculate the fraction of gammas lost when a low–energy cutoff is placed on the detector.

The efficiency of the NaI(Tl) array comes from two sources. First, there is a chance that the photon will veto itself in one of the anti–counters. Bay measured the contribution due to the FRONT anti–counter at 91.3% and the contribution from the anti–counters on the sides, top and bottom of the array to contribute 1%. The net efficiency from this was measured by Bay to be $92.3\% \pm 3\%$. This effect includes possible conversion of the photon in the air between the target and the detector, but does not include effects of conversion in the liquid hydrogen target. The second source was mentioned in the last paragraph and will be discussed in the next chapter.

Finally, we had no online monitor of the individual crystal gain stabilities in this experiment. A system exists for the NaI(Tl) array, but we did not make use of it. In order to verify that the overall stability was good, we looked at the reconstructed energy of all photons in several $\pi p \rightarrow \pi p \gamma$ runs. This energy spectra did not change between any of the examined runs; this does not guarantee the stability of any given crystal, only that the overall stability is good.

Chapter 5

Data Reduction and Analysis

5.1 Calculated Corrections to the Data

There are several corrections to the data that need to be calculated in order to extract the correct cross–section. Some of these can be checked against the data to make sure that they agree, whereas others one needs to accept as such. These effects are discussed in the following sections, and comparisons to an experimental check are made when possible.

5.1.1 Pion Decay

When pions decay in flight while traversing the pion spectrometer, the pion can either be lost to the system or be reconstructed with the wrong momentum. Looking at the elastic data, we observe that if the pion is reconstructed with a momentum more than 30MeV/c away from its true momentum it will be lost to the system, whereas if it is closer than 30MeV/c away from its true momentum, it will probably be accepted. In order to study this problem, we used the monte–carlo to track pions through the system, and allowed the pions to decay in flight based on the 26.03 ns lifetime of the pion. The muons resulting from this decay were thrown uniformly in the pion rest frame, and then boosted into the lab frame. The program then tracked the muon through the rest of the spectrometer. By comparing the number of accepted events when pions were allowed to decay and when pions were not allowed to decay we were able to calculate a pion decay correction. The results of this calculation are shown in table 5.1.

If we assume that all pions that decay before they reach the center of the spectrometer

p_π	Accepted (no decay)	Accepted (decay)	Accepted Fraction
160.0	978	835	0.854 ± 0.040
200.0	6496	5889	0.907 ± 0.016
	1299	1138	0.876 ± 0.028
	1299	1072	0.825 ± 0.025
avg.			0.875 ± 0.023
250.0	1246	1136	0.912 ± 0.037
300.0	5472	4915	0.898 ± 0.018
	1094	1003	0.917 ± 0.032
avg.			0.905 ± 0.023
350.0	1004	924	0.920 ± 0.042

Table 5.1: Results of the monte–carlo decay calculation.

magnet are lost, and all those that decay after the center of the spectrometer magnet are accepted, then the fraction of pions that decay and are lost is

$$f = e^{-\frac{m_\pi \cdot l}{p_\pi \cdot \tau_\pi \cdot c}}.$$

Where $c = 30\text{cm/ns}$, $l = 150.\text{cm}$, $\tau_\pi = 26.03\text{ns}$ and $m_\pi = 139.57 MeV/c^2$. A comparison of this model with the above monte–carlo calculation is shown in figure 5.1. The agreement is remarkably good, and thus this formula was used for all decay corrections.

We also looked at decay as a function of E_γ by throwing $\pi p \rightarrow \pi p \gamma$ events with the pion allowed to decay. The results from this study were consistent with the previous result, but since pion decay is a function of pion momentum, and not directly of photon energy, we did not use these results in correcting the final date.

5.1.2 The Efficiency of the Proton Detector

There are several sources of inefficiency in the proton detector. It is possible for a proton to be absorbed or to scatter on its way to the the proton detector. There are essentially three sources for this, the liquid hydrogen target, air, and the hodoscope array. Table 5.2 lists the

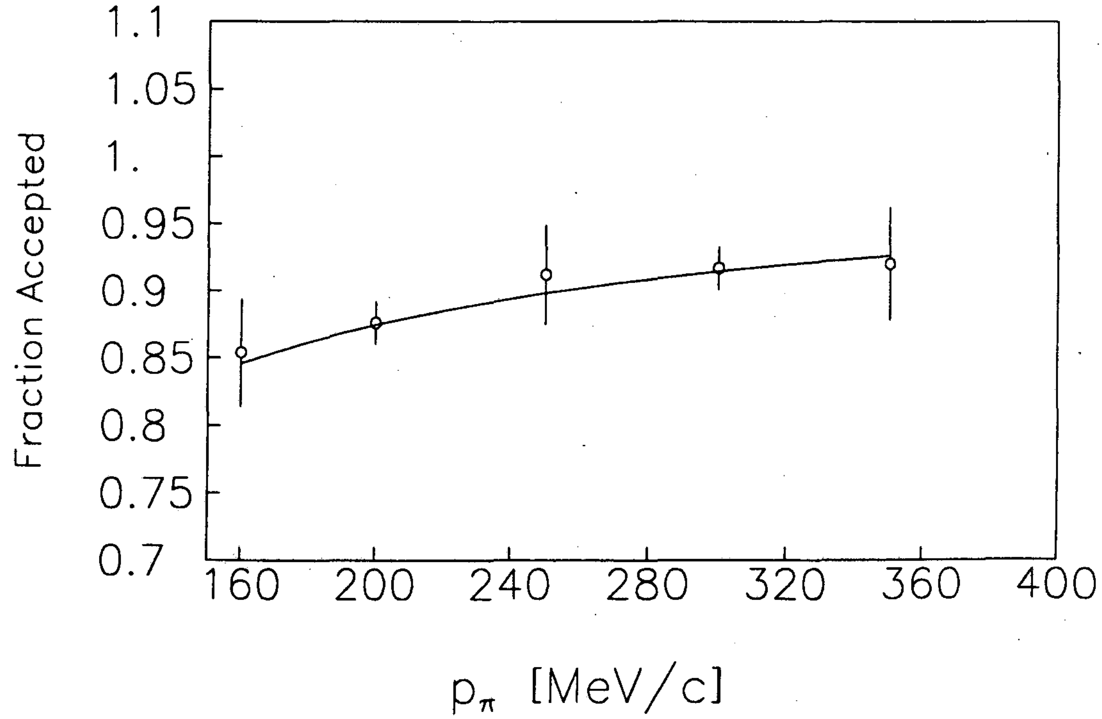

Figure 5.1: Results of pion decay monte–carlo compared to the model.

fraction of protons lost from each of these sources as given by tables in the literature[47,48]. Also, once the proton enters the proton detector, it is possible that it will interact with a

Energy at Target	H $.245\frac{gm}{cm^2}$	O $.052\frac{gm}{cm^2}$	Hodoscope $.515\frac{gm}{cm^2}$	Total
50 MeV	0.7%	1.3%	0.9%	2.9%
75 MeV	0.6%	1.1%	0.8%	2.5%
100 MeV	0.4%	1.0%	0.6%	2.1%
125 MeV	0.4%	0.9%	0.6%	1.9%
150 MeV	0.3%	0.8%	0.6%	1.7%

Table 5.2: Percentage of protons absorbed before reaching the proton detector.

nucleus and a substantial amount of its energy will be released as neutrons. These neutrons will not be detected and the energy will be lost. The fraction of such events as a function of proton energy at the target is shown in table 5.3. In order to check this calculation,

---

[47] J. Bystricki and F. Lehar, Physik-Daten 11, 1 (1978).

[48] J.F. Janni Proton Range-Energy Tables Atomic Data and Nuclear Data Tables 27, 147 (1982).

Energy at Target	Energy at Proton Detector	% lost in proton Detector	Total Lost [%]
50 MeV	34.9 MeV	2.3	5.2
75 MeV	64.1 MeV	5.9	8.4
100 MeV	91.2 MeV	9.8	11.9
125 MeV	117.4 MeV	13.8	15.7
150 MeV	143.5 MeV	17.8	19.5

Table 5.3: The percentage of protons lost due to energy being released as neutrals in the proton detector.

we had made some elastic runs in which the proton detector was not in the trigger. By reconstructing the pion side of the spectrometer and requiring the pion momentum to be close to the elastic momentum at the measured pion angle, we can select a sample of πp elastic events. If we then reconstruct the proton arm of the spectrometer for only those elastic events, we are able to measure the efficiency of the proton detector. The results from this analysis are that proton E_2 is $85.7 \pm 3.5\%$ efficient and proton E_3 is $89.1 \pm 2.6\%$ efficient. (We do not observe elastic events in the E_1 counter.) From the above calculations we obtain that for elastic events, proton E_2 should be 84.8% efficient and proton E_3 should be 90.3% efficient. There is remarkably good agreement between these two sets of numbers.

Corrections for the real data are made by parameterizing the above tables as a function of E_p. Corrections are then made event by event based on the proton energy in the event.

5.1.3 The Response of the NaI(Tl)

According to Bay[49] the response of the NaI(Tl) array to a monoenergetic beam of gammas can be expressed as the convolution of a delta function, a gaussian and a function which is an exponential on the low energy side of the delta function and zero on the high energy side. The gaussian has a sigma given by equation 4.5, while the exponential can be expressed as $e^{-\kappa|E-E_\delta|^\tau}$ if $E < E_\delta$ and as 0 otherwise. Where $\tau = 0.7$, $\kappa = 0.76 - 3.02 \cdot 10^{-3}E$ and $E_\delta = E/1.03$. A plot of these convolutions for various values of E are shown in figure 5.2. It

---

[49] A. Bay Ph.D. Thesis, see section 3.1.

is important to understand these functions in order to correctly parameterize the efficiency of the NaI(Tl) array. In the experiment there was a hardware cutoff at $E_\gamma = 14 MeV$. Because of this a certain fraction of the events will be lost for gammas near 20 MeV. In order to make sure that we understand this effect the data was analyzed with a software cut on E_γ at 15MeV and at 20MeV. According to this analysis, there should be a 3.7% correction in the photon bin between 20 and 30 MeV for the 15MeV cut, and a 21.4% correction in this same bin with the 20MeV cut. These corrections are plotted in figure 5.3. These numbers agree very well with what one finds when the analyses are carried out on the data.

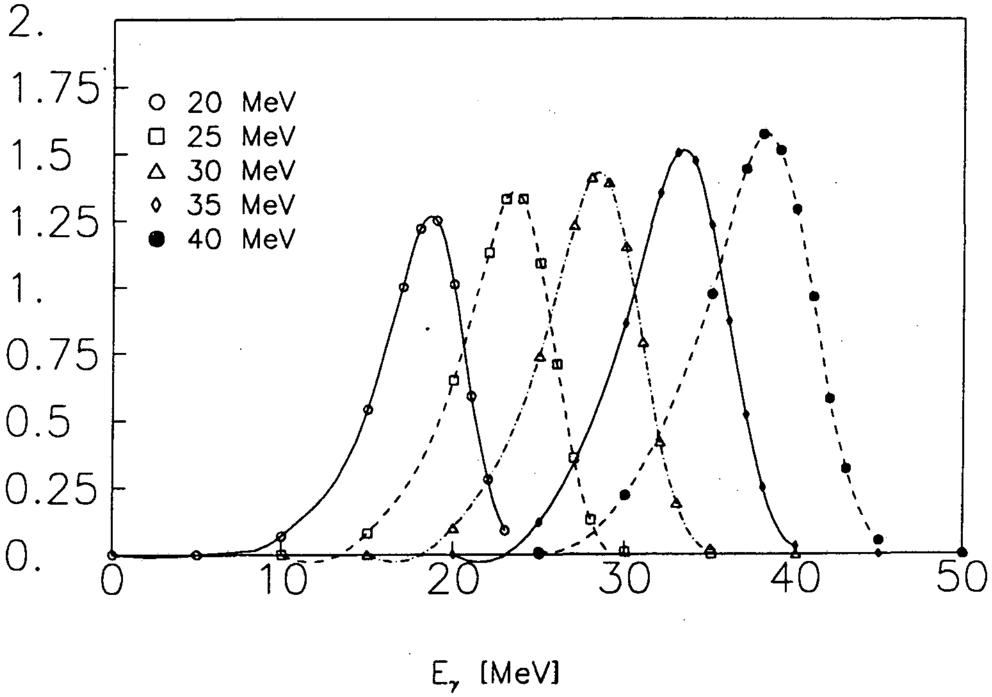

Figure 5.2: The response of the NaI(Tl) array to various energy photons.

There is also a correction to the monte–carlo solid angles for the NaI(Tl) array as calculated in chapter 3. In calculating that solid angle with the monte–carlo, we required that the position of the photon at a depth of 3cm into the crystal be inside the central 6 by 6 array of crystals. However, events which are near the outer edge of the 6 by 6 array at that point will probably deposit most of their energy in one of the 28 guard crystals and be lost to the system. The closest distance depends upon the energy of the photon and is calculated to be an effect ranging from about 6% for 20MeV photons to about 12% for

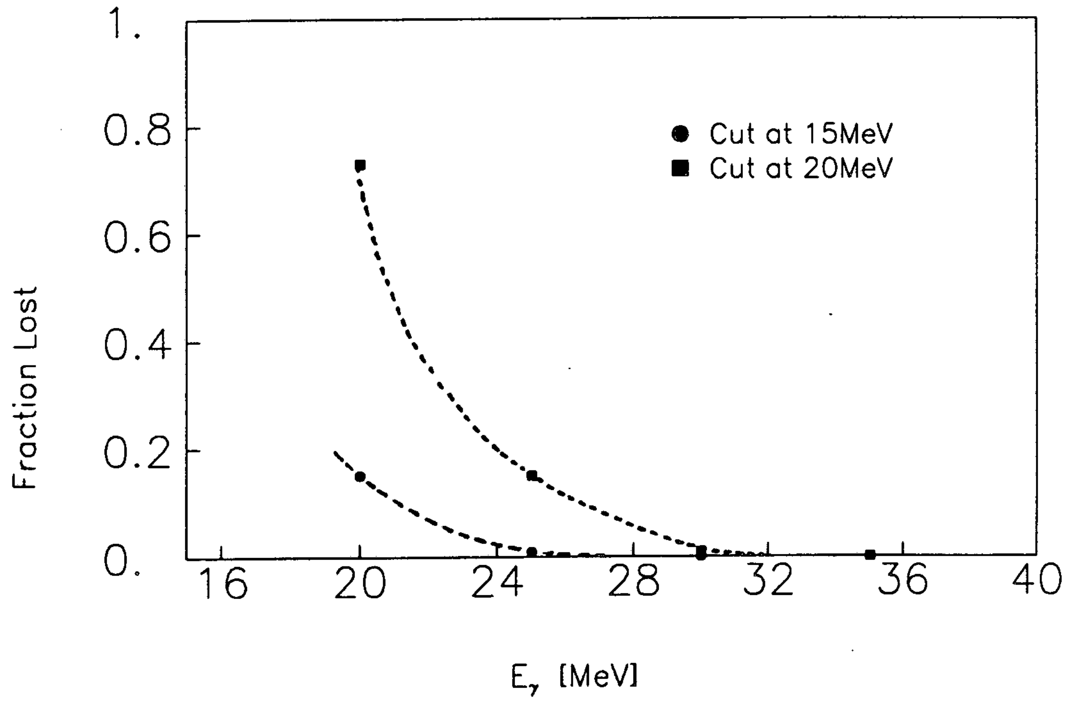

Figure 5.3: The efficiency of the NaI(Tl) array as a function of incident photon energy for two energy thresholds.

100MeV photons.

5.2 Analysis of Elastic Data

During our run, we took one tape of $\pi p \rightarrow \pi p$ triggers, (30 minutes) for every five tapes of $\pi p \rightarrow \pi p \gamma$ triggers, (10 hours). The elastic data was taken for two reasons. It allowed us to calibrate our proton detector, and gave us a well known cross-section to measure and possibly use for absolute normalization. The calibration is described in chapter 4, here we will only discuss measurement of the elastic cross-section.

The first thing that is done with the raw data is to make sure that there is really a pion and a proton in the correct detectors. This can be done by looking at pulse-height and time of flights in the two detector arms, and saves us from doing a full track reconstruction on garbage events, (the track reconstruction is the most CPU expensive part of the analysis code). This cut is made by forming the sum:

$$\chi^2 = \left[\frac{(E_1E_2)_\pi - a_1}{c_1}\right]^2 + \left[\frac{t_\pi - a_2}{c_2}\right]^2 + \left[\frac{AB_\pi - a_3}{c_3}\right]^2 + \left[\frac{H_p - a_4}{c_4}\right]^2 + \left[\frac{t_p - a_5}{c_5}\right]^2 \qquad (5.1)$$

Where $(E_1E_2)_\pi$ is the ADC reading in the pion E–array, t_π is the pion time of flight, AB_π is the ADC reading in the pion B–array, t_p is the proton time of flight and H_p is the average ADC reading of both ends of the proton hodoscope which fired. All events that passed the above cut were then analyzed completely, with the analysis code reconstructing $(p_\pi, \phi_\pi, \theta_\pi)$ and (E_p, α_p); α_p is the in plane angle of the proton as defined in equation 2.1. We did not use the time difference information in the hodoscope to reconstruct β_p because of a time walk problem in some of the CFD's, also the vertical acceptance of the pion spectrometer constraints the proton to be close to in plane. The interaction point in the target is obtained from the pion reconstruction with the assumption that the event came from on the beam axis. Corrections are made to the energy and momentum of the initial pion, and the final pion and proton based on target penetration, and then ϕ_p and θ_p are calculated to best balance the event's momentum.

In order to identify which events come from elastic events, we perform several cuts on reconstructed quantities. First of all we reconstruct the mass of the target from the kinematic information.

$$m_t = \sqrt{(E_\pi^{in} - E_\pi - E_p)^2 - \mid \vec{p}_\pi^{\,in} - \vec{p}_\pi - \vec{p}_p \mid^2} \tag{5.2}$$

If we take the difference between m_t and m_{proton}, we should get a peak which is centered at 0MeV for real events. Figure 5.4 shows this quantity plotted for all reconstructed events in an elastic data sample. The long tail to the left arises from pions decaying, protons rescattering, protons losing energy via neutrals and events coming from the mylar walls of the target vessel, while the tail to the right is from pions decaying. Figure 5.5 is a plot of the same quantity from an empty target run. We cut in this quantity at ±35MeV, which is at the 4.4σ level with the assumption that the true peak is gaussian.

Next we examine the overall momentum balance of the system,

$$P_{Bal} = \mid \vec{p}_{in} - \vec{p}_\pi - \vec{p}_p \mid \tag{5.3}$$

which is just the resulting magnitude of the unbalanced three–momentum. This quantity is plotted in figure 5.6, while the same quantity for an empty target run is plotted in figure 5.7. The reason that this quantity is not peaked at zero is due to the poor overall momentum resolution of the system, see figure 4.6. We cut in this spectra at 60MeV, however the effect is essentially null when the previous and next cuts are performed first.

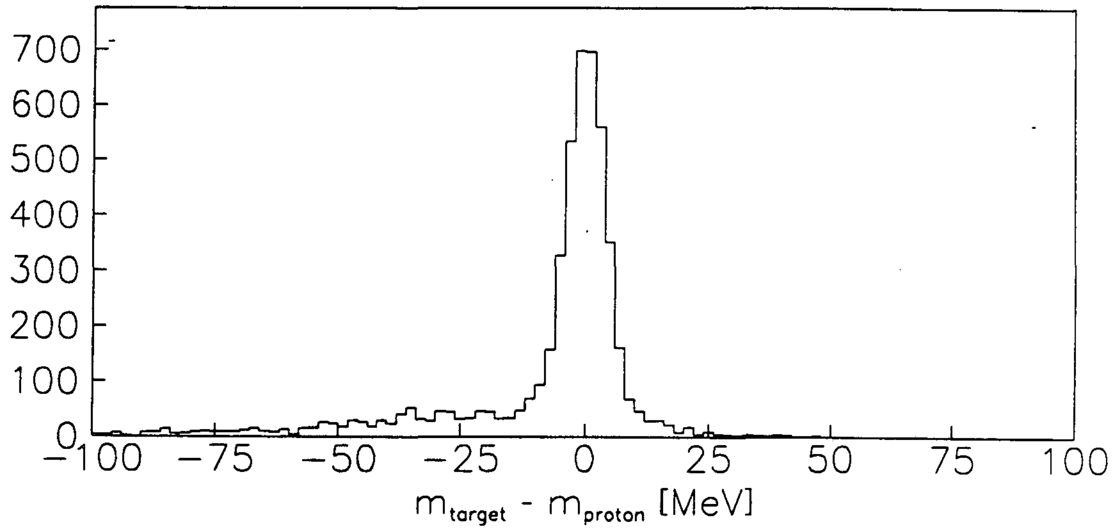

Figure 5.4: A plot of $m_t - m_p$ for an πp → πp data sample.

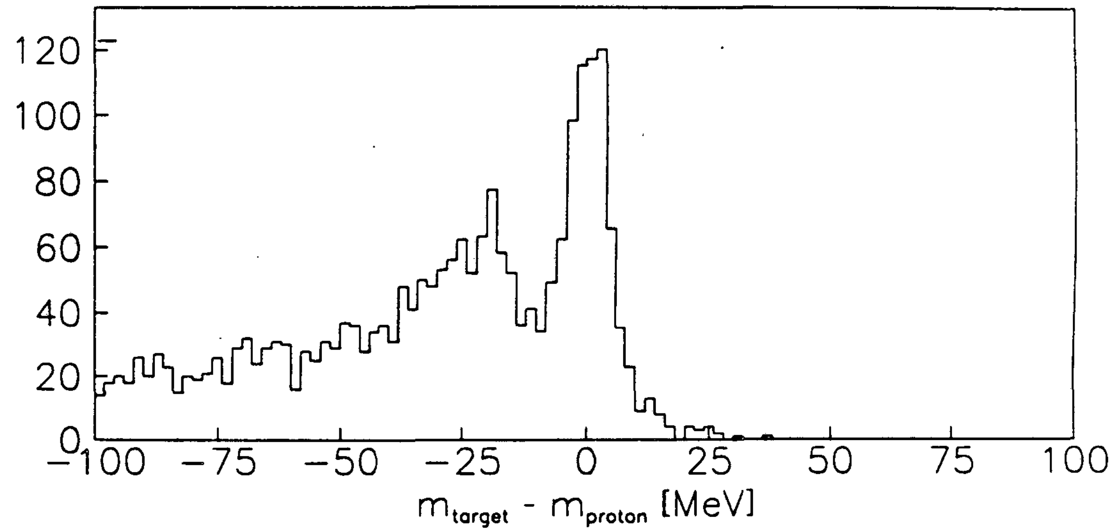

Figure 5.5: A plot of $m_t - m_p$ for an empty target πp → πp data sample.

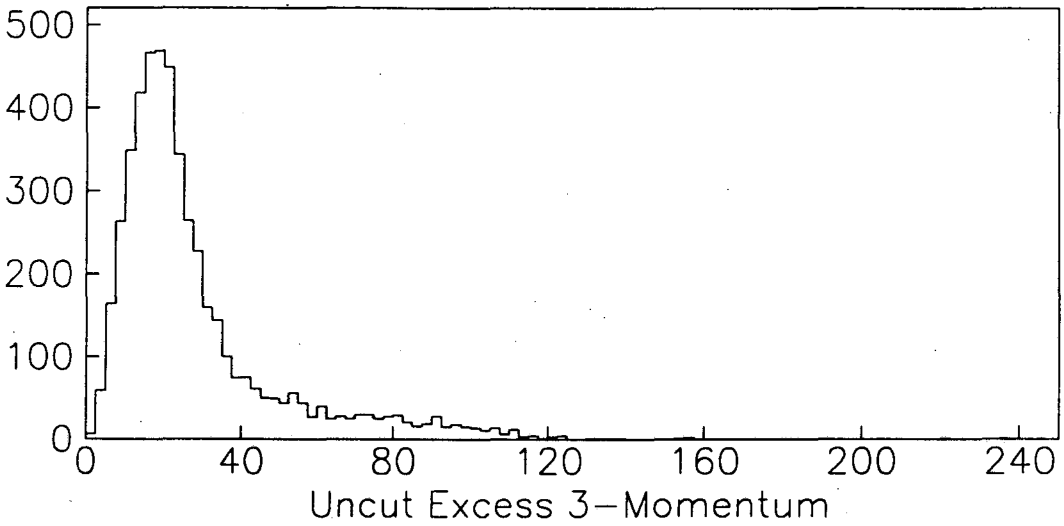

Figure 5.6: A plot of the momentum balance for a $\pi p \rightarrow \pi p$ data sample.

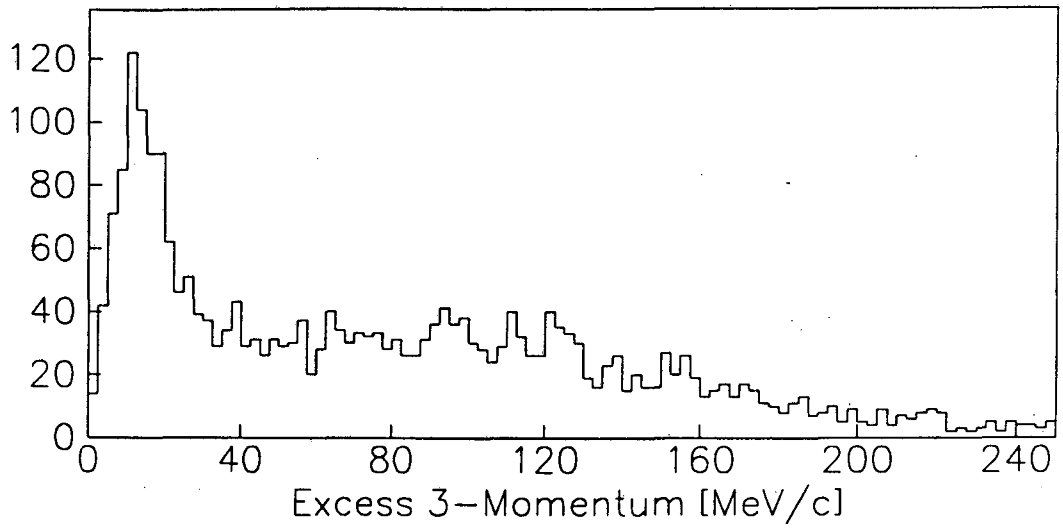

Figure 5.7: A plot of the momentum balance for an empty target $\pi p \rightarrow \pi p$ data sample.

Finally, we use the angular information from the reconstruction to form the quantity,

$$\Delta\alpha_p = \alpha_p^{meas} - \tan^{-1}\left[\frac{-p_\pi^x}{p_{in} - p_\pi^z}\right] \tag{5.4}$$

the difference between the measured α_p and that as calculated from the pion. This quantity is plotted in figure 5.8 and a cut is placed at ±6°, which is at 3.7σ. Plots of the three quantities after the cuts have been made are presented in figure 5.9. When the empty target data is passed through the same cuts, we find that the contribution to the signal is less than 1.7% of the true signal. This turns out to be so small as compared to the errors on the data, that no subtraction was made.

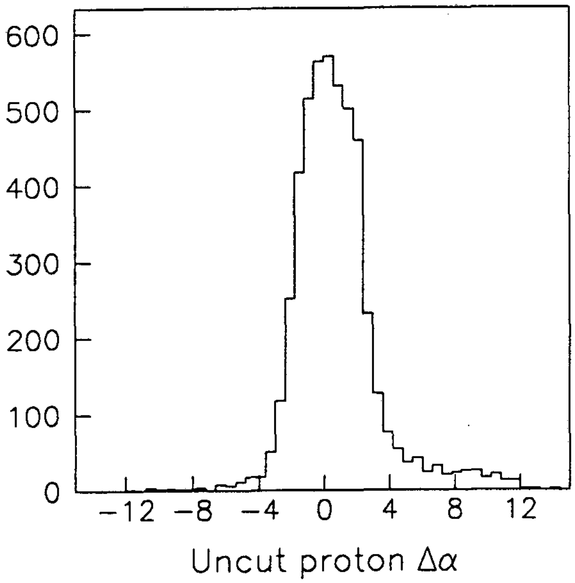

Figure 5.8: The $\Delta\alpha$ quantity for an πp → πp data sample.

The data set that survives all these cuts is then used to calculate the elastic cross–section. The cross–section is given by the following formula.

$$\frac{d\sigma}{d\Omega} = \frac{N_{scat}}{N_{in}} \cdot \frac{1}{N_{proton} \cdot f_t} \cdot \frac{1}{\Omega_\pi} \cdot \frac{1}{\epsilon_{ch}} \cdot \frac{1}{\epsilon_\pi} \cdot \frac{1}{\epsilon_p} \cdot \frac{1}{\eta_{decay}} \cdot \frac{1}{\eta_{pu}} \tag{5.5}$$

- N_{scat} is the number of scattered pions.
- N_{in} is the number of incident pions. For the run analyzed, $N_{in} = (202 \pm 6) \cdot 10^6$.
- N_{proton} is the number of protons in the liquid hydrogen target. The density of the target is $\rho_H = 0.0727 gm/cm^3$, and the thickness of the target is t = 14cm. This gives

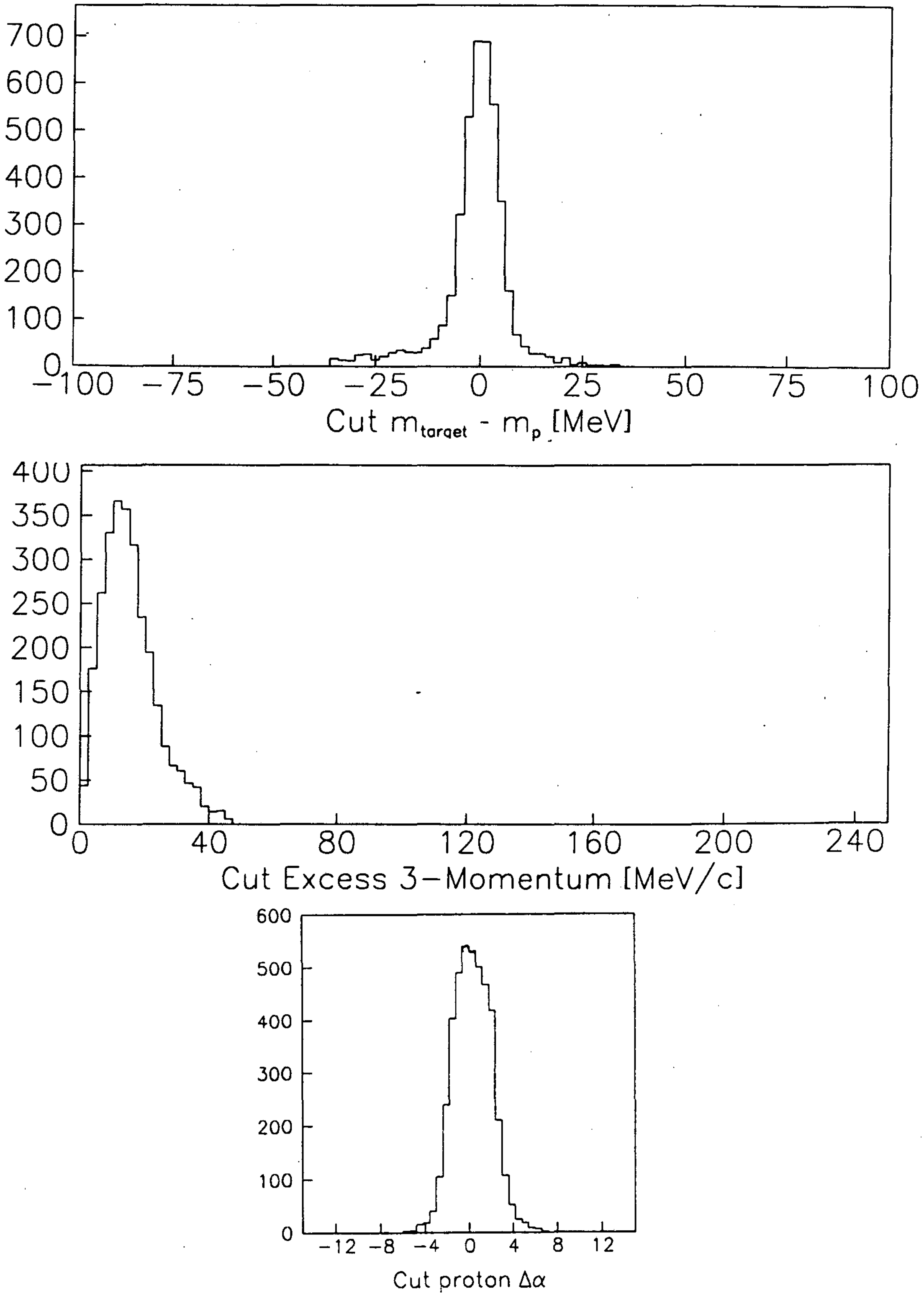

Figure 5.9: The resulting three quantities after cuts.

that:

$$\begin{aligned} N_{proton} &= \rho \cdot t \cdot N_A \cdot (10^{-27}[cm^2/mb]) \\ &= 613. \cdot 10^{-6}/mb. \end{aligned}$$

- f_t is the fraction of the liquid hydrogen target seen at each angle.
- Ω_π is the solid angle of the pion spectrometer over the accepted angular range, this has been calculated by monte–carlo for each of the bins in θ_π.
- ϵ_{ch} is the total chamber efficiency during the elastic run, for this run

  $$\epsilon_{ch} = 0.431 \pm 0.007.$$
- ϵ_π is the pion reconstruction probability ignoring the chamber efficiency. This includes the efficiency of the E and AB arrays, as well as the track finder efficiency. This effect is $\epsilon_\pi = 0.875 \pm 0.021$.
- ϵ_p is the efficiency of the proton detector. This efficiency is $85.7 \pm 3.5\%$ in proton E_2 and $89.1 \pm 2.6\%$ in proton E_3.
- η_{pu} is a correction for pile–up in the proton counters. For proton E_2 this number is 0.930 ± 0.017 and for proton E_3 0.954 ± 0.020.
- η_{decay} is the correction for decayed pions that are lost to the system, this has been calculated in section 5.5.1 .

The results of this measurement are presented in table 5.4, while a plot of the resulting quantity is presented in figure 5.10. The cross–section is compared to the Karlsruhe–Helsinki phase shift results. Our average energy at the center of the target is 415.8 MeV/c. The agreement is quite good, and gives us confidence that we understand the pion and proton arms of our detector.

5.3 Monitoring Detector Stability

There are many quantities that need to be monitored throughout the experiment in order to make a good measurement. The number of incident pions needs to be measured, but

p_π $[MeV/c]$	θ_π [degrees]	Ω_π [msr]	η_{decay} [%]	$\frac{d\sigma}{d\Omega}$ K–H [mb/sr]	$\frac{d\sigma}{d\Omega}$ meas [mb/sr]
336.0	60	6.78 ± 0.14	0.923 ± 0.023	4.49	4.54 ± 0.31
332.0	62	6.92 ± 0.14	0.922 ± 0.023	4.00	4.04 ± 0.23
328.0	64	7.04 ± 0.14	0.922 ± 0.023	3.56	3.65 ± 0.21
324.1	66	7.16 ± 0.14	0.921 ± 0.023	3.18	3.57 ± 0.20
320.2	68	7.26 ± 0.15	0.920 ± 0.023	2.84	2.76 ± 0.17
316.3	70	7.36 ± 0.15	0.919 ± 0.023	2.67	2.46 ± 0.16
312.5	72	7.45 ± 0.15	0.918 ± 0.023	2.31	2.44 ± 0.15
308.7	74	7.53 ± 0.15	0.917 ± 0.023	2.11	2.03 ± 0.15
304.9	76	7.60 ± 0.15	0.916 ± 0.023	1.94	2.07 ± 0.15
301.2	78	7.66 ± 0.15	0.915 ± 0.023	1.80	1.83 ± 0.13
297.6	80	7.71 ± 0.15	0.914 ± 0.023	1.70	1.73 ± 0.13
294.0	82	7.76 ± 0.16	0.913 ± 0.023	1.62	1.43 ± 0.11
290.4	84	7.79 ± 0.16	0.912 ± 0.023	1.57	1.60 ± 0.12
287.0	86	7.81 ± 0.16	0.911 ± 0.023	1.53	1.55 ± 0.12
283.6	88	7.83 ± 0.16	0.910 ± 0.023	1.51	1.53 ± 0.12
280.2	90	7.83 ± 0.16	0.909 ± 0.023	1.52	1.53 ± 0.13
χ^2 per degree of freedom				10.99/16	

Table 5.4: Measured elastic cross–sections at $p_\pi = 415.8\text{MeV/c}$.

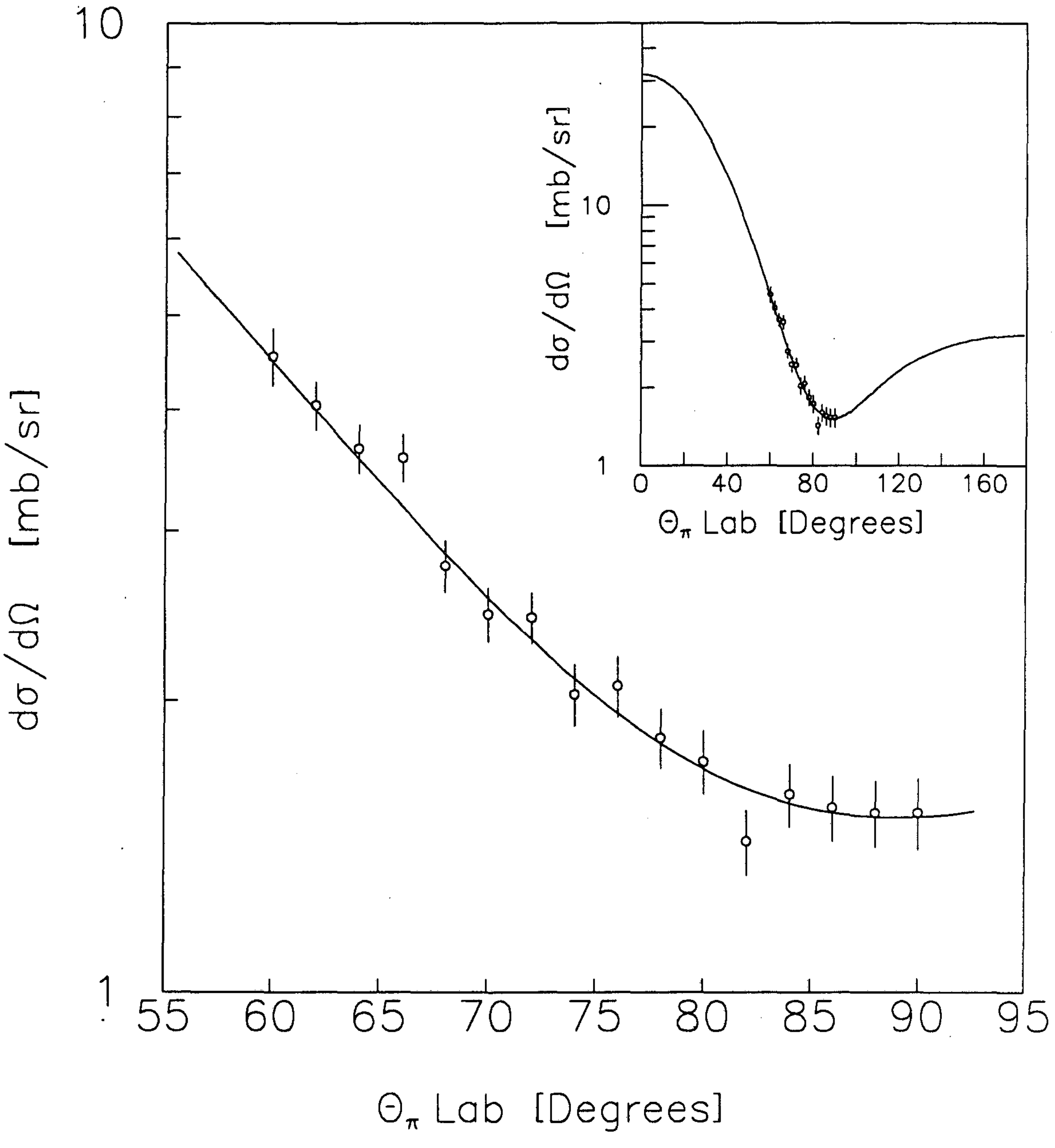

Figure 5.10: The measured elastic cross-section versus phase-shift calculations at $p_\pi = 415.8\text{MeV/c}$.

unfortunately with over 25MHz of incident beam on the target, this cannot be done by simply shoving a counter in the beam and letting things go. The density of the liquid hydrogen target needs to be watched. The control system we used let us monitor the pressure above the target, but no direct temperature probe was in the target, and we had no way of observing visually if the target was boiling. Finally, there are gains in all of the counters and efficiencies of the chambers that need to be watched. These gains and efficiencies were discussed in chapter 3, and the discussion will not be repeated here.

5.3.1 The Incident Pion Flux

The incident pion flux was monitored by means of a scintillator telescope that looked at the entrance window to the vacuum vessel around the liquid hydrogen target. This counter was referred to as the JOKER counter for some historical reason unknown to me. The JOKER counter consisted of two $1cm^2$ plastic scintillators about 50cm apart; the front one being about 1m from the target. They were mounted on top of the NaI(Tl) array and looked down at the target.

Calibration of the JOKER counters was done by lowering the beam flux from the 26MHz used in the experiment down to between 500KHz and 2MHz and putting a counter in the incident beam, Π_1. We were then able to count the number of incident pions and compare this number directly to that obtained in the JOKER counter. This analysis gives us a conversion factor from JOKER to N_{in} such that

$$N_{in} = (1.90 \pm 0.06) \cdot 10^6 \cdot JOKER.$$

5.3.2 The Target Density

As was mentioned in section 4.2, we had one measurement of the target density which was made by observing the energy loss of protons passing through the target. This measurement agreed well with published densities, and as such I nominally used the average liquid density over all temperatures at which hydrogen is a liquid. In order to make sure that this was not varying from run to run, we measured the elastic cross–section during each $\pi p \rightarrow \pi p \gamma$ run and fit the results to the known cross–sections with the target density as a free parameter.

As was stated in section 5.2, photons that were off the accepted time by 20ns provided a good random sample trigger throughout the experiment. In analyzing background elastics we examined a photon time window around photons which were from a later beam burst, and were uncorrelated with the pion and proton. The πp events in this peak should be mostly elastics. If we then treat the number of incident pions as

$$N_{in} = \frac{N_\gamma \cdot 20ns}{Time} \cdot JOKER \cdot 1.90 \cdot 10^6,$$

then we have a good measure of the elastic cross-section. Figure 5.11 shows the elastic cross-section after being fit to the K–H phase shifts, while figure 5.12 shows a plot of the target density measured in this manner plotted against time in hours. The two lines in figure 5.12 are the *best fit to a constant density* and the *best fit to a straight line whose slope is free.* The very first point is low as during that run the proton E_3 counter was turned off, and it was not included in either of the fits. We feel there is no justification for choosing the slanted line, in particular because most of the low points were from low statistics runs. The density that we obtain from this analysis is

$$\rho_{H_2} = (1.007 \pm 0.048) \cdot 0.0727 \frac{gm}{cm^3}.$$

A similar analysis performed on an elastic run gives that

$$\rho_{H_2} = (1.001 \pm 0.043) \cdot 0.0727 \frac{gm}{cm^3}.$$

This measurement is coupled to the calibration of the incident flux, and the fact that the measured density is constant implies that we have a stable monitor of the incident pion flux.

5.4 Analysis of Bremsstrahlung Data

In reconstructing the bremsstrahlung data, we first make sure that we have a π and a p in the correct detectors in exactly the same manner as for the elastics, (equation 5.1). However, unlike the $\pi \mathrm{p} \rightarrow \pi \mathrm{p}$ data, the $\pi \mathrm{p} \rightarrow \pi \mathrm{p} \gamma$ data written to tape has a large fraction of events where a proton triggered the pion spectrometer. Application of this cut to all the data on tape removes about 60% of the triggers, (in the $\pi \mathrm{p} \rightarrow \pi \mathrm{p}$ data, this cut removed about 25% of the triggers). The events that survive these cuts are then reconstructed; we obtain $(p_\pi, \phi_\pi, \theta_\pi)$, (E_p, α_p) and $(E_\gamma, \phi_\gamma, \theta_\gamma)$. When we reconstruct the photon, we apply a time of flight cut such that we only accept events which are in a 6.1ns wide window about

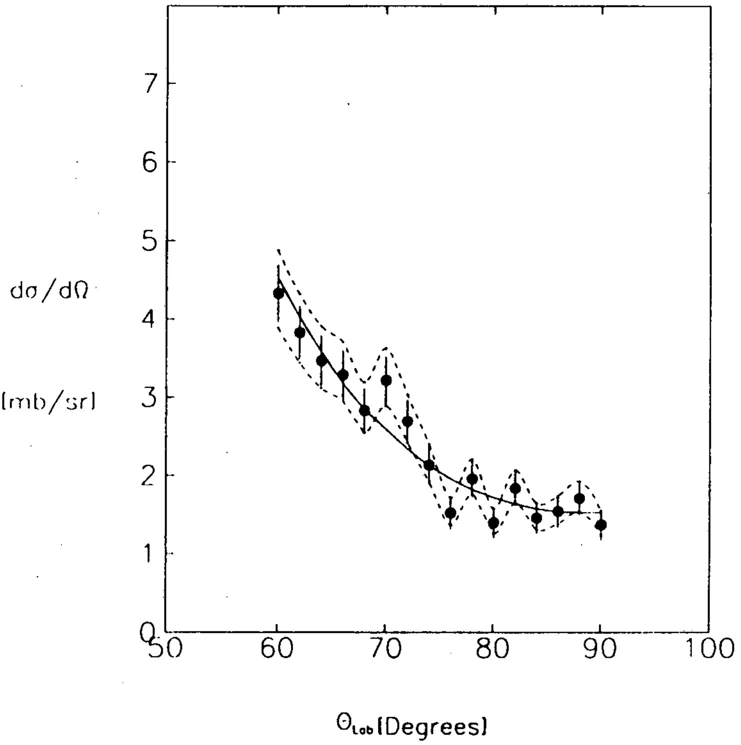

Figure 5.11: The elastic cross-section as measured with random photons.

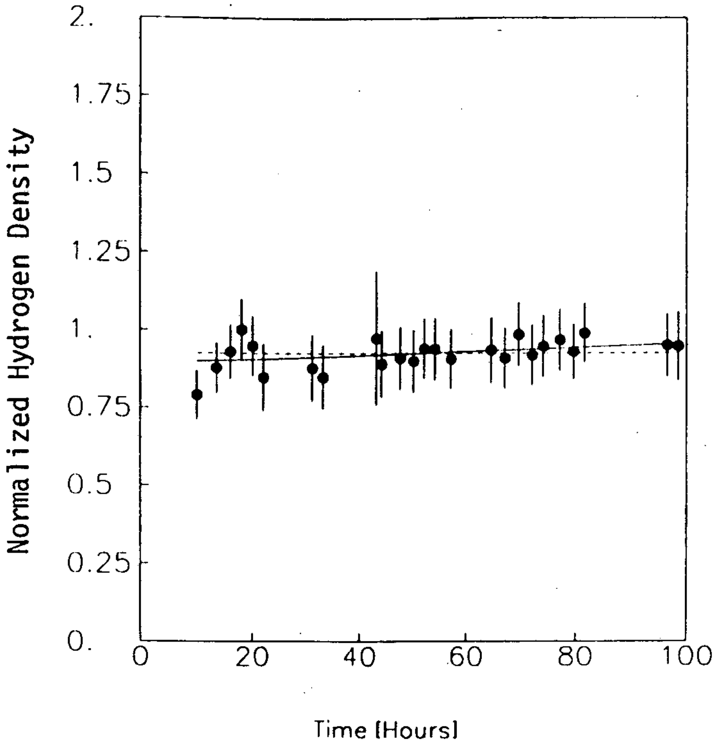

Figure 5.12: The density of the liquid hydrogen target as a function of time.

the central photon time. Recall from 4.4.1 that the time resolution of the NaI(Tl) array was 1.78ns FWHM; our cut on the photon time is at the $\pm 4\sigma$ level. We also only accept events which are centered in the central 6 by 6 array of crystals. At this level, we still have about 2.3% of all the events which were written to tape. We will refer to this sample in which we have a reconstructed π, p and γ as the *raw* data set.

Next we can form the same sort of kinematic quantities that we used for the elastics. The definitions are slightly changed from those in equations 5.2, 5.3 and 5.4 to include the photon, and we include a total energy balance, E_{Bal}.

$$\begin{aligned}
m_t &= \sqrt{(E_{in} - E_\pi - E_p - E_\gamma)^2 - \mid \vec{p}_\pi^{\,in} - \vec{p}_\pi - \vec{p}_p - \vec{p}_\gamma \mid^2} && (5.6) \\
P_{Bal} &= \mid \vec{p}_{in} - \vec{p}_\pi - \vec{p}_p - \vec{p}_\gamma \mid && (5.7) \\
\Delta\alpha_p &= \alpha_p^{meas} - \tan^{-} \left[\frac{-p_\pi^x - p_\gamma^x}{p_{in} - p_\pi^z - p_\gamma^z} \right] && (5.8) \\
E_{Bal} &= E_{in} + m_p - E_\pi - E_p - E_\gamma && (5.9)
\end{aligned}$$

These four quantities for the raw data set are shown in figure 5.13. From these figures we see some hint of the bremsstrahlung signal as the small enhancement around 0MeV in the $m_t - m_p$ and E_{Bal} plots. However there is no obvious place to start cutting.

At this point we note that most of the surviving events must be an elastic event in coincidence with a random photon. Since the detector with the best resolution is the pion spectrometer, we want to examine the quantity $p_\pi^{meas} - p_\pi^{elas(\theta)}$ for the data sample. By looking at the kinematics of a πp $\rightarrow$ πpγ event in our detector, we find that the above quantity can be parameterized as

$$p_\pi^{meas} - p_\pi^{elas(\theta)} \approx -0.86 \cdot E_\gamma[MeV].$$

By including the momentum resolution of the pion spectrometer, and looking at the tails in the $p_\pi^{meas} - p_\pi^{elas(\theta)}$ for elastic events we find in cutting

$$p_\pi^{meas} - p_\pi^{elas(\theta)} < -9.0MeV/c$$

that we lose less than 4% of all good events at any given photon energy. Table 5.5 shows the calculated fraction lost at each photon energy. In figure 5.14 is plotted this quantity for the raw data set. In this figure we have identified the three major constituents of the sample and have indicated them.

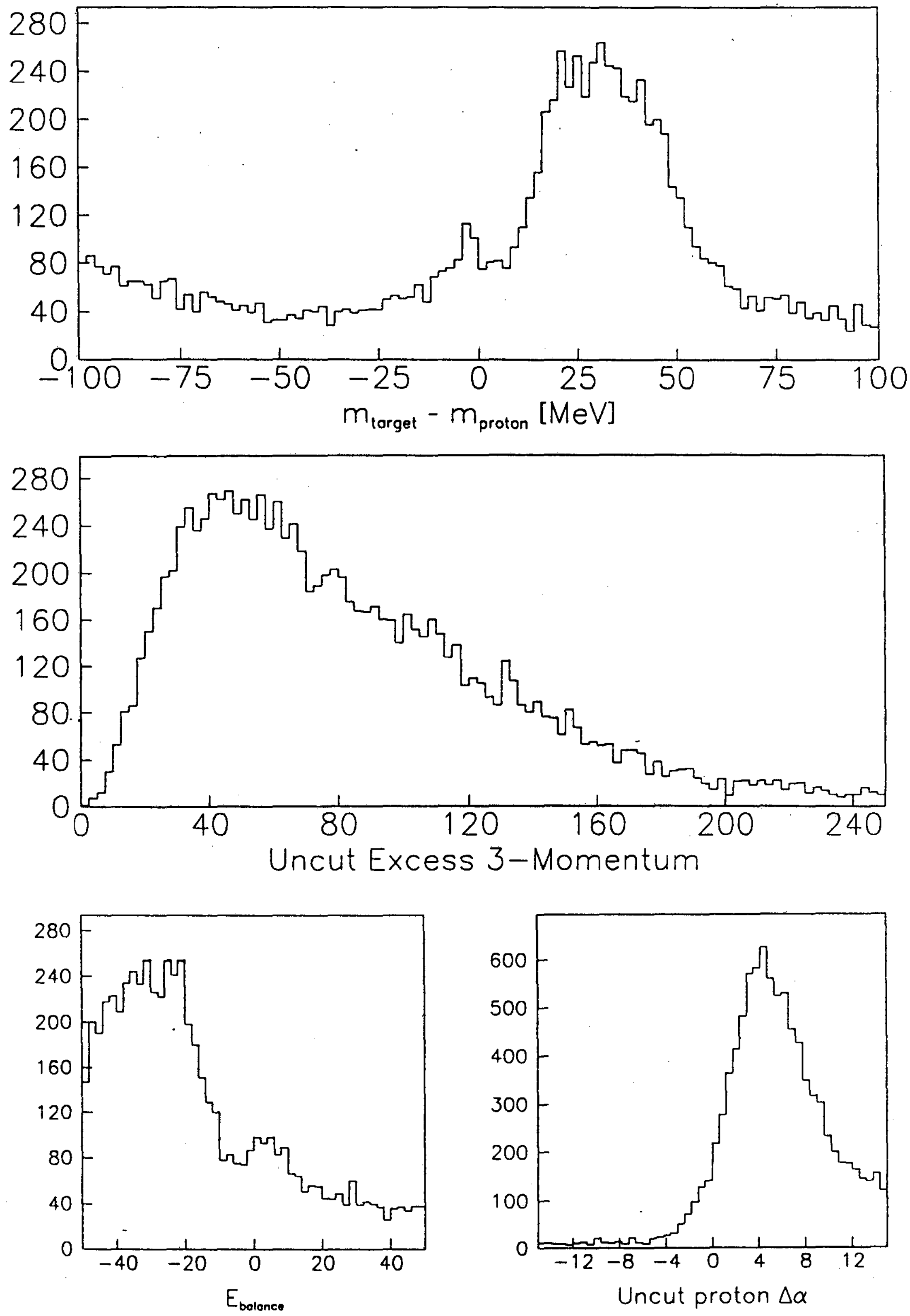

Figure 5.13: Various kinematic quantities for the raw data set.

E_γ [MeV]	Fraction Lost [%]
20.0	3.9 ± 0.4
25.0	1.8 ± 0.3
30.0	1.2 ± 0.2
35.0	0.8 ± 0.2
40.0	0.5 ± 0.1
45.0	0.0

Table 5.5: Fraction of good events lost from the elasticity deviation cut on pions.

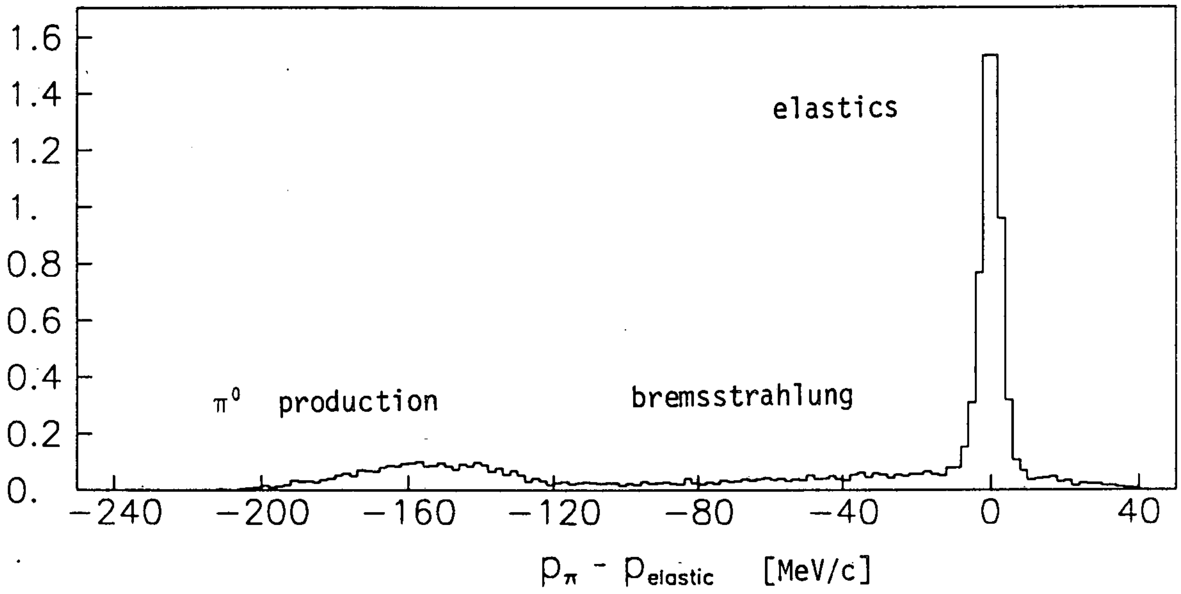

Figure 5.14: A plot of $p_\pi^{meas} - p_\pi^{elas(\theta)}$ for the raw data sample. We can see the three types of events which are most predominate in our data.

The next best resolution is in the total energy of the system. In this regard it makes sense to compare the energy of the photon with the total energy balance of the system, E_{Bal}. For an elastic event, the following equation should hold.

$$E_{Bal} = -E_\gamma$$

In figure 5.15 we show a scatter plot of E_{Bal} versus E_γ. The line satisfying the above equation is clearly visible as the major constituent of the plot. In order to apply a cut on the energy balance, we form the energy balance of the πp system,

$$E^{\pi p}_{Bal} = E_{in} + m_p - E_\pi - E_p.$$

This quantity, which is plotted in figure 5.16, should be peaked at 0MeV for events which are an elastic plus a random photon. Because of the energy resolution of the entire system, to keep from removing more than 1% of the good events we require only that $E^{\pi p}_{Bal} > 0MeV$.

Finally, it is possible to have an elastic event in which the pion decays in the spectrometer and has its momentum misidentified, or the pion rescatters in the liquid hydrogen target (about 1.5% of the time). In order to try to prevent these events from giving us a background, we want to make a cut on the proton's deviation from elasticity. We can parameterize this quantity as a function of photon energy in the same manner as we did the pion.

$$p_p^{meas} - p_p^{elas(\alpha_p)} \approx -2.06 \cdot E_\gamma$$

Unfortunately, the proton momentum resolution is rather poor, and in order to remove fewer than 1% of all good events we have to cut

$$p_p^{meas} - p_p^{elas(\alpha_p)} < +10.0MeV/c.$$

As well as elastics plus a random photon, there is another source of triggers in which the photon is correlated with the π and p. We can have the reaction $\pi^+p \rightarrow \pi^+\pi^\circ p$ occurring, (there is more than sufficient energy in the center of mass to produce π°'s). In order to remove this background, we define a new quantity which is essentially the mass of the photon.

$$m_\gamma^2 = (E_{in} + m_p - E_\pi - E_p)^2 - \mid \vec{p}_{in} - \vec{p}_\pi - \vec{p}_p \mid^2 \qquad (5.10)$$

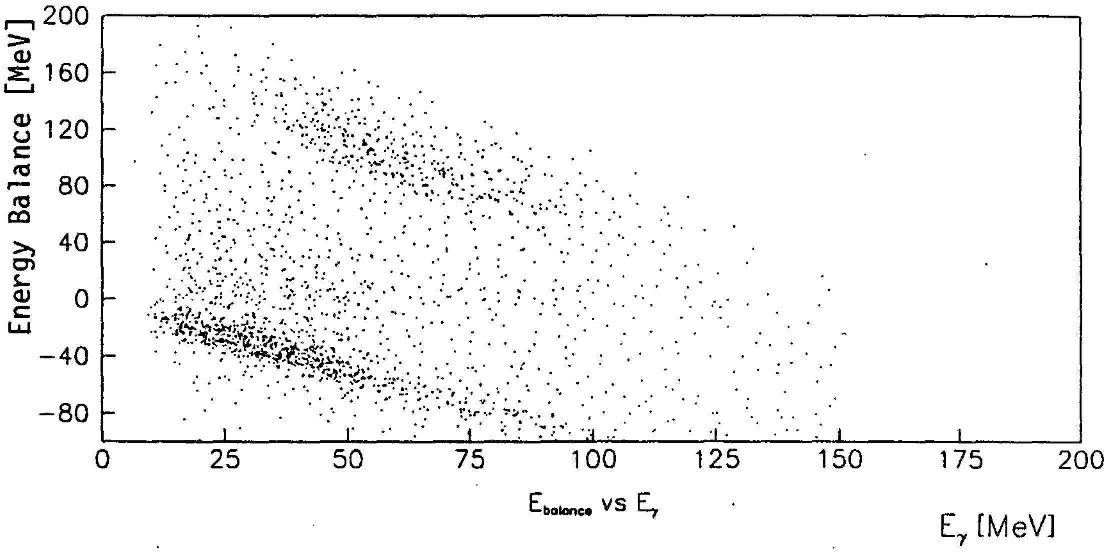

Figure 5.15: The total energy balance plotted against the photon energy. The band at the bottom of the figure is elastics, while the band at the top is π^0's. The bremsstrahlung should appear as a horizontal band at 0MeV; it is too weak compared to the elastics to be seen.

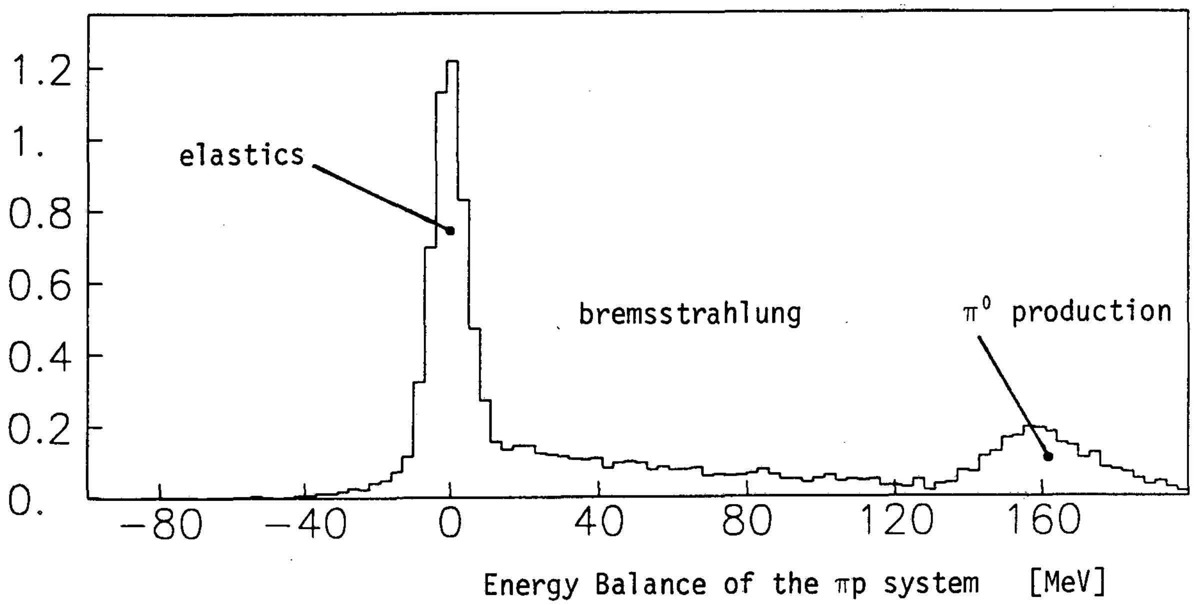

Figure 5.16: The energy balance of the πp system.

For elastic and bremsstrahlung events, this quantity should be $0 MeV^2$, whereas for $\pi^+p \rightarrow \pi^+\pi^\circ p$ there should be a peak at $m^2_{\pi^\circ} = 18200 MeV^2$. In figure 5.17 is shown a plot of this quantity for the raw data set. In order to remove the π°'s, we require that $m^2_\gamma < 7500 MeV^2$.

After the above four cuts have been made, we are left with about 10% of the raw data set. The four kinematic quantities defined earlier are plotted for this data set in figure 5.18. Looking at the $\Delta\alpha_p$ plot, we can see that there is still a lot of background signal in the data sample. However, we can remove a good fraction of it by cutting on $\mid \Delta\alpha_p \mid < 6.0^\circ$, (this cut is at about 3.5σ). After this last cut has been performed, we are left with about 5.6% of the raw data set. There is still a tail of some sort of background which extends under the true signal in the $\Delta\alpha_p$ spectrum. If we plot $\Delta\alpha_p$ against E_γ, see figure 5.19 we observe that most of this back ground is associated with low energy (under 50MeV) photons. Monte-carlo studies indicate that most of this background comes from elastic events with the pion decaying in the spectrometer mixing in with a random photon, (see section 5.5.4).

It turned out to be virtually impossible to cut away the last bit of background in the data sample. Cutting in $m_t - m_p$ at 50MeV removes some of it, but by no means all of it. In order to make a background subtraction, we needed some idea of how much background there

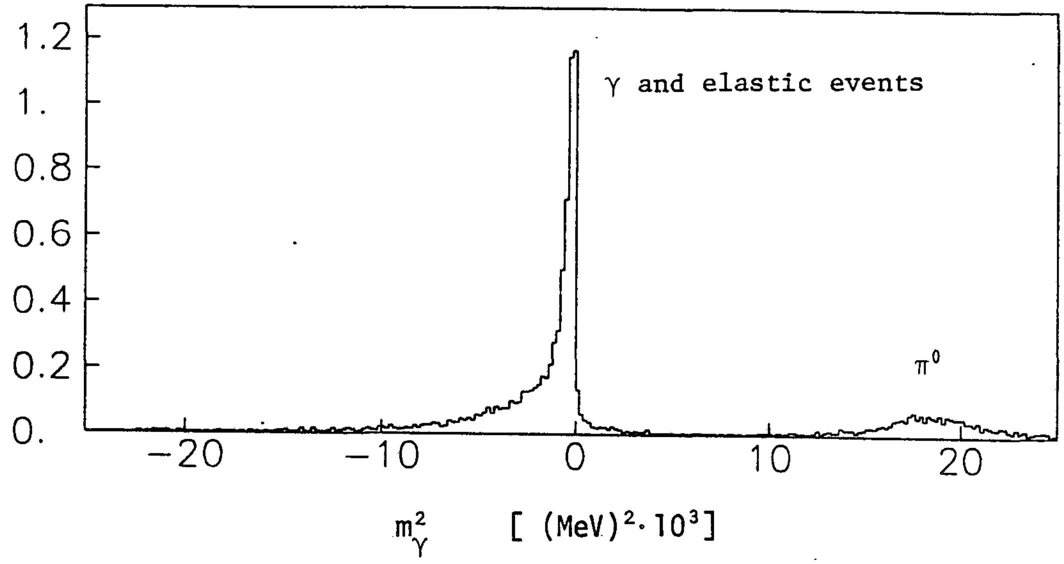

Figure 5.17: Mass of the photon, m_γ^2. This quantity is used to remove π^0 production events.

was. As we believe that this background is due to decaying elastic events in coincidence with a random gamma, the photon is completely uncorrelated with the pion and proton. As such, if we analyze any time window in photon time of flight, the same background will be present. In particular, if we analyze around the γ from one beam burst later in exactly the same manner as we analyzed the correlated photon time peak, then all backgrounds where the gamma is random, (correlated and uncorrelated to the beam) will still be present in the sample. This data set can then be subtracted directly from the real signal to remove all backgrounds containing random photons.

When this analysis was carried out for 86% of the data, we obtained a data set of 355 events which passed all cuts up to this point. Plots of the four kinematic quantities for the backgrounds are shown in figure 5.21.We can then compare 355/.866 = 410 with 1589 events which came from the real data set. At this point we have reduced the 1,240,000 events written to tape down to a data set of 1179 events.

Finally, before we constructed the final cross–section, we performed a 3–C kinematic fit to the hypothesis that the events come from $\pi p \rightarrow \pi p \gamma$ and cut in the resulting χ^2 like variable. For a description of kinematic fitting, see Appendix E. The kinematic fit included all of the measured resolutions of the various detectors and minimized energy and momentum balance by shifting all measured quantities within their measured errors. In

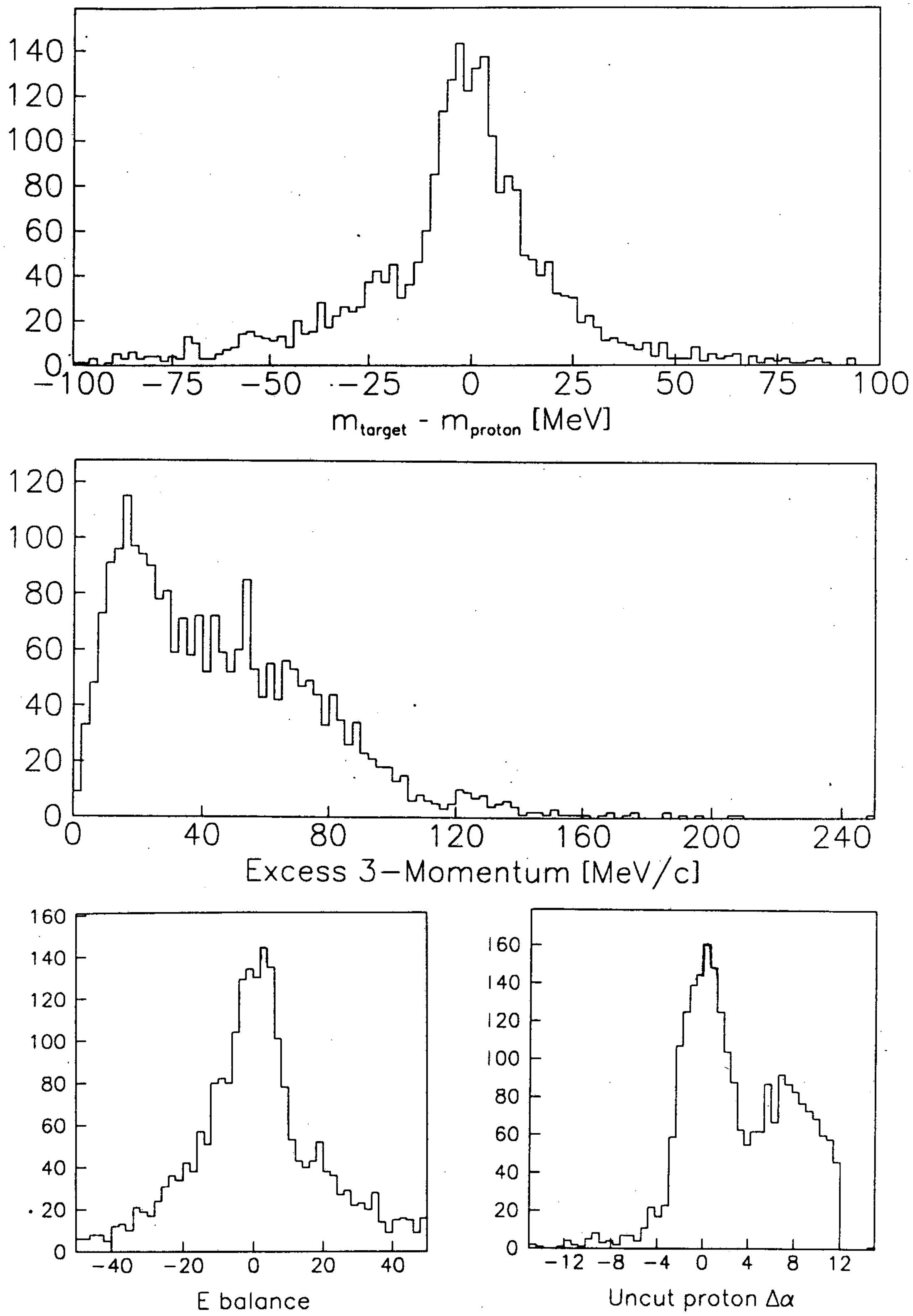

Figure 5.18: The various kinematic quantities after the first level of cutting.

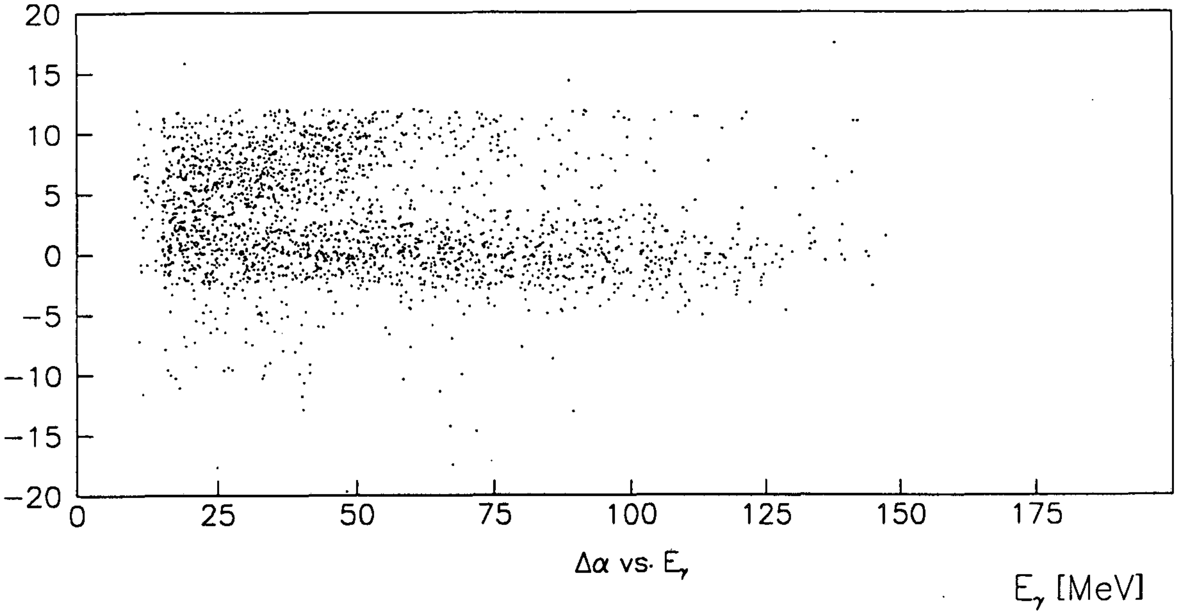

Figure 5.19: A plot of $\Delta\alpha_p$ versus E_γ. The horizontal band at 0° is bremsstrahlung, while the tail above it comes from elastic events.

figure 5.22 we present the resulting χ^2 for both the real data set and the background data set in three ranges of photon energies. It is seen that almost all of the background is in the range of photon energies which are less than 40MeV. We cut the χ^2 at 4.0 in the low data set, at 5.5 in the middle data set, and at 7.0 in the high data set. Table 5.6 indicates the number of events remaining after the kinematic fitting and the χ^2 cutting, the errors are statistical only. The raw counts will be converted into a cross–section in the next chapter.

After this, it was necessary to estimate the number of real events that were lost from the data sample during the cuts. In order to do this, we examined the total energy balance of the system in several ranges of photon energy. We generated these plots for both the data set and the background set and then subtracted the background from the real set. The effect of all the cuts to remove elastic events is always on the negative energy side of the energy balance. By then looking at the number of events on the positive side beyond the point where the cutoff was applied on the negative side we obtained a reasonable estimate for the number of events lost. The fraction varied linearly from 12% at 25Mev to 0% at 45MeV.

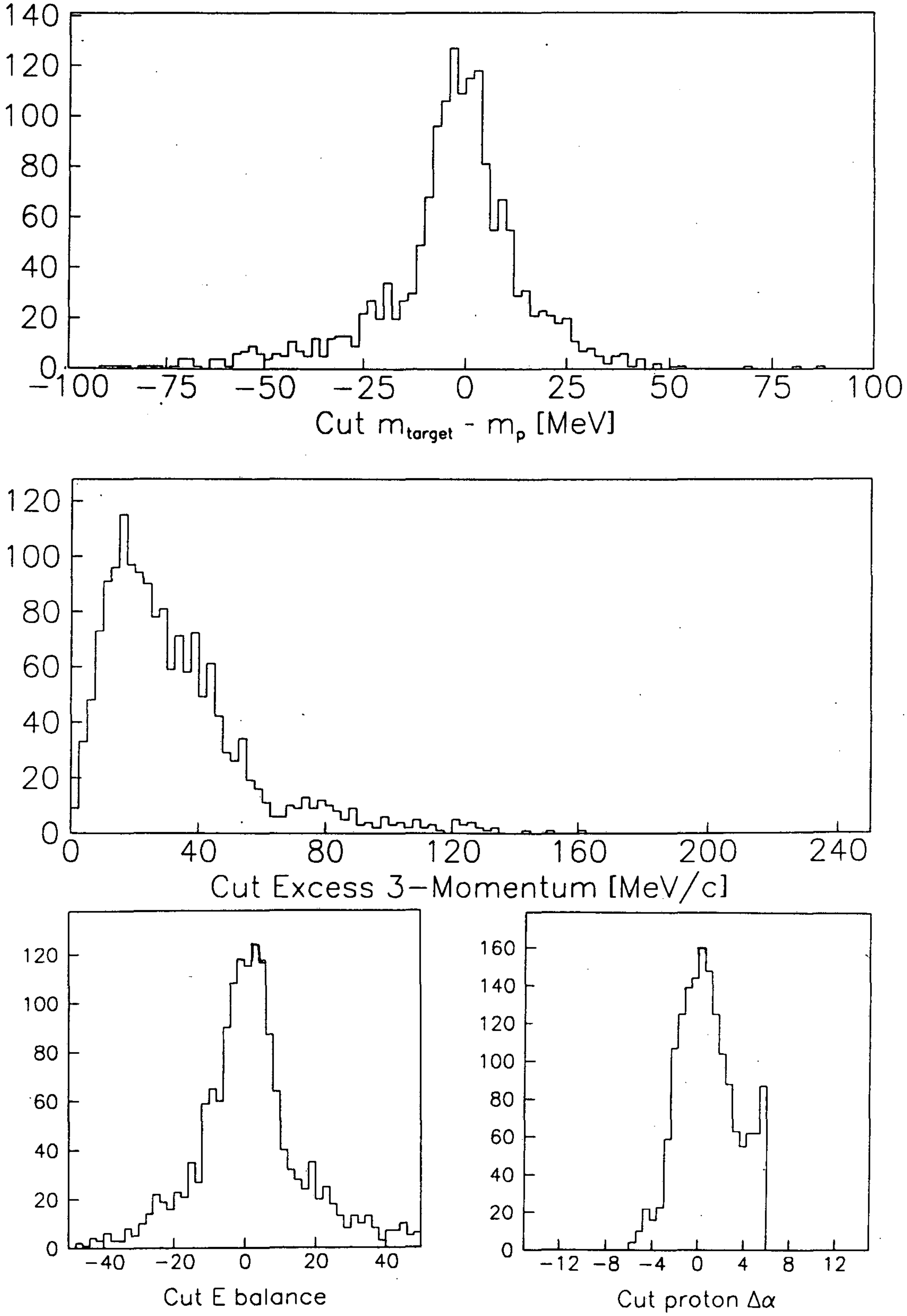

Figure 5.20: The kinematic quantities of all events after the $\Delta\alpha_p$ cut was made.

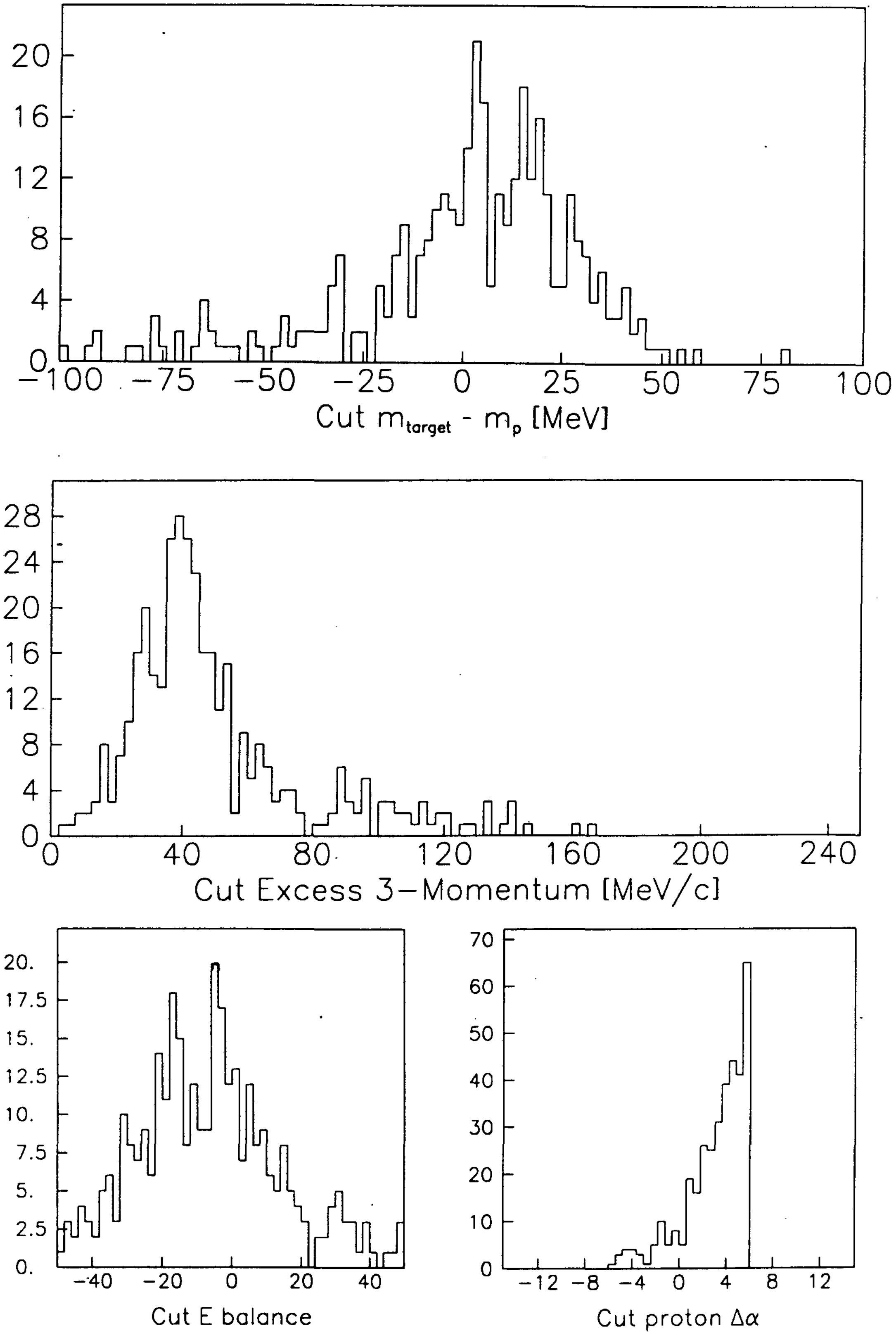

Figure 5.21: Events from the Background data set which passed all cuts.

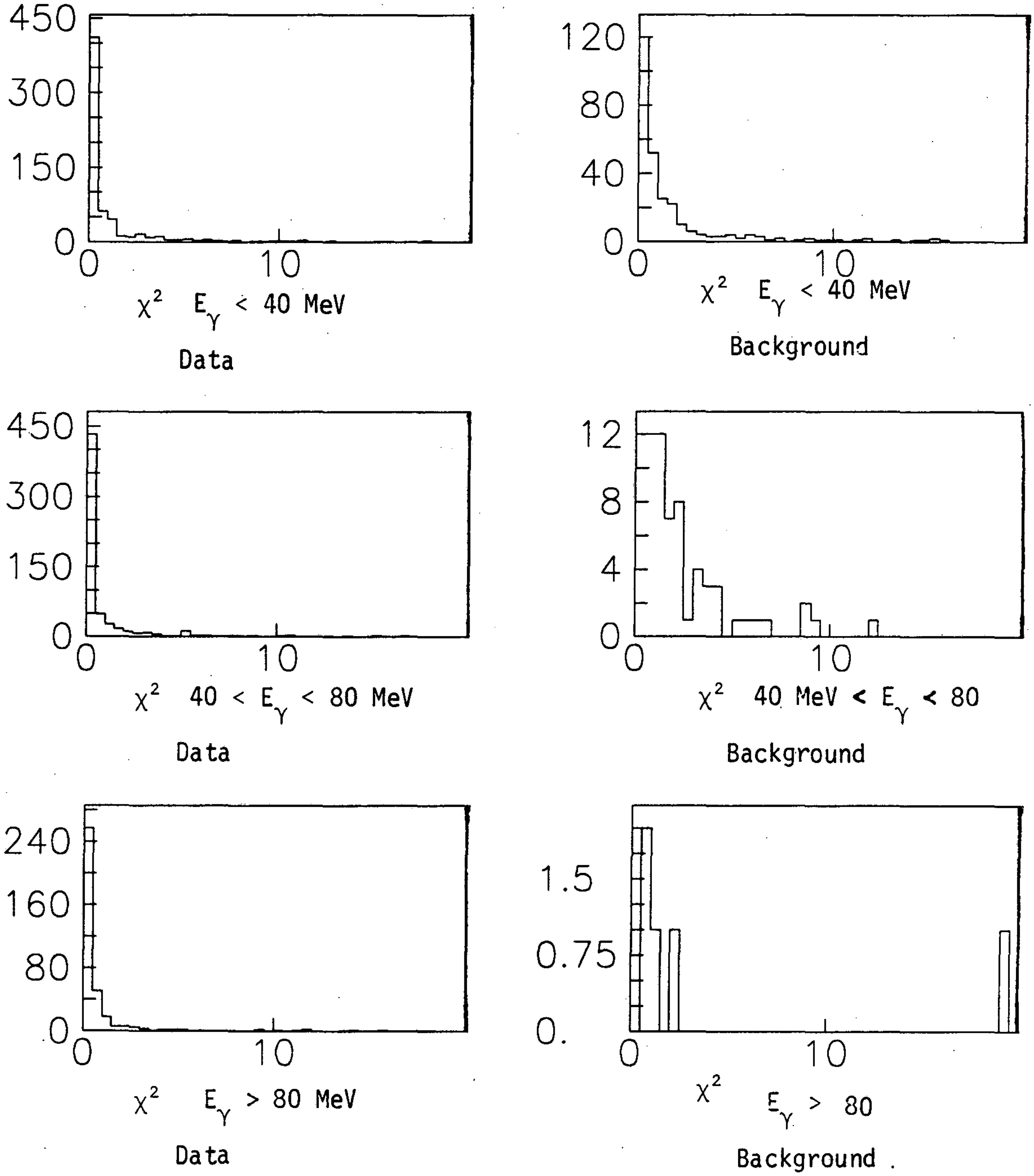

Figure 5.22: The χ^2 returned from the kinematic fit for the real and background data sets.

E_γ [MeV]	Events in Real Sample	Events in Background
20.—30.	245 ± 15.7	98 ± 9.9
30.—40.	215 ± 14.7	92 ± 9.6
40.—50.	180 ± 13.4	44 ± 6.6
50.—60.	152 ± 12.3	13 ± 3.6
60.—70.	126 ± 11.2	3 ± 1.7
70.—80.	112 ± 10.6	2 ± 1.4
80.—90.	104 ± 10.3	3 ± 1.7
90.—100.	88 ± 9.5	0
100.—110.	68 ± 8.4	2 ± 1.4
110.—120.	50 ± 7.2	0
120.—130.	36 ± 6.4	0

Table 5.6: Number of events after all cuts in the real and background data sets.

5.5 Backgrounds in the Spectrometer

There are various sorts of backgrounds that we have in this experiment, and of course there are even more in the experiment using the polarized target. This is simply because we have replaced a very simple target, liquid hydrogen, with a very dirty one, butanol. One of the reasons that we performed this measurement on the liquid hydrogen target was to give us experience in dealing with these backgrounds, and possibly get rid of them in the polarized run. A discussion of the backgrounds seen in the liquid hydrogen target, and what improvements we made in the polarized run are presented below.

5.5.1 Protons in The Pion Spectrometer

A large fraction, (about 50%) of the triggers in the pion spectrometer where caused by protons in the spectrometer. A reaction akin to $\pi^+ n \rightarrow p\gamma$ where the proton is detected by the pion spectrometer and the gamma is seen by the NaI(Tl) array. If a random trigger, such as a muon from the beam halo, is then detected in the proton spectrometer we have what appears as a real event. There is no problem removing this background by simply looking at the pulse–height and time of flights of the pion arm, and the pulse–height in the proton hodoscope. The only problem that it can cause is that the trigger rate will go up, and the tapes will contain mostly garbage. Because this experiment is an absolute measurement of the cross–section, we did not place any hardware cuts on pulse–height in the pion arm to reduce the trigger rate. However, when we used the polarized target, this sort of trigger was about 70% to 80% of our trigger rate. In this case we put a hardware cut on the pulse–height in the pion E counters. However, as the polarized run is to measure an asymmetry and not an absolute cross–section the effects of this hardware cut will cancel in the division.

5.5.2 Sources of Random Photons

There are several sources of random *photons* in the experiment. Figure 5.23 shows a typical γ time spectra associated with a $\pi p \rightarrow \pi p \gamma$ run. One should note that this is the time spectra of all photons, and not just those whose π and p are correlated. In this figure are labeled all the sources of photons that we observe in the detector. The sources which are correlated with the beam pion are such things as π° production, charge exchange on nuclei and neutrons detected, whereas the predominant uncorrelated sources are Michel electrons generated inside the NaI(Tl) array.

The label *Background Michel Electrons* refers to Michel electrons which are produced in the NaI(Tl) array. Pions which backscatter into the NaI(Tl) array will stop somewhere near the middle of the detector and decay, $(\pi^{+} \rightarrow \mu^{+}\nu_{\mu})$. The resulting muons have very little energy and also remain in the NaI(Tl) array. It is the final decay of these muons, $(\mu^{+} \rightarrow e^{+}\nu_{e}\overline{\nu}_{\mu})$ which produce the Michel electrons. During the polarized run, we installed some extra hardware to tag these Michel electrons, in the hope allowing us to get rid of them in the analysis. Every time that the anti–counter in front of the NaI fired, we opened a $7\mu s$ wide gate. If we then got a real trigger during this gate, we tagged the event with a pattern bit. When we later went back and looked at the Energy spectra of the photons with a bit set, we got essentially a Michel spectrum, and the time spectrum of the remaining events was nearly devoid of the flat background. However, this tagging was only done for a few runs during the unpolarized data, and I did not use it in the analysis.

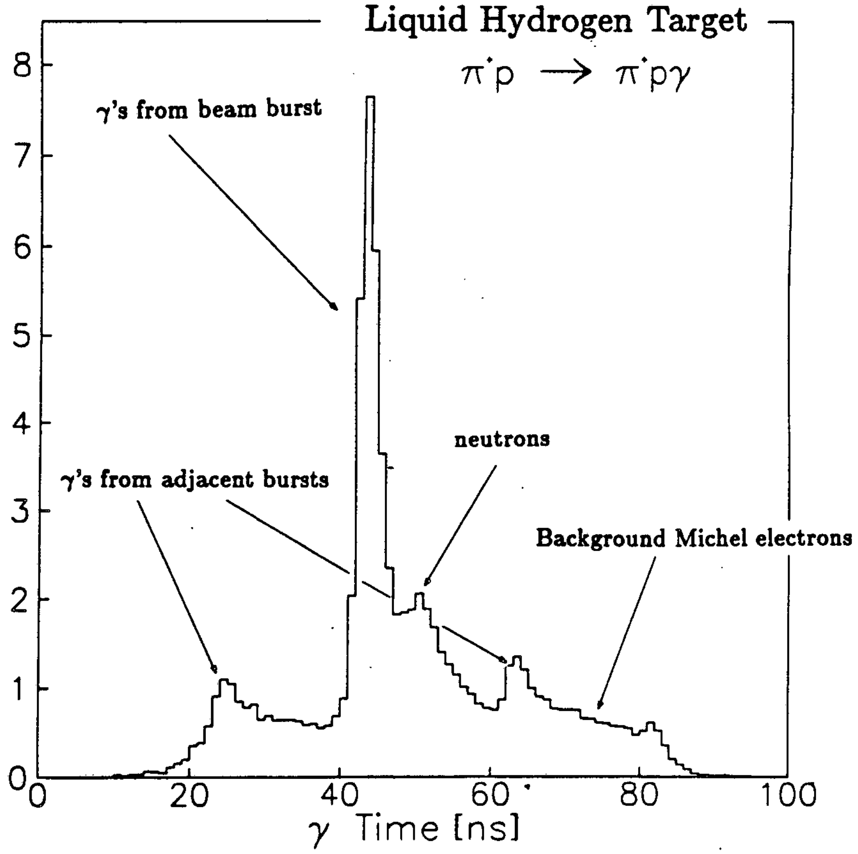

Figure 5.23: Time spectra of all γ's in a $\pi p \rightarrow \pi p\gamma$ run.

5.5.3 πp $\rightarrow$ πp Plus Random γ

Any random γ in coincidence with an elastic event will produce a trigger. We have simulated this background with monte–carlo, and the conclusion is that it can make only the smallest of contributions for the lowest energy photon bins. Plots showing $m_t - m_p$ and $\Delta\alpha$ from the monte–carlo are shown in figure 5.24. A simple cut on the pion deviation from elasticity removes all the events in the monte–carlo sample.

5.5.4 πp $\rightarrow$ πp with Decay Plus Random γ

If in the previous reaction, the pion decays in flight on its way through the spectrometer, it is possible to generate a sizeable number of events that look exactly $\pi p \rightarrow \pi p\gamma$ for low energy photons. We examined this reaction with monte–carlo studies and the results are presented in figure 5.25. The tails in the **Cut** $\Delta\alpha$ plot are seen to extend into the region of $\pi p \rightarrow \pi p\gamma$ events. However, this background is still one of which we can dispose by analyzing around one beam burst later in photon time, and subtracting.

5.5.5 π^+Nucleus $\rightarrow$ π^+pX Plus Random γ

This reaction is a quasi–free scattering in coincidence with a random photon. The only place we can get such quasi–free scattering is from our target walls and as such this is a small contribution to our signal. As the photon in this process is completely uncorrelated with the pion and proton, this background is removed when we subtract the contribution from the second gamma time peak as discussed in the previous sections. This background will be much larger in the polarized data sample, but the same technique can be used to get rid of it.

5.5.6 Quasifree Bremsstrahlung

This process is bremsstrahlung off a bound proton, which is then knocked free. Because of the small amount of material that was not hydrogen in the target, this reaction is negligible in this experiment. However, in the polarized running this could have a significant contribution and much *empty target* data was taken to be able to perform a subtraction.

In the unpolarized experiment, the thickness of the target vessel was less than 2% of the liquid Hydrogen in gm/cm^2. We tried to find evidence of this reaction in our data sample

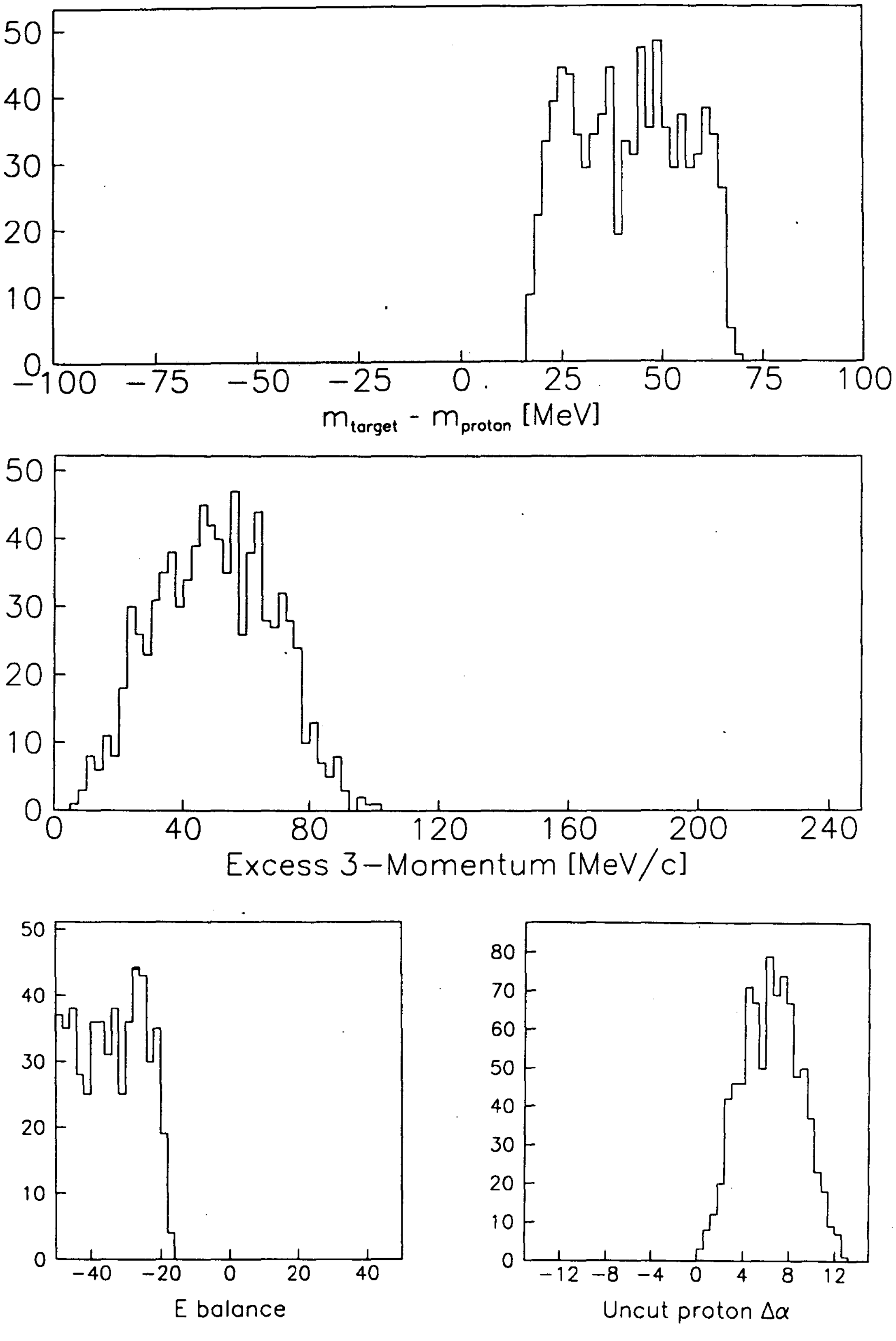

Figure 5.24: Monte–carlo calculations for $\pi p \rightarrow \pi p + \gamma_{random}$.

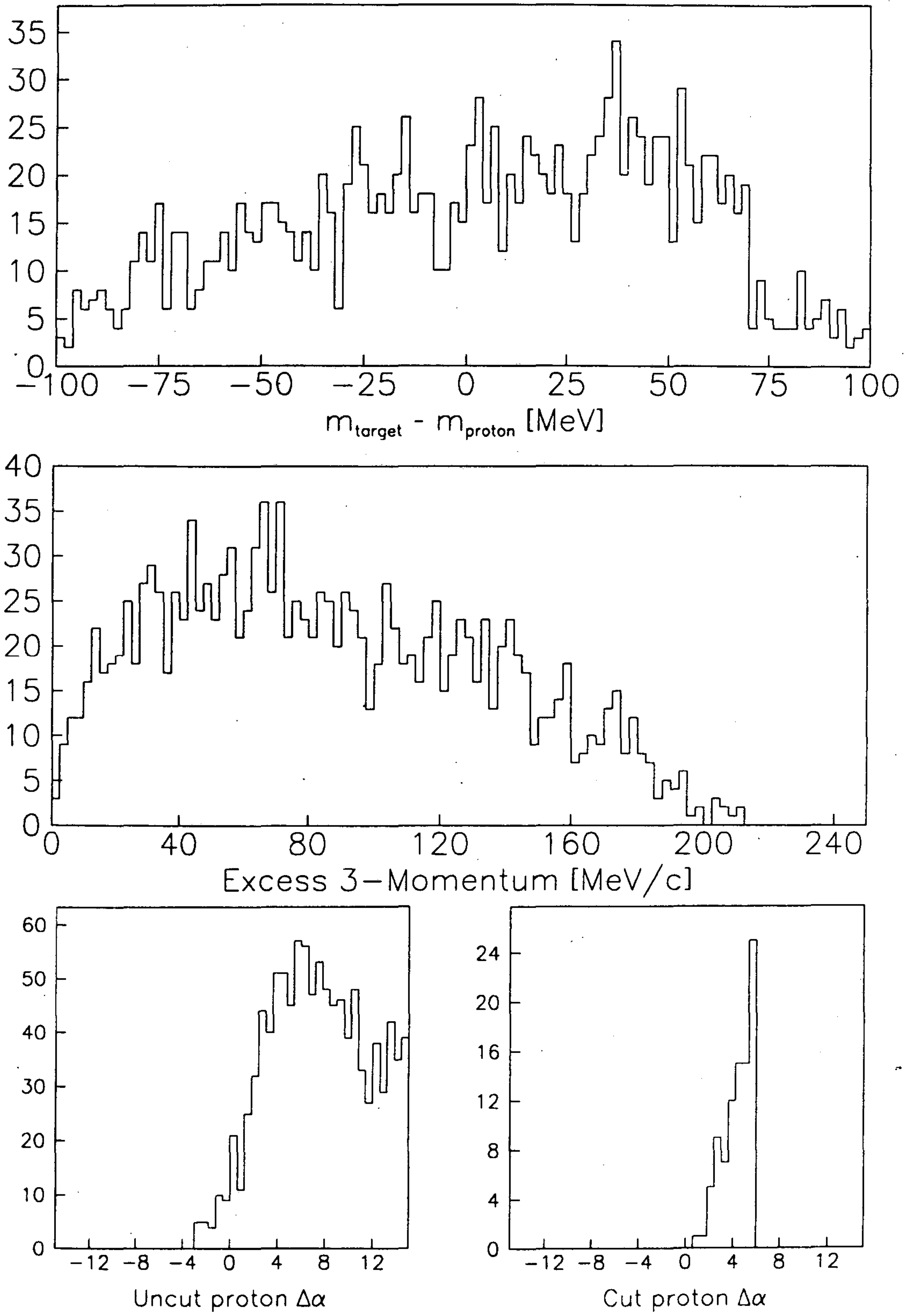

Figure 5.25: Monte–carlo calculations for $\pi p \to \pi p + \gamma_{random}$ with the scattered π^+ decaying in flight.

by analyzing a subset of the total data set which came from near the mylar windows. The spectra from this region looked no different from that at the center of the target. In particular one would expect a peak in the energy balance at about the binding energy of carbon for the reaction $\pi^+C^{12} \rightarrow \pi^+pB^{11}\gamma$. No such peak was visible.

5.5.7 π^+p→ $\pi^+\pi^0$p

π^0 production will give a trigger which in all respects is exactly the same as a bremsstrahlung trigger. However, because of the large amount of information measured in this experiment is is very easy to cut away. We can reconstruct the mass of the particle identified as a γ by only looking at the final state π and p.

$$m_\gamma^2 = (E_{in} + m_p - E_\pi - E_p)^2 - (\vec{P}_{in} - \vec{p}_\pi - \vec{p}_p)^2$$

When this quantity is calculated, events with π^0's will sit in a peak at $(135MeV)^2$, whereas πp → πpγ and πp → πp events will sit in a peak at $(0MeV)^2$. A plot of this quantity is shown in figure 5.17.

If one looks at where the π^+'s for π^0 production are seen, they all appear at the most forward angles observed. Because of the acceptance change that occurred when we changed from unpolarized to polarized, we essentially cut away all of these events, (see figure 3.6). This may or may not have been a fortuitous accident, and it led to some worry early in the polarized run when we did not see the π^0 production.

Chapter 6

Results of the Analysis and Fits to Theory

6.1 Calculation of The Cross–section

In order to get from the results in table 5.6 to a cross–section, we perform the calculation

$$\frac{d^5\sigma}{d\Omega_\pi d\Omega_\gamma dE_\gamma} = \frac{N_{scat}}{N_{in}\cdot\epsilon_{ch}}\cdot\frac{1}{\Omega_\pi}\cdot\frac{1}{\Omega_\gamma}\cdot\frac{1}{E_\gamma}\cdot\frac{1}{N_{proton}}\cdot\frac{1}{\epsilon_\pi}\cdot\frac{1}{\epsilon_p}\cdot\frac{1}{\eta_{decay}}\cdot\frac{1}{\epsilon_\gamma} \tag{6.1}$$

- N_{scat} is the number of good events.

- $N_{in}\cdot\epsilon_{ch}$ is the number of incident pions multiplied by the wire chamber efficiency. This quantity was calculated for every run analyzed and summed, this was necessary because of the large fluctuations in chamber efficiency over the length of the experiment. We have that

  $$N_{in}\cdot\epsilon_{ch} = (1.867 \pm 0.080)\cdot 10^{12}$$

  The 4.3% error in this quantity arises from the uncertainty in the incident flux, 3.2% and the uncertainty in the wire chamber efficiency, 2.8%.

- N_{proton} is the number of protons in the liquid hydrogen target. It is calculated in section 5.2 and is $N_{proton} = (613. \pm 3.7)\cdot 10^{-6}/mb$.

- Ω_π is the effective solid angle of the pion spectrometer. This value was calculated as a function of E_γ in section 3.1.4 and has an average error of about 2%.

- Ω_γ is the solid angle of the NaI(Tl) array; and is 125.75 ± 0.70msr as calculated by monte–carlo.
- E_γ is the bin width in photon energy.
- ϵ_π is the pion reconstruction probability ignoring chamber efficiency, but including scintillator efficiencies. This is the same as for the elastic data, $\epsilon_\pi = 87.5 \pm 2.1\%$.
- ϵ_p is the proton detector efficiency which was calculated in section 5.1.2. It averaged about 90% for the $\pi p \rightarrow \pi p \gamma$ data, but event by event corrections were applied.
- ϵ_γ is the efficiency of the NaI, which includes both the detection efficiency, (see section 4.4.2) and the chance that a photon is lost due to resolution, (see section 5.1.3).
- η_{decay} is the correction for pions decaying and being lost.

In order to calculate the cross–section, we went through the events that survived all cuts and assigned a weight based on detector efficiencies, solid angles and decay probability. This weighting was performed for both the real and background data sets, and then a subtraction was performed. This weighting was made such that the sample is normalized to an Ω_π of 130.0 msr. One can then calculate the cross–sections from the weighted sample as:

$$\frac{d^5\sigma}{d\Omega_\pi d\Omega_\gamma dE_\gamma} = \frac{N_{scat}}{N_{in} \cdot \epsilon_{ch}} \cdot \frac{1}{\Omega_\pi} \cdot \frac{1}{\Omega_\gamma} \cdot \frac{1}{E_\gamma} \cdot \frac{1}{N_{proton}}$$

Because of the large angular range accepted by the pion spectrometer, (55° to 95°), we felt it desirable to also split the data sample into a low and a high pion–angle set. In order to do this, the only change necessary was to weight the events with the solid angle of the partial spectrometer rather than the entire spectrometer. These solid angles were also calculated in section 3.1.4, see figures 3.8 and 3.9. In these two data sets the weighting was normalized to 65.00msr rather than the 130.00 for the entire data set. Tables 6.1 and 6.2 present the number of weighted events and the calculated cross–sections as a function of photon energy. The errors quoted include all effects.

In order to check the stability of these cross–sections against the various cuts, we generated several alternative sets of cuts which were performed after the elastic events had been removed. Amongst these were (1) cuts in $m_t - m_p$ before the kinematic fitting was done, (2) not performing the cut in $\Delta\alpha_p$, and (3) performing a 2–C kinematic fit with the photon energy free, and then cutting on the difference between the measured and predicted photon energy. All of these procedures yielded the same cross–sections in the entire data set to within 0.5σ. Also, because of the rather large errors on the two fractional data sets we present the data in bins of larger photon energy. The cross–sections for the three angular bins with 12MeV wide photon energy bins are presented in table 6.3 and with 15MeV wide bins in photon energy are presented in table 6.4.

E_γ [MeV]	Weighted Events	$\frac{d^5\sigma}{d\Omega_\pi d\Omega_\gamma dE_\gamma}[\frac{nb}{sr^2 MeV}]$
20.—30.	$294. \pm 47.2$	1.57 ± 0.26
30.—40.	$222. \pm 40.0$	1.19 ± 0.22
40.—50.	$243. \pm 33.5$	1.30 ± 0.19
50.—60.	$260. \pm 30.4$	1.39 ± 0.17
60.—70.	$234. \pm 27.0$	1.25 ± 0.15
70.—80.	$217. \pm 25.8$	1.16 ± 0.15
80.—90.	$201. \pm 24.5$	1.07 ± 0.14
90.—100.	$186. \pm 23.5$	1.00 ± 0.13
100.—110.	$142. \pm 20.4$	0.76 ± 0.11
110.—120.	$118. \pm 18.4$	0.63 ± 0.10
120.—130.	$108. \pm 19.4$	0.58 ± 0.11

Table 6.1: Cross–sections over all θ_π.

In figures 6.1, 6.2 and 6.3 we present plots of the entire data set in 10MeV wide bins in photon energy, and the two fractional data sets in 15MeV wide bins in photon energy. The errors in this figure are both statistical and systematic combined, and represent our best estimate of the total errors in the system. The data set for pion angles between 75° and 95° contains one fewer points than the low–angle data set. This is because of uncertainties in the solid angle of the πp system for high energy photons. The uncertainty in this acceptance is too large, and the statistics too low to get a result here.

E_γ	$55^\circ < \theta_\pi < 75^\circ$		$75^\circ < \theta_\pi < 95^\circ$	
$[MeV]$	Weighted Events	$\frac{d^5\sigma}{d\Omega_\pi d\Omega_\gamma dE_\gamma}$	Weighted Events	$\frac{d^5\sigma}{d\Omega_\pi d\Omega_\gamma dE_\gamma}$
20.—30.	121 ± 31.2	1.29 ± 0.34	168 ± 31.2	1.80 ± 0.34
30.—40.	79 ± 24.0	0.85 ± 0.26	141 ± 29.4	1.50 ± 0.32
40.—50.	140 ± 22.4	1.50 ± 0.25	104 ± 22.6	1.11 ± 0.25
50.—60.	118 ± 17.4	1.26 ± 0.19	140 ± 21.5	1.50 ± 0.24
60.—70.	115 ± 16.1	1.23 ± 0.18	115 ± 18.2	1.23 ± 0.20
70.—80.	112 ± 15.6	1.20 ± 0.18	95 ± 17.0	1.02 ± 0.19
80.—90.	118 ± 16.2	1.26 ± 0.18	72 ± 14.8	0.77 ± 0.16
90.—100.	97 ± 14.0	1.04 ± 0.16	82 ± 16.7	0.88 ± 0.18
100.—110.	65 ± 11.5	0.69 ± 0.13	87 ± 18.7	0.93 ± 0.20
110.—120.	71 ± 11.5	0.76 ± 0.13		
120.—130.	58 ± 10.7	0.63 ± 0.12		

Table 6.2: Cross-sections in $\frac{nb}{sr^2 MeV}$ for θ_π between 55° and 75° and θ_π between 75° and 95°.

E_γ [MeV]	$\frac{d^5\sigma}{d\Omega_\pi d\Omega_\gamma dE_\gamma}$ $55^\circ < \theta_\pi < 95^\circ$	$\frac{d^5\sigma}{d\Omega_\pi d\Omega_\gamma dE_\gamma}$ $55^\circ < \theta_\pi < 75^\circ$	$\frac{d^5\sigma}{d\Omega_\pi d\Omega_\gamma dE_\gamma}$ $75^\circ < \theta_\pi < 95^\circ$
20.—32.	1.46 ± 0.24	1.07 ± 0.31	1.82 ± 0.31
32.—44.	1.22 ± 0.20	1.27 ± 0.23	1.13 ± 0.28
44.—56.	1.48 ± 0.18	1.48 ± 0.21	1.48 ± 0.23
56.—68.	1.25 ± 0.15	1.14 ± 0.16	1.33 ± 0.20
68.—80.	1.14 ± 0.14	1.14 ± 0.16	1.04 ± 0.18
80.—92.	1.10 ± 0.13	1.23 ± 0.18	0.87 ± 0.16
92.—104.	0.90 ± 0.12	0.91 ± 0.14	0.90 ± 0.18
104.—116.	0.64 ± 0.10	0.73 ± 0.12	
116.—128.	0.67 ± 0.11	0.72 ± 0.12	

Table 6.3: Cross-sections $[\frac{nb}{sr^2 MeV}]$ in 12MeV wide bins.

E_γ [MeV]	$\frac{d^5\sigma}{d\Omega_\pi d\Omega_\gamma dE_\gamma}$ $55° < \theta_\pi < 95°$	$\frac{d^5\sigma}{d\Omega_\pi d\Omega_\gamma dE_\gamma}$ $55° < \theta_\pi < 75°$	$\frac{d^5\sigma}{d\Omega_\pi d\Omega_\gamma dE_\gamma}$ $75° < \theta_\pi < 95°$
20.—35.	1.52 ± 0.22	1.17 ± 0.27	1.83 ± 0.29
35.—50.	1.19 ± 0.17	1.25 ± 0.20	1.12 ± 0.23
50.—65.	1.35 ± 0.15	1.33 ± 0.17	1.34 ± 0.19
65.—80.	1.19 ± 0.13	1.13 ± 0.15	1.16 ± 0.17
80.—95.	1.08 ± 0.13	1.21 ± 0.15	0.85 ± 0.15
95.—110.	0.81 ± 0.10	0.79 ± 0.12	0.86 ± 0.16
110.—125.	0.68 ± 0.09	0.78 ± 0.11	

Table 6.4: Cross–sections in 15MeV wide bins.

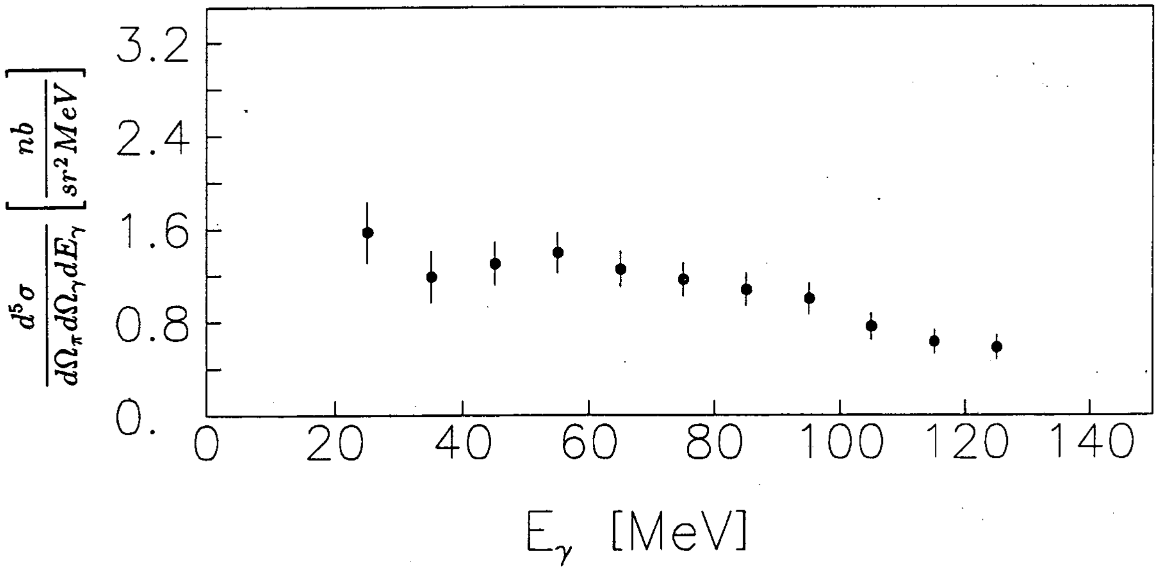

Figure 6.1: The cross–sections for the data: $55° < \theta_\pi < 95°$.

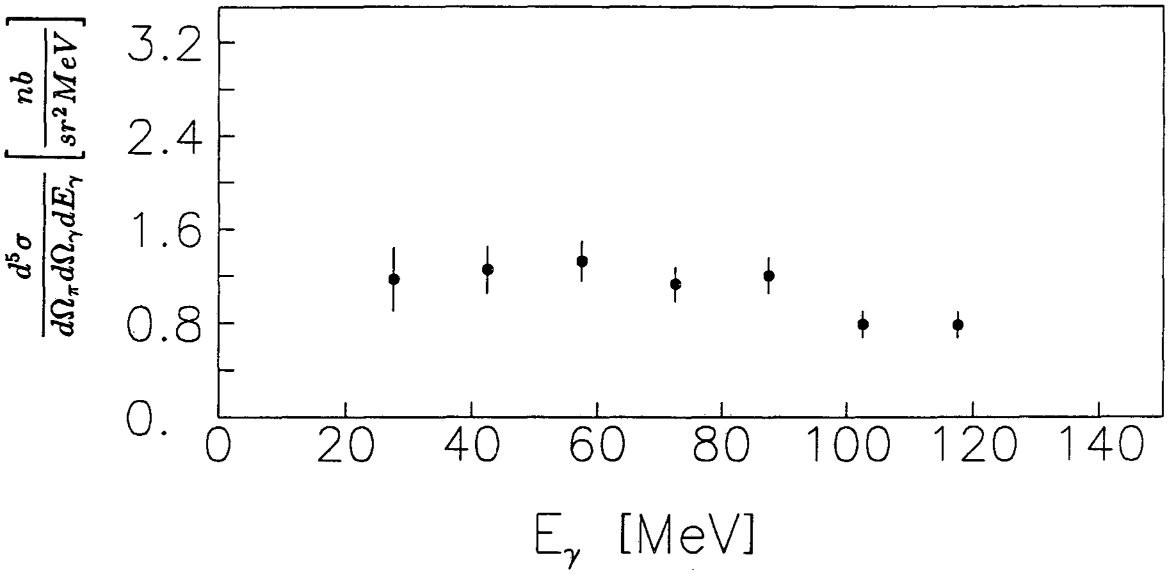

Figure 6.2: The cross–sections for the data: 55° < θ_π < 75°.

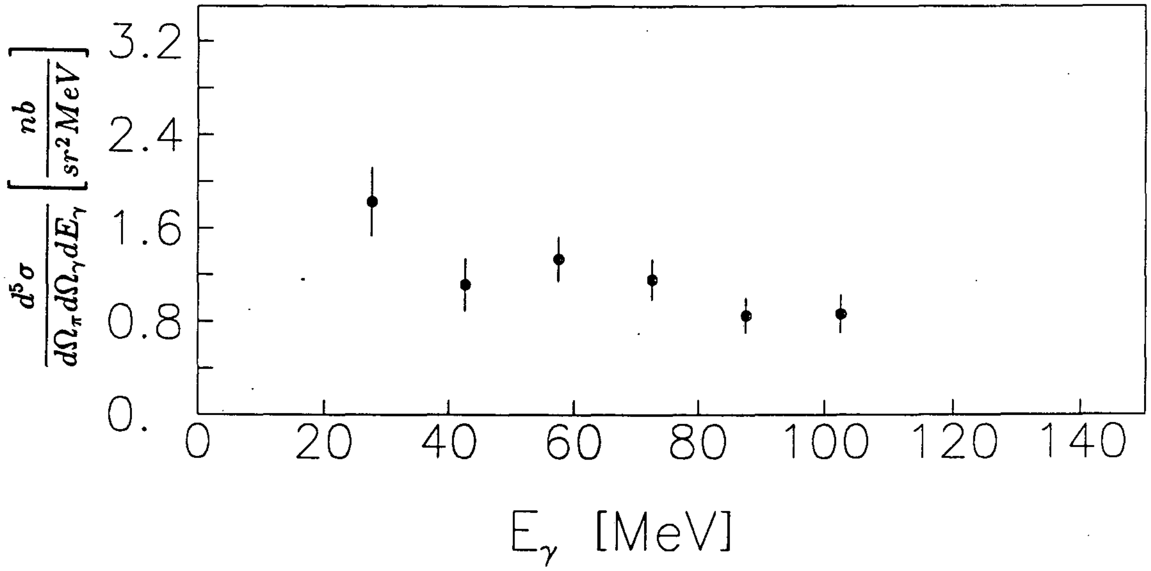

Figure 6.3: The cross–sections for the data: 75° < θ_π < 95°.

6.2 Fits to Theory

In order to fit the MIT theory to our data, it was necessary to fold the acceptances of our detector into the MIT theory. To do this we generated a set of 1000 monte–carlo events with the STINGO program. The following variables were thrown uniformly over the faces of the various detectors.

- E_γ uniformly between 20MeV and 130MeV.
- $\cos\theta_\gamma$ uniformly between 108° and 132°.
- ϕ_γ uniformly between -12° and $+12^\circ$.
- $\cos\theta_\pi$ uniformly between 50° and 100°.
- ϕ_π uniformly between 167° and 193°.

All other quantities are then uniquely determined if we are to satisfy the kinematics of a $\pi p \rightarrow \pi p \gamma$ event. For every one of these monte–carlo events, we then went through and evaluated the MIT cross–section using the program TSECT00 as provided to us by S. Kumano[50]. The TSECT00 code has as input $(\alpha_\gamma, \beta_\gamma, \alpha_\pi, \beta_\pi, E_\gamma, E_{in})$, and returns the cross–section and polarization asymmetry at each point. These cross–sections were then averaged over the photon energy bins in which we present our data, and these values were compared with our data. The analysis gave an average of about 90 events per 10MeV wide bin over the entire data sample, while about 70 events per 15MeV wide bin for the two smaller data sets. We limited ourselves to only 1000 events because of the large amount of CPU time required to perform these averages. Each call to the TSECT00 program requires about 7.8 CPU seconds on a a VAX™ 8650 computer. We require one call per monte–carlo event per magnetic moment of the Δ. The results of these calculations are presented in tables 6.5, 6.6 and 6.7.

In order to determine which value of μ_Δ best fits our data, we define the quantity:

$$\chi^2 = \frac{1}{n}\sum_{i=1}^{n}\left[\frac{\frac{d^5\sigma^{meas}}{d\Omega_\pi d\Omega_\gamma dE_\gamma}(E_\gamma) - \frac{d^5\sigma^{MIT}}{d\Omega_\pi d\Omega_\gamma dE_\gamma}(E_\gamma, \mu_\Delta)}{stddev_i(E_\gamma)}\right]^2 . \tag{6.2}$$

---

[50] This code was written by J. Martinez and S. Kumano for their thesis work at MIT. It is the code they used to fit the UCLA data. See section 2.3 for the appropriate references.

E_γ $[MeV]$	μ_Δ 2.0	μ_Δ 2.4	μ_Δ 2.5	μ_Δ 2.6	μ_Δ 2.7	μ_Δ 2.8	μ_Δ 2.9	μ_Δ 3.0	μ_Δ 3.1	μ_Δ 3.2
25.	1.516	1.530	1.534	1.539	1.543	1.548	1.553	1.558	1.563	1.586
35.	1.231	1.264	1.274	1.284	1.295	1.307	1.319	1.332	1.346	1.360
45.	1.141	1.201	1.220	1.240	1.262	1.286	1.311	1.338	1.367	1.397
55.	1.232	1.323	1.355	1.389	1.427	1.468	1.513	1.561	1.612	1.667
65.	1.219	1.319	1.360	1.407	1.460	1.520	1.586	1.658	1.737	1.822
75.	1.310	1.366	1.495	1.455	1.514	1.584	1.664	1.754	1.855	1.965
85.	1.455	1.349	1.358	1.381	1.417	1.468	1.533	1.612	1.705	1.812
95.	1.579	1.277	1.242	1.224	1.221	1.235	1.265	1.311	1.373	1.451
105.	1.840	1.323	1.221	1.146	1.088	1.046	1.020	1.010	1.017	1.041
115.	2.162	1.523	1.352	1.234	1.129	1.039	0.964	0.903	0.856	0.823
125.	2.443	1.730	1.544	1.401	1.270	1.152	1.046	0.952	0.871	0.802

Table 6.5: The MIT theory averaged over the entire acceptance of our detector.

E_γ $[MeV]$	μ_Δ 2.0	μ_Δ 2.4	μ_Δ 2.5	μ_Δ 2.6	μ_Δ 2.7	μ_Δ 2.8	μ_Δ 2.9	μ_Δ 3.0	μ_Δ 3.1	μ_Δ 3.2
27.5	1.100	1.110	1.113	1.116	1.120	1.125	1.129	1.134	1.139	1.145
42.5	0.868	0.913	0.929	0.946	0.964	0.984	1.005	1.028	1.053	1.097
57.5	0.866	0.958	0.993	1.033	1.078	1.127	1.181	1.240	1.304	1.372
72.5	1.006	1.078	1.122	1.176	1.240	1.315	1.401	1.496	1.602	1.719
87.5	1.359	1.171	1.166	1.178	1.206	1.252	1.314	1.394	1.490	1.603
102.5	1.805	1.291	1.207	1.140	1.090	1.058	1.043	1.046	1.067	1.104
117.5	2.312	1.586	1.440	1.308	1.190	1.087	0.977	0.922	0.861	0.814

Table 6.6: The MIT theory averaged over the acceptance of our detector with $55° < \theta_\pi < 75°$.

E_γ [MeV]	μ_Δ 2.0	μ_Δ 2.4	μ_Δ 2.5	μ_Δ 2.6	μ_Δ 2.7	μ_Δ 2.8	μ_Δ 2.9	μ_Δ 3.0	μ_Δ 3.1	μ_Δ 3.2
27.5	1.708	1.733	1.741	1.748	1.756	1.763	1.771	1.780	1.788	1.797
42.5	1.446	1.507	1.525	1.544	1.564	1.586	1.608	1.632	1.657	1.683
57.5	1.520	1.618	1.651	1.688	1.728	1.772	1.819	1.869	1.924	1.981
72.5	1.584	1.653	1.689	1.733	1.785	1.844	1.911	1.986	2.068	2.158
87.5	1.640	1.517	1.517	1.528	1.550	1.585	1.632	1.691	1.761	1.844
102.5	1.669	1.219	1.230	1.183	1.148	1.127	1.119	1.125	1.144	1.176
117.5	1.755	1.267	1.171	1.086	1.011	0.946	0.891	0.847	0.814	0.790

Table 6.7: The MIT theory averaged over the acceptance of our detector with $75° < \theta_\pi < 95°$.

In figures 6.4, 6.5 and 6.6 are plotted χ^2 against μ_Δ in units of the proton magnetic moment. We plot χ^2 including and excluding points with $E_\gamma > 115.MeV$. The exclusion is because the theory is not valid at these high energies. In the entire data set, the minimum of $\chi^2 = 4.65$ and occurs at $\mu_\Delta = 2.80\mu_p$ and $\chi^2 + 1$ occurs at $\mu_\Delta = 2.65\mu_p$ and $3.0\mu_p$. For the low angle data set, the minimum of $\chi^2 = 1.71$ and occurs at $\mu_\Delta = 2.80\mu_p$. The values of μ_Δ for $\chi^2 + 1$ are $\mu_\Delta = 2.55\mu_p$ and $\mu_\Delta = 3.05\mu_p$. Finally, for the large angle data set the minimum of $\chi^2 = 6.42$ and occurs at $\mu_\Delta = 2.40\mu_p$. The $\chi^2 + 1$ values are $\mu_\Delta = 2.10\mu_p$ and $\mu_\Delta = 2.82\mu_p$. The χ^2 from these fits are not particularly good, especially for the large angle data set. However our fit to the low angle data set appears no worse than the fits made to the UCLA experiment. Our data are plotted against the MIT theory in figures 6.7, 6.8 and 6.9. We also present a plot of the MIT theory as fitted to the UCLA experiment, figure 6.10; these data are from their G7 counter, which is in essentially the same position as our NaI(Tl) array. Finally, we have formed the same χ^2 requiring that $E_\gamma < 100MeV$. For the low data set, the minimum value of $\chi^2 = 0.94$ and occurs at $\mu_\Delta = 2.75$. However, the fit to the high data set is just as bad as the previous fit.

When comparing with the MIT theory it is important to note that there are uncertainties in the off shell treatment, and ambiguities in the parameterization of the $\pi N \Delta$ vertex which make it impossible to pin μ_Δ down to an accuracy[51] better than $\pm 0.25\mu_p$. Also, the model

---

[51] Shunzo Kumano, Nucleon Substructure and Nuclear Properties, MIT Ph.D. Thesis (1985).

is valid only for $E_\gamma < 116 MeV$ and in comparing to our data, $E_\gamma = 100 MeV$ might be a more realistic limit. This behavior can be clearly seen in our comparisons to the MIT theory. For $E_\gamma > 116$ MeV, the MIT cross–section is rising, a clearly unphysical effect as the energy of the photon is kinematically limited to be under 140.MeV in our geometry. This rising cross–section arises from the bremsstrahlung from the self–energy loop in the Δ propagator, a term which is needed to accurately calculate the lower energy cross–sections, (see figure 2.6).

When one looks at how well the MIT theory fit the UCLA data, they were able to do a very good job for $\alpha_\gamma = 120°, \beta_\gamma = \pm 36°, \theta_\pi = -50°$; when they fit at $\beta_\gamma = 0°$ the results at $\alpha_\gamma = 120°$ were somewhat worse. However, when they looked at other photon counters in the UCLA experiment, $(\alpha_\gamma = (140°, 160°)$, the fits became progressively worse, and the behavior was similar to what we saw in our high angle data set. We note that when one transforms to the center of mass frame, our $(\alpha_\gamma = 120°, \theta_\pi = -85°)$ and the UCLA $(\alpha_\gamma = 160°, \theta_\pi = -50°)$ have the final state particles in the same relative positions. In the center of mass, our photon energy, and the UCLA energy are equal, our pion momentum and the UCLA pion momentum are equal, and the angle between the pion and photon are the same. This is not to say that they are the same position, but it is interesting to note that the MIT theory fails to fit both data sets in essentially the same way. This may be indicative of the off mass shell effects being wrong in this region.

In quoting a value for μ_Δ, it is not really possible to make use of the high angle data set, a χ^2 of 6.42 is meaningless. We are forced to extract a value of μ_Δ exclusively from the low angle data set. From this set alone, we then get that $\mu_\Delta = (2.80 \pm 0.25)\mu_p$. To this we have to add the theoretical uncertainty of $\pm 0.25\mu_p$. This theoretical error is partly a systematic shift due the the ambiguity in the choice of the parameterization of the $\pi N \Delta$ vertex. As such it is not correct to add it in quadrature with our experimental uncertainty, but instead we are forced to add it linearly. This then results in $\mu_\Delta = (2.8 \pm 0.5)\mu_p$. This value is consistent with the result quoted by the MIT group when they fit their theory to the UCLA data, $\mu_\Delta = (3.0 \pm 0.5)\mu_p$. However, these values of μ_Δ are entirely dependent upon the validity of the MIT theory.

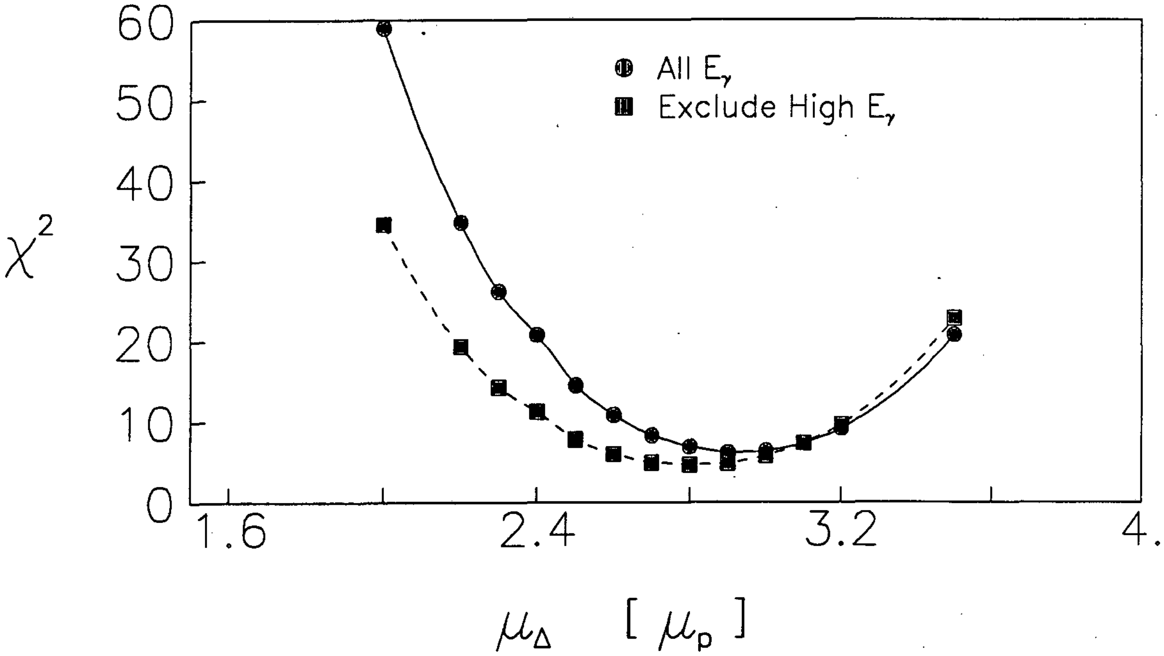

Figure 6.4: A plot of χ^2 versus μ_Δ for $55° < \theta_\pi < 95°$.

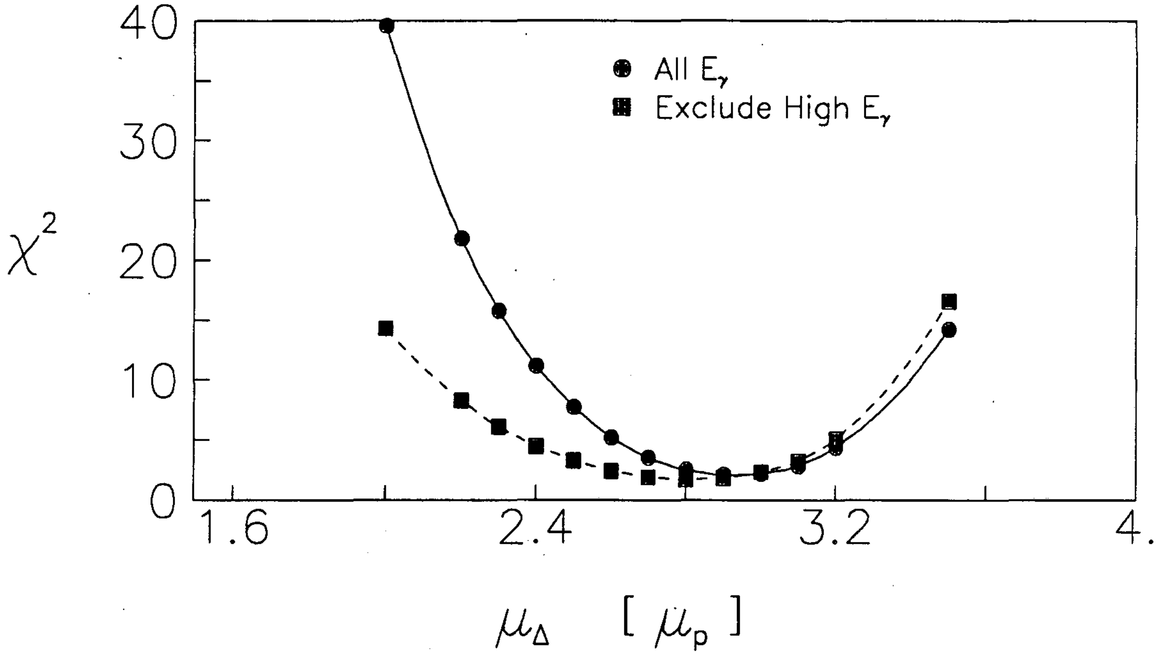

Figure 6.5: A plot of χ^2 versus μ_Δ for $55° < \theta_\pi < 75°$.

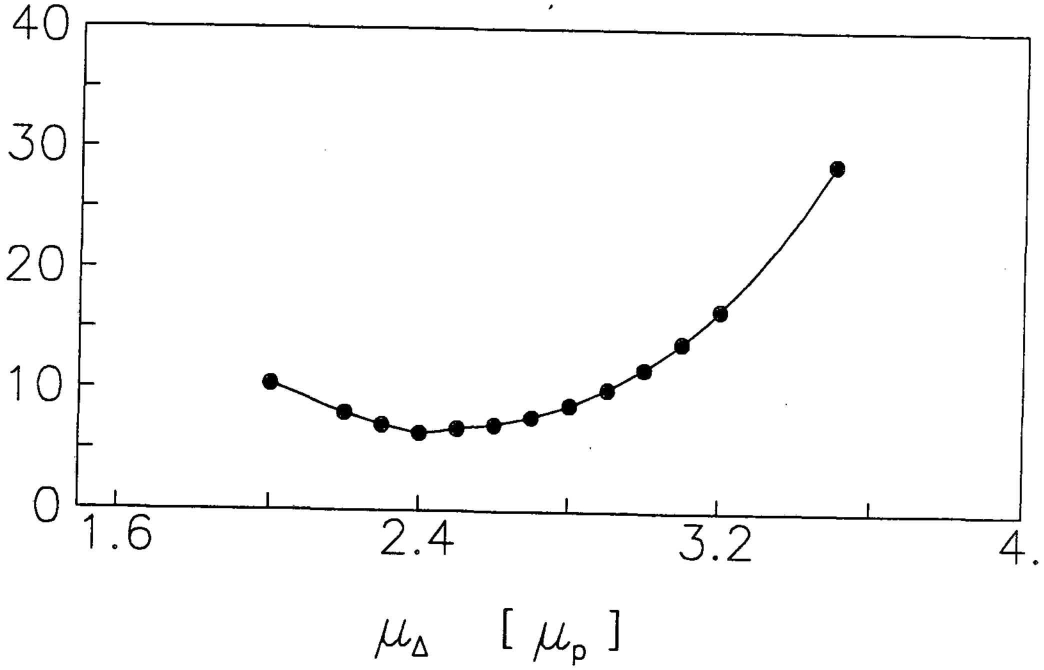

Figure 6.6: A plot of χ^2 versus μ_Δ for $75° < \theta_\pi < 95°$.

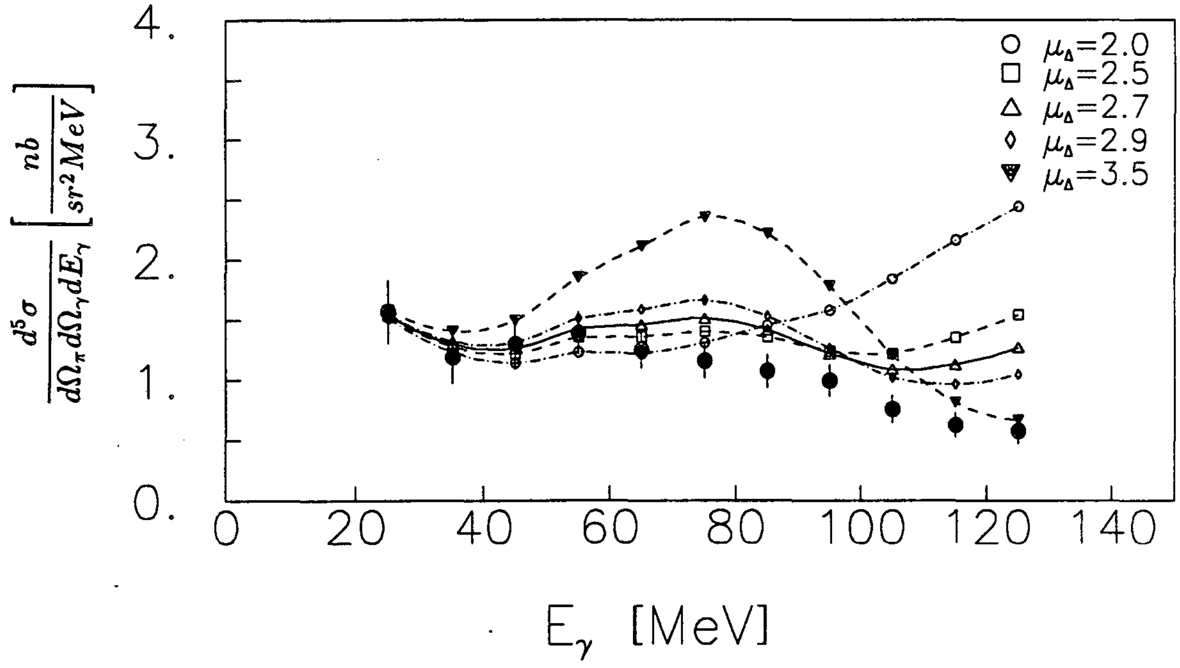

Figure 6.7: Our data plotted against the MIT theory for several values of μ_Δ; $55° < \theta_\pi < 95°$.

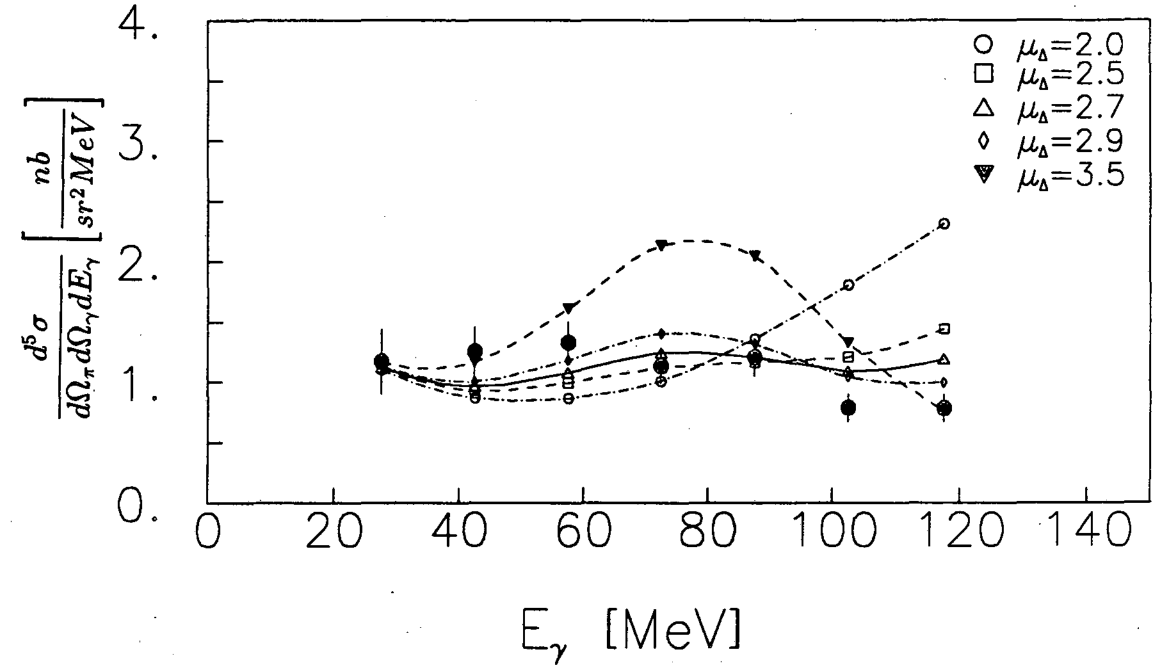

Figure 6.8: Our data plotted against the MIT theory for several values of μ_Δ; $55° < \theta_\pi < 75°$.

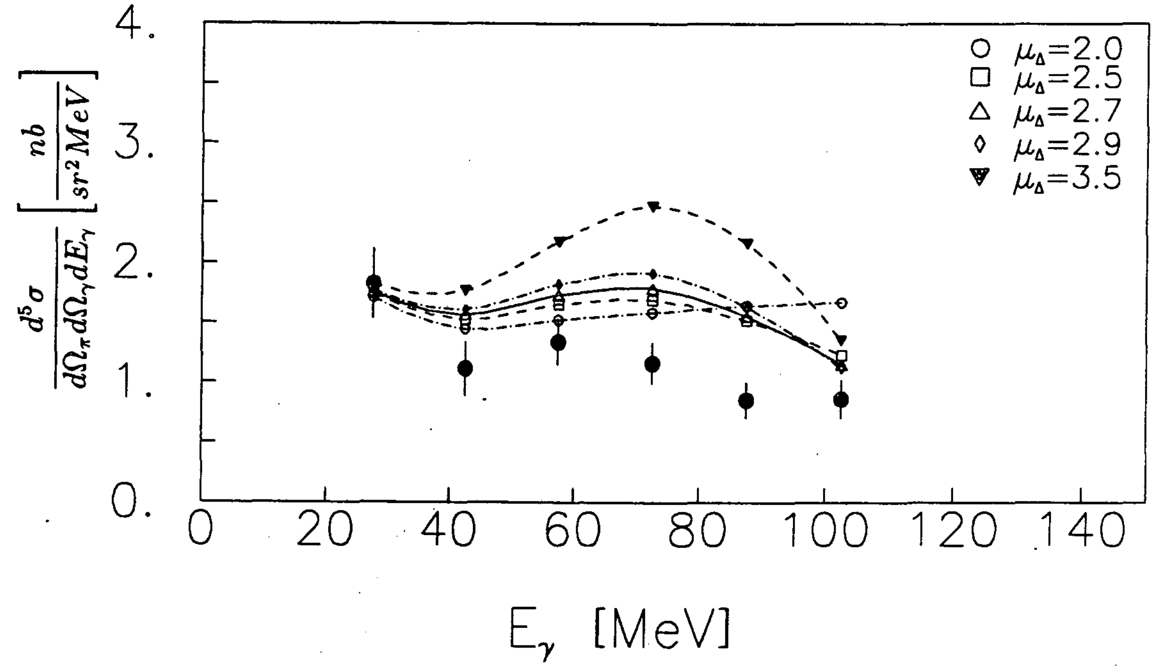

Figure 6.9: Our data plotted against the MIT theory for several values of μ_Δ; $75° < \theta_\pi < 95°$.

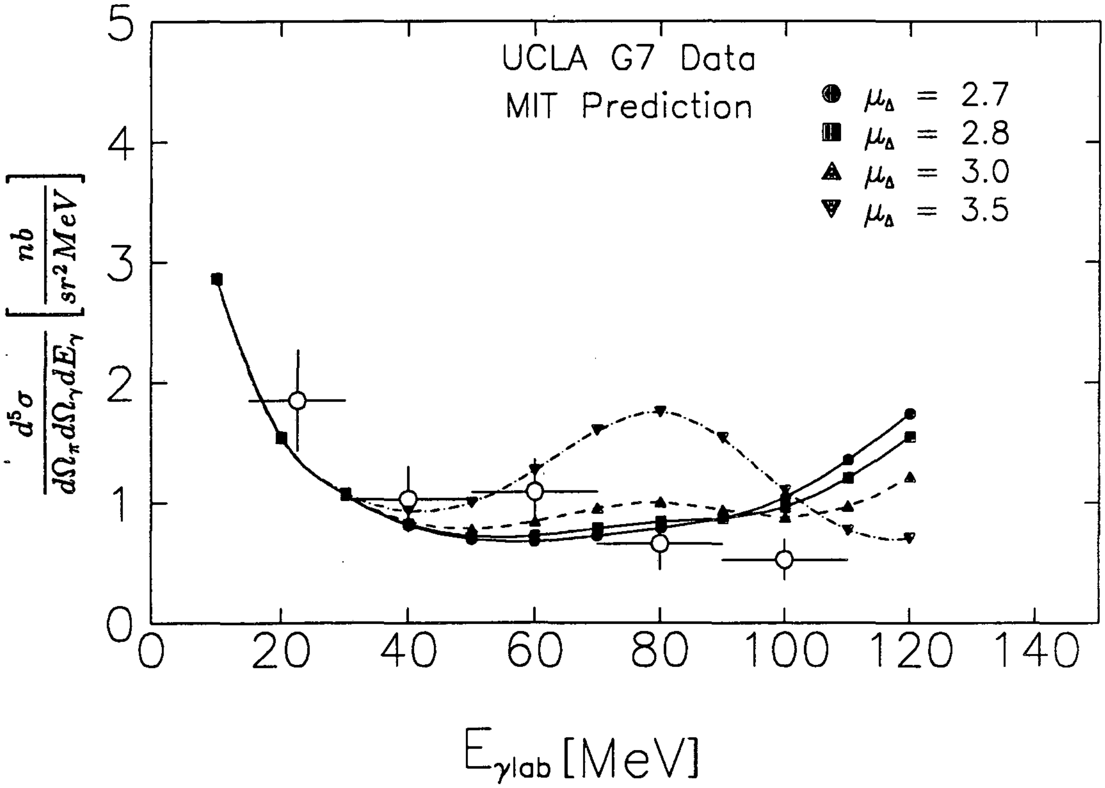

Figure 6.10: UCLA data plotted against the MIT theory for several values of μ_Δ. The data is from the UCLA G7 counter.

Appendix A

Principal Components Analysis

In the Principal Component Analysis, one starts with a set of n measurements of m quantities which are expressed as n vectors, $\vec{x}_\alpha$.

$$\vec{x}_\alpha = \begin{pmatrix} x_{\alpha 1} \\ x_{\alpha 2} \\ \vdots \\ x_{\alpha m} \end{pmatrix}$$

One then wants to find a new set of coordinates, ξ_j such that one has successively maximized the quantity

$$\overline{\xi}_j^2 = \frac{1}{n} \sum_{\alpha}^{n} \xi_{\alpha j}^2 \qquad \text{(A.1)}$$

for $j = 1, 2, \cdots, m$. What one is doing is obtaining a set of orthogonal coordinates which are pointing in the most significant to the least significant *directions* in the data sample. The new set of coordinates, ξ_j are useful for fitting functions to the data sample, and locating either tracks or unusual events in the data sample.

When fitting functions to the data set, one would not need to include the complete set of ξ_j, some subset of the most significant coordinates can be used. In track finding one makes use of the fact that 6 parameters will uniquely identify every track, ($\vec{x}$ and $\vec{p}$ at some point on the track). If one then has more than 6 measurements, the residual sum

$$\sum_{j=7}^{m} \xi_j^2$$

will be very small for a good track, and in general quite large for a random data set. One then makes some cut on the residual and a very efficient track recognition routine is obtained.

In order to perform the transformation to Principal Components, it is necessary to determine what the transformation is. One defines $\vec{\xi}$ as

$$\vec{\xi} = \mathcal{R}(\vec{x} - \vec{a})$$

where $\mathcal{R}$ is a rotation matrix and $\vec{a}$ is a constant displacement. In solving for $\mathcal{R}$ and $\vec{a}$ one needs to maximize equation A.1 . For $\vec{a}$ this gives that

$$\frac{d}{da_i}\sum_{\alpha}^{n} \xi_{\alpha j}^2 = \frac{d}{da_i}\sum_{\alpha}^{n}\left[\sum_{k}^{m} r_{jk}\left(x_{\alpha k} - a_k\right)\right]^2 = 0 \qquad \text{(A.2)}$$

To satisfy equation A.2 it is necessary that $\sum(x_{\alpha k} - a_k) = 0$, or $a_k = \overline{x}_k$, where

$$\overline{x}_i = \frac{1}{n}\sum_{\alpha}^{n} x_{\alpha i}$$

From this one sees that the new origin for the measurements is just the center of gravity of all the measurements. For convenience, one now defines a shifted set of coordinates $\vec{u}_i$ such that

$$\vec{u} = \vec{x} - \vec{a}$$

$\vec{\xi}$ can now be written as

$$\vec{\xi} = \mathcal{R}\vec{u}$$

and because $\mathcal{R}$ is a rotation, $\sum_i^m r_{ij}^2 = 1$. In order to satisfy the condition on $\mathcal{R}$, one uses Lagrange multipliers λ_j to maximize equation A.1 .

$$\begin{aligned}
\frac{d}{dr_{ij}}\left[\sum_{\alpha}^{n} \xi_{\alpha j}^2 - \lambda_j \sum_{k}^{m} r_{kj}^2\right] &= 0 \\
\frac{d}{dr_{ij}}\left[\sum_{\alpha}^{n}\left(\sum_{k}^{m} u_{\alpha k} r_{jk}\right)^2\right] &= 2\lambda_j r_{ij} \\
\frac{d}{dr_{ij}}\left[\sum_{\alpha}^{n}\sum_{k}^{m}\sum_{l}^{m}\left(u_{\alpha k} u_{\alpha l} r_{jk} r_{jl}\right)\right] &= 2\lambda_j r_{ij} \\
\sum_{\alpha}^{n}\sum_{k}^{m} u_{\alpha k} u_{\alpha i} r_{jk} &= \lambda_j r_{ij}
\end{aligned}$$

This can be rewritten in matrix notation as:

$$\mathcal{A}\mathbf{r}_j = \lambda_j \mathbf{r}_j \qquad \text{(A.3)}$$

The matrix $\mathcal{A}$ is the dispersion matrix, and is given by

$$a_{ij} = \frac{1}{n}\sum_{\alpha}^{n}(x_{\alpha i} - \overline{x}_i)(x_{\alpha j} - \overline{x}_j)$$

The vectors r_j are just the eigenvectors of the dispersion matrix, and the λ_j are their eigenvalues. It can also be demonstrated that the eigenvalues $\lambda_j = \overline{\xi}_j^2$, the quantity that was maximized in equation A.1 . So, we have obtained that the elements of the rotation matrix are just the eigenvectors of equation A.3 .

Appendix B

Polynomial Fitting to Monte–carlo Data

In fitting the monte–carlo data for the pion spectrometer, one wants to obtain a set of polynomials whose arguments are the fired wires in the 13 wire planes of the spectrometer and whose results are: p_π,θ_π, ϕ_π, target$_y$ and target$_z$. In principle six wires should completely describe each track; 13 wires should provide much redundant information. Because fitting a polynomial with 13 free parameters takes about an order of magnitude more time than fitting one with 6 free parameters, one would like to use some subset of the 13 parameters which have as much information about the track as possible. This set of parameters is just some subset of the 13 components obtained from a *principal components analysis* performed on the monte–carlo data sample, (see appendix A).

In fitting a quantity Q, one forms a polynomial such that:

$$Q_\alpha = \sum_i^{n_1}\sum_j^{n_2}\sum_k^{n_3}\cdots\sum_l^{n_m}[P_i(\xi_{\alpha 1})\cdot P_j(\xi_{\alpha 2})\cdot P_k(\xi_{\alpha 3})\cdots P_l(\xi_{\alpha m})] \qquad \text{(B.1)}$$

Where P_n are a set of orthonormal polynomials, (Chebychev, Hermite or Legendre) and $\xi_{\alpha m}$ are the principal components obtained from the α'th measurement. In forming these polynomials, there is a general rule of thumb that one should have at least 50 data points for each accepted function in equation B.1[52]. Because the principal components are ordered

---

[52] H. Wind **Principal Component Analysis and its Applications to Track Finding** published in **Formulae and Methods in Experimental Data Evaluation, Vol.3** European Physical Society (1984)

from most significant to least significant, the values of n_i approximately obey the relation:

$$n_1 \geq n_2 \geq n_3 \geq \cdots \geq n_m$$

The choice of polynomials is also another critical factor. For one parameter fits it can be shown[53] that Chebychev polynomials give the best possible fit to a data sample; for multidimensional fits it is not clear that a product of Chebychev polynomials as in equation B.1 would give the best fit, this is just assumed to be true. However when using Chebychev polynomials there is a problem when one tries to extrapolate beyond the data sample; Chebychev polynomials are only defined over the range $(-1, +1)$ and the errors encountered blow up at the boundaries of the data set. One can try to correct this problem by weighting the data sample towards the boundaries but this doesn't always work. Another solution would be to use a set of polynomials which are not bound to some small interval. Hermite polynomials are defined over the interval $(-\infty, +\infty)$ and as such can provide a possible fix to the problem.

In performing the fits to the data, the program ERIKA loops over all the allowed functions and computes a reduction to χ^2 for each. If the calculated reduction is greater than some minimum value, the function is accepted and the new χ^2 computed. One needs to loop over the data set several times to get a good fit and in doing so it is not true that the same minimum value should be used in each pass. During the first loop over the data, one wants only to accept the most significant functions. If the minimum reduction to χ^2 is too small it is possible to accept one function, while a later one in the list would actually give a larger reduction to χ^2. When this happens one would get several additional functions accepted during later passes which just corrects for the bad choice. To reduce this problem, ERIKA has a very tight χ^2 reduction during the first pass which gradually gets reduced during subsequent passes.

When fitting a particular function, one wants to generate monte–carlo data whose acceptance limits are beyond those normally encountered in the real data sample. This allows the resulting functions to interpolate rather than extrapolate. In these data sets, one pretends that the wire chambers are about 20% bigger than the real chambers, and then tries to weight the events towards the boundary of the accepted phase space. Unfortunately, for

---

[53] Kendall E. Atkinson **An Introduction to Numerical Analysis** John Wiley and Sons, New York (1976), chapter 4

the momentum fit this does not work all that well. There is a minimum momentum that can traverse the spectrometer magnet without being turned around. Because one is not able to generate events below this minimum momentum, the momentum is fit with products of Hermite polynomials, all other quantities are fit with Chebychev polynomials. Table B.1 summarizes the parameters used in the fitting of each quantity.

Quantity	Polynomial used	Number of pr. comp.	Number of terms used	Residual χ^2
p_π	Hermite	8	60	1.87 MeV/c
θ_π	Chebychev	8	45	0.001°
ϕ_π	Chebychev	8	28	0.001°
target_y	Chebychev	8	40	0.02cm
target_z	Chebychev	8	44	0.02cm

Table B.1: Fit Parameters

Appendix C

The Triangle Equations

The *triangle equations* are a set of linear equations which allow one to determine the size of a triangle formed by the wires in a wire chamber. One inputs the three fired wires, and the height of the triangle in *mm* is returned. One can also set the size of a triangle to zero and determine what a missing wire should be. The equations are obtained from simple planar geometry and are only repeated here as the author is never able to find them when they are needed.

Before proceeding, a table that lists the measured positions of the wires in each of the chambers used is presented. In principle the three two meter chambers are identical, but of course this is not the case. In order to avoid confusion each of the chambers has been given a name. Zoe, Yolanda are the small chambers close two the target, Mildred is a one meter long chamber used with the unpolarized target and Adele, Berthe and Cunegonde are the three two meter long chambers.The wire spacing and rotation angle in each plane has been measured by Andreas Bosshard and is presented in table C.1. In order to use table C.1, one needs to know the following definitions:

- α is the angle between the vertical side of a chamber and the wires in a plane.
- s is the spacing between wires in a given plane.
- Δ is the distance from wire number '0' to an outside corner of the chamber.
- l is the length of a wire chamber.
- h is the height of a wire chamber.

- *Center* is the distance from wire number '0' to the center of a wire plane, distance measured normal to the wires.

Chamber	Plane	α [deg]	s [mm]	Δ [mm]	*Center* [mm]	error [mm](1σ)
Zoe	2X	0.00	1.9987	68.16	142.84	0.09
Yolande	4X	0.00	1.9987	68.07	142.93	0.19
Mildred	MID2	30.10	1.9964	279.17	430.72	0.12
	MID6	180.00	1.9996	-2277.44	1662.69	0.15
	MID4	150.04	2.0010	-1842.70	1487.38	0.50
Berthe	4A	149.82	1.9975	-1812.25	957.70	0.24
	6A	180.00	2.0011	-2266.58	1071.58	0.09
	2A	30.30	1.9951	253.63	957.23	0.16
Adele	4	149.91	1.9985	-1814.87	958.89	0.35
	6	180.00	2.0009	-2266.40	1071.40	0.03
	2	30.24	1.9953	254.94	956.23	0.18
Cunegonde	4B	149.98	1.9994	-1816.86	959.78	0.38
	6B	180.00	2.0001	-2266.11	1071.11	0.13
	2B	30.25	1.9979	252.92	958.20	1.02

Table C.1: Measured wire positions in the chambers

In order to derive the triangle equations, one starts with the equations of three lines which fall on top of the wires. These wires are shown in figure C.1 as w_1, w_2 and w_3. (Note the unusual coordinate system in figure C.1. The x–axis points to the left, and the y–axis points down.)

$$y_1 = m_1 \cdot x_1 + b_1 \tag{C.1}$$

$$y_2 = m_2 \cdot x_2 + b_2 \tag{C.2}$$

$$y_3 = m_3 \cdot x_3 + b_3 \tag{C.3}$$

These equations are fine unless one of the wires is vertical or horizontal. In such a cases one can use the much simpler equations:

$$\begin{aligned} y_i &= b_i \\ x_j &= a_j \end{aligned}$$

From figure C.1 we obtain that $m = \tan\theta$ and $b = \alpha\cdot\sec\theta$. The quantity α_i in figure C.1 is given as $\alpha_i = s_i\cdot(\text{℄}_i - w_i)$ where s_i is the wire spacing, w_i is the wire number and ℄_i is the wire number at the center of the chamber. In this way equations C.1,C.2 and C.3 can be rewritten as

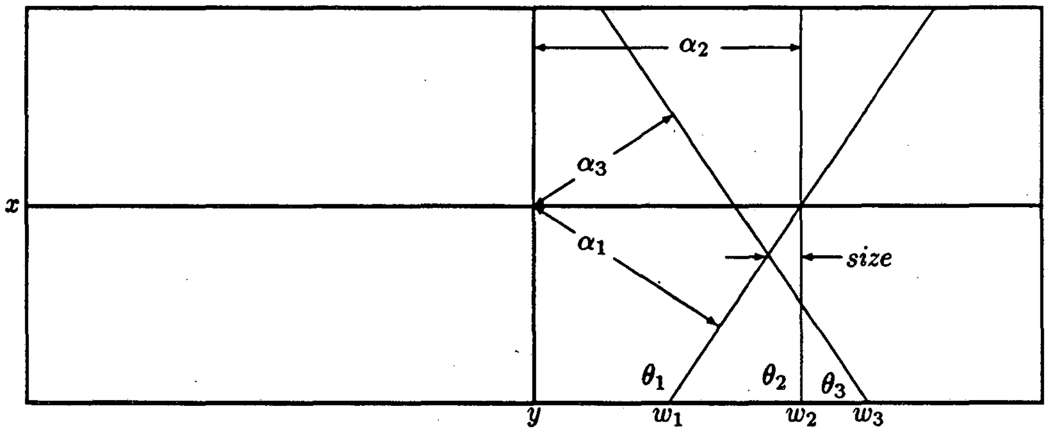

Figure C.1: Triangle in a wire chamber

$$\begin{aligned} y_1 &= \tan\theta_1\cdot x_1 + \alpha_1\cdot\sec\theta_1 && \text{(C.4)} \\ x_2 &= \alpha_2\cdot\sin\theta_2 && \text{(C.5)} \\ y_3 &= \tan\theta_3\cdot x_3 + \alpha_3\cdot\sec\theta_3 && \text{(C.6)} \end{aligned}$$

assuming that $\theta_2 = \pm 90°$. The triangle size is then defined as the distance from the point where w_1 and w_3 cross to w_2. To get this distance, one equates y_1 and y_3. This giving:

$$\tan\theta_1\cdot x + \alpha_1\cdot\sec\theta_1 = \tan\theta_3\cdot x + \alpha_3\cdot\sec\theta_3$$

which solving for x yields:

$$x = \frac{\alpha_3\cdot\sec\theta_3 - \alpha_1\cdot\sec\theta_1}{\tan\theta_1 - \tan\theta_3}$$

The difference between the above x and x_2 then gives the size of the triangle.

$$size = \frac{\sec\theta_1}{\tan\theta_1 - \tan\theta_3}\cdot\alpha_1 + \alpha_2\cdot\sin\theta_2 + \frac{\sec\theta_3}{\tan\theta_3 - \tan\theta_1}\cdot\alpha_3$$

This equation is then written in a form:

$$size = 2\cdot c_1\cdot(\text{¢}_1 - w_1) + 2\cdot c_2\cdot(\text{¢}_2 - w_2) + 2\cdot c_3\cdot(\text{¢}_3 - w_3) \tag{C.7}$$

There is also the situation where one plane is horizontal and one plane is vertical. In this situation it can be shown that the triangle equation can be written as:

$$size = \alpha_1 \cdot \sin\theta_3 - \alpha_2 \cdot \cos\theta_2 \cos\theta_3 + \alpha_3$$

where plane one contains the vertical wires and plane two contains the horizontal wires. The *size* in this situation is horizontal width of the triangle. Finally, if one has a horizontal and no vertical plane where plane one is the horizontal plane, then the triangle equation is:

$$size = \alpha_1 \cdot \cos\theta_1 + \frac{\tan\theta_3 \sec\theta_2}{\tan\theta_2 - \tan\theta_3}\alpha_2 + \frac{\tan\theta_2 \sec\theta_3}{\tan\theta_3 - \tan\theta_2}\alpha_3$$

where the *size* is the height of the triangle in *mm*. One can then take the values for wire spacing, angles and centers of chambers from table C.1,one obtains the set of coefficients as seen in table C.2. Note that the θ's used are not necessarily the same as those in table C.1 as the readout direction is included in this angle. One can also solve equation C.7 for missing wires and obtain a set of three equations per chamber that allow one to always

chamber	θ_1	θ_2	θ_3	c_1	c_2	c_3
Mildred	-59.90	90.00	59.96	-0.5762	-0.9998	0.5786
Berthe	-59.82	-90.00	59.70	0.5791	-1.0006	-0.5763
Adele	-59.91	-90.00	59.76	0.5792	-1.0005	-0.5757
Cunegonde	-59.98	-90.00	59.75	0.5800	-1.0001	-0.5755

Table C.2: Triangle size coefficients in the large chambers

chamber	θ_1	θ_2	θ_3	θ_4	c_1	c_2	c_3	c_4
Zoe	-90.	0.			.7067	-.7067	.9994	
Yolande			135.	45.	-.9994		.7067	.7067
						-.9994	.7067	-.7067

Table C.3: Triangle size coefficients in the small chambers calculate the third wire. These equations are then written as

$$\begin{aligned} w_1 &= \frac{c_2}{c_1}\cdot(\text{¢}_2 - w_2) + \frac{c_3}{c_1}\cdot(\text{¢}_3 - w_3) + \text{¢}_1 \\ w_2 &= \frac{c_1}{c_2}\cdot(\text{¢}_1 - w_1) + \frac{c_3}{c_2}\cdot(\text{¢}_3 - w_3) + \text{¢}_2 \\ w_3 &= \frac{c_2}{c_1}\cdot(\text{¢}_3 - w_1) + \frac{c_2}{c_3}\cdot(\text{¢}_2 - w_2) + \text{¢}_3 \end{aligned}$$

Finally, a related topic to triangle sizes is the x and y coordinates of a hit. When one has a vertical or horizontal wire, then the coordinate should be determined solely from that wire. When one of those wires aren't present, then it is necessary to use information from the slanted planes. To calculate the position one then takes an average of the positions of the three intersection points of wire pairs as seen in figure C.1. In doing this, one wants to express x and y as:

$$\begin{aligned} x &= \frac{1}{3}(x_{12} + x_{23} + x_{13}) \\ y &= \frac{1}{3}(y_{12} + y_{23} + y_{13}) \end{aligned}$$

Where x_{ij} and y_{ij} are determined from the line equations in a given chamber, (C.4, C.5 and C.6). For the large chambers in this experiment where plane 2 is a 90° plane, one has that:

$$\begin{aligned} x_{12} &= \alpha_2 \cdot \sin\theta_2 \\ y_{12} &= \alpha_1 \cdot \sec\theta_1 + \alpha_2 \cdot \tan\theta_1 \cdot \sin\theta_2 \\ x_{23} &= \alpha_2 \cdot \sin\theta_2 \\ y_{23} &= \alpha_2 \cdot \tan\theta_3 \cdot \sin\theta_2 + \alpha_3 \cdot \sec\theta_3 \\ x_{13} &= \alpha_1 \cdot \frac{\sec\theta_1}{\tan\theta_3 - \tan\theta_1} + \alpha_3 \cdot \frac{\sec\theta_3}{\tan\theta_1 - \tan\theta_3} \\ y_{13} &= \alpha_1 \cdot \frac{\tan\theta_3 \sec\theta_1}{\tan\theta_3 - \tan\theta_1} + \alpha_3 \cdot \frac{\tan\theta_1 \sec\theta_3}{\tan\theta_1 - \tan\theta_3} \end{aligned}$$

One then wants to express the these equations in terms of a set of A, B and C coefficients for each chamber.

$$\begin{aligned}
x_{12} &= 2 \cdot [A_1 \cdot (\text{¢}_1 - w_1) + A_2 \cdot (\text{¢}_2 - w_2)] \\
y_{12} &= 2 \cdot [A_3 \cdot (\text{¢}_1 - w_1) + A_4 \cdot (\text{¢}_2 - w_2)] \\
x_{23} &= 2 \cdot [B_1 \cdot (\text{¢}_2 - w_2) + B_2 \cdot (\text{¢}_3 - w_3)] \\
y_{23} &= 2 \cdot [B_3 \cdot (\text{¢}_2 - w_2) + B_4 \cdot (\text{¢}_4 - w_4)] \\
x_{13} &= 2 \cdot [C_1 \cdot (\text{¢}_1 - w_1) + C_2 \cdot (\text{¢}_3 - w_3)] \\
y_{13} &= 2 \cdot [C_3 \cdot (\text{¢}_1 - w_1) + C_4 \cdot (\text{¢}_3 - w_3)]
\end{aligned}$$

From this, one can obtain the values of A, B and C for each of the chambers. The coefficients given in the tables give the xy position in *mm*. Finally, in the two small chambers a slightly

chamber	A_1	A_2	A_3	A_4
Mildred	0.0000	–0.9998	1.9904	1.7248
Berthe	0.0000	0.9878	1.9867	–1.7205
Adele	0.0000	0.9993	1.9931	–1.7266
Cunegonde	0.0000	0.9997	1.9967	–1.7307

Table C.4: The A coefficients for the large chambers.

chamber	B_1	B_2	B_3	B_4
Mildred	–0.9998	0.0000	–1.7289	1.9986
Berthe	0.9978	0.0000	1.7122	1.9772
Adele	0.9993	0.0000	1.7162	1.9809
Cunegonde	0.9997	0.0000	1.7148	1.9829

Table C.5: The B coefficients for the large chambers.

chamber	C_1	C_2	C_3	C_4
Mildred	0.5762	-0.5786	0.9964	0.9981
Berthe	0.5751	-0.5763	0.9922	0.9910
Adele	0.5792	-0.5758	0.9935	0.9937
Cunegonde	0.5755	-0.5800	0.9945	0.9960

Table C.6: The C coefficients for the large chambers.

different set of equations apply. These are derived from the following equations:

$$\begin{aligned}
x_{12} &= \alpha_1 \cdot \sin\theta_1 \\
y_{12} &= \alpha_2 \cdot \cos\theta_2 \\
x_{13} &= \alpha_1 \cdot \sin\theta_1 \\
y_{13} &= \alpha_1 \cdot \sin\theta_1 \tan\theta_3 + \alpha_3 \cdot \sec\theta_3 \\
x_{14} &= \alpha_1 \cdot \sin\theta_1 \\
y_{14} &= \alpha_1 \cdot \sin\theta_1 \tan\theta_4 + \alpha_3 \cdot \sec\theta_4 \\
x_{23} &= \alpha_2 \cdot \cos\theta_2 \cot\theta_3 - \alpha_3 \cdot \csc\theta_3 \\
y_{23} &= \alpha_2 \cdot \cos\theta_2 \\
x_{24} &= \alpha_2 \cdot \cos\theta_2 \cot\theta_3 - \alpha_4 \cdot \csc\theta_4 \\
y_{24} &= \alpha_2 \cdot \cos\theta_2 \\
x_{34} &= \alpha_3 \cdot \frac{\sec\theta_3}{\tan\theta_4 - \tan\theta_3} + \alpha_4 \cdot \frac{\sec\theta_4}{\tan\theta_3 - \tan\theta_4} \\
y_{34} &= \alpha_3 \cdot \frac{\csc\theta_3}{\cot\theta_3 - \cot\theta_4} + \alpha_4 \cdot \frac{\csc\theta_4}{\cot\theta_4 - \cot\theta_3}
\end{aligned}$$

From these equations, one can define three sets of A, B and C coefficients depending on which three planes on examines. These are presented in the last three tables of this appendix.

combination	A_1	A_2	A_3	A_4
123	-0.9994	0.0000	0.0000	0.9994
124	-0.9994	0.0000	0.0000	0.9994
134	-0.9994	0.0000	0.9994	-1.4133
234	0.9994	-1.4133	0.9994	0.0000

Table C.7: The three sets of A coefficients for the small chambers.

combination	B_1	B_2	B_3	B_4
123	0.9994	1.4133	0.9994	0.0000
124	-0.9994	-1.4133	0.9994	0.0000
134	-0.7067	-0.7067	0.7067	-0.7067
234	-0.7067	-0.7067	0.7067	-0.7067

Table C.8: The three sets of B coefficients for the small chambers.

combination	C_1	C_2	C_3	C_4
123	-0.9994	0.0000	0.9994	-1.4133
124	-0.9994	0.0000	-0.9994	1.4133
134	-0.9994	0.0000	-0.9994	1.4133
234	-0.9994	-1.4133	0.9994	0.0000

Table C.9: The three sets of C coefficients for the small chambers.

Appendix D

Electronic Logic Diagrams

This Appendix contains drawings of the elctronics logic used during data acqusition.

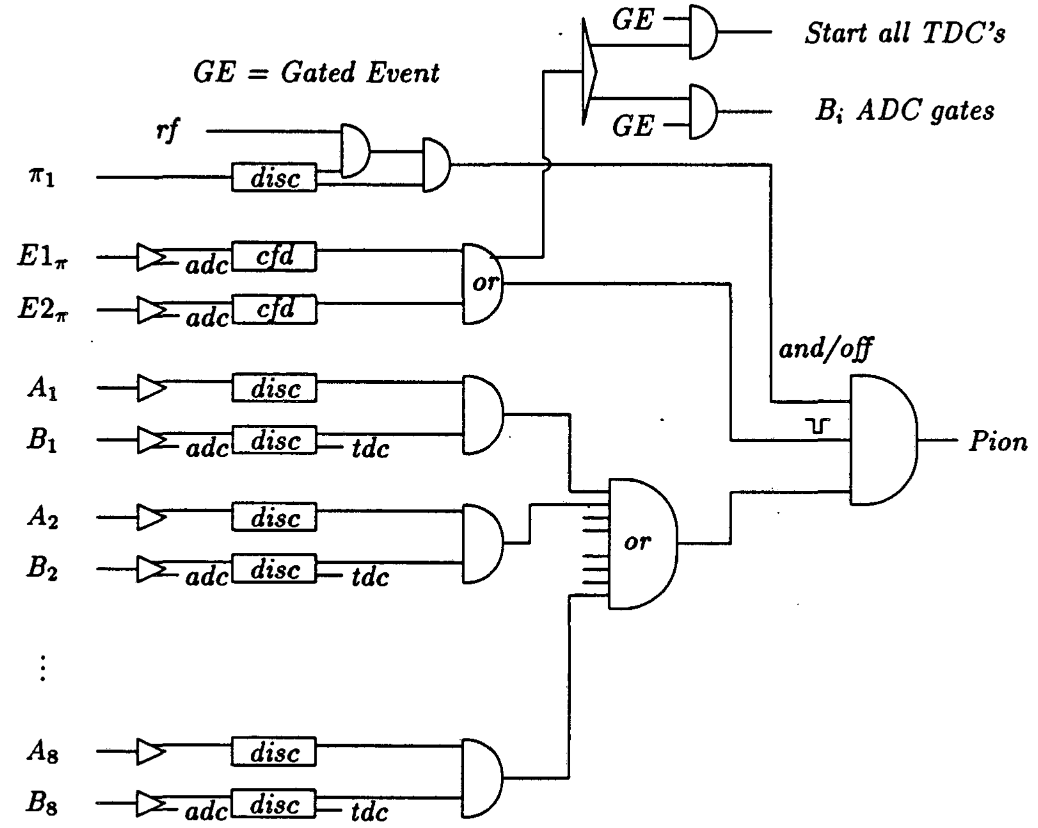

Figure D.1: Trigger Electronics of the Pion Spectrometer

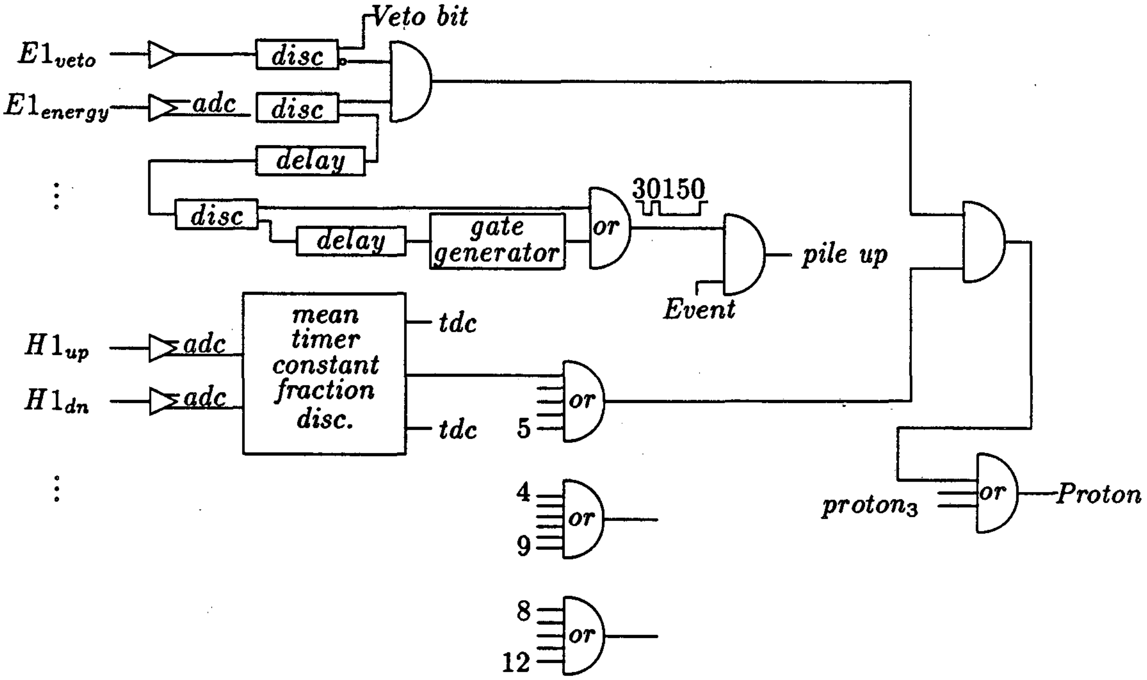

Figure D.2: Trigger Electronics of the Proton Detector

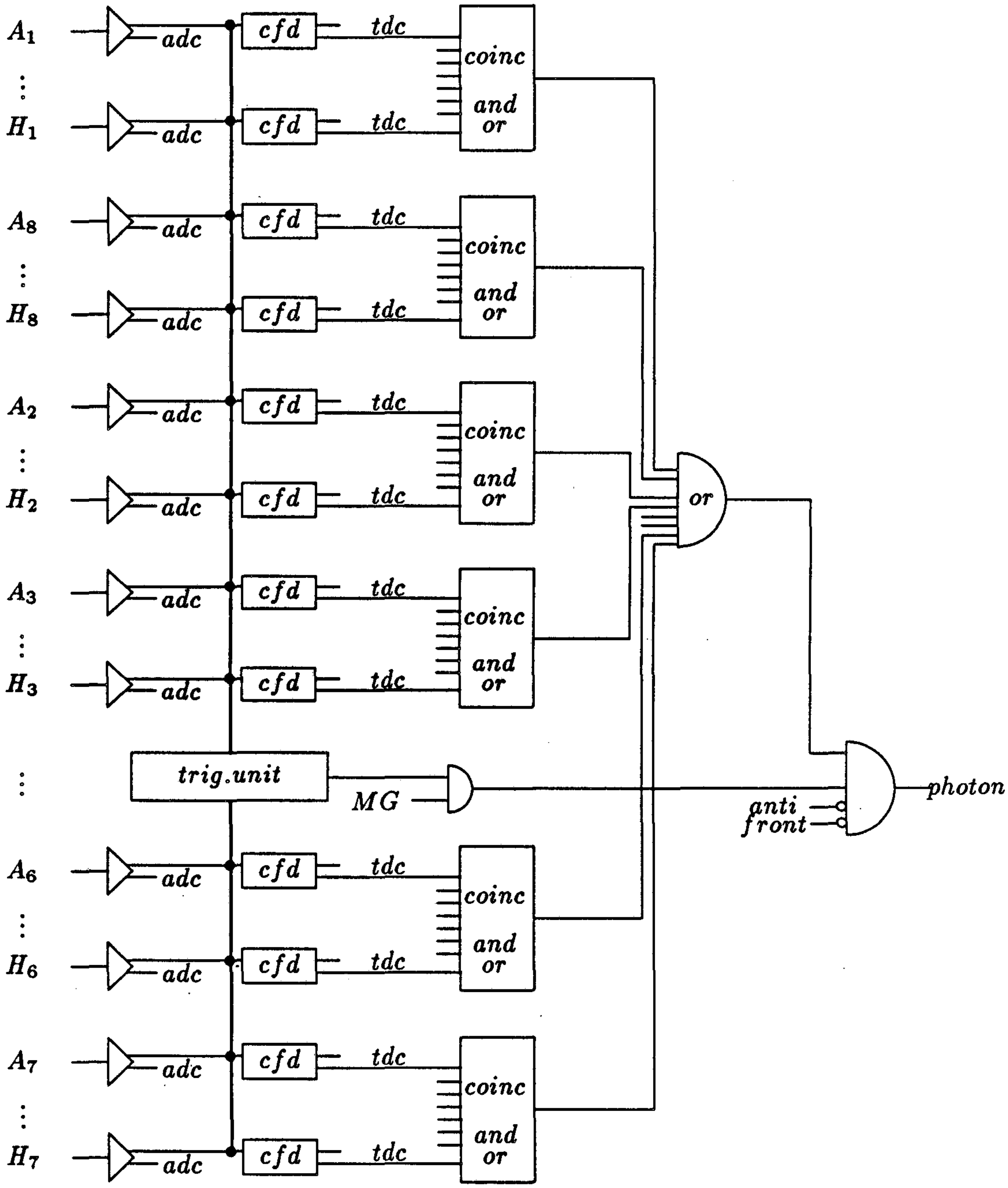

Figure D.3: The NaI Trigger Electronics

Appendix E

Kinematic Fitting of Measured Quantities

In kinematic fitting, one takes a set of overconstrained measurements with their associated errors and allows the quantities to vary within their errors in order to best satisfy the equations of constraints. In a general form, one has r possible measurements that can be made on a system. Of these r observables, n are measured. We will call these n values $\vec{\eta}$. The remaining $r-n$ unmeasured values will be called $\vec{x}$. Next, associated with each of the measurements, η_i is an error σ_i. We will put these σ's into an $n \times n$ diagonal matrix G_y such that $G^{-1}_{y[i,j]} = \delta_{ij}\sigma_i^2$. Finally, there are l equations of constraint on the system, $f_i(\vec{\eta},\vec{x}) = 0$ for $i = 1, l$. So, we have the following quantities:

- n measured quantities, η_i given as $\vec{\eta}$.
- $r-n$ unmeasured quantities, x_i given as $\vec{x}$.
- An $n \times n$ error matrix, G_y.
- l equations of constraint, $f_i(\vec{\eta},\vec{x}) = 0$.

We now want to define a χ^2 which we will then minimize under the l constraints.

$$\chi^2 = (\vec{\eta}_0 - \vec{\eta})^T G_y (\vec{\eta}_0 - \vec{\eta})$$

We will also write the equations of constraint as:

$$f_i(\vec{\eta},\vec{x}) \cong f_i(\vec{\eta}_0,\vec{x}_0) + \sum_{j=1}^{n} \frac{\partial f_i}{\partial \eta_j}|_{\eta_0}(\eta_j - \eta_{j0}) + \sum_{j=1}^{r-n} \frac{\partial f_i}{\partial x_j}|_{x_0}(x_j - x_{j0})$$

Now, if we define

$$A = \begin{pmatrix} \frac{\partial f_1}{\partial x_1} & \cdots & \frac{\partial f_1}{\partial x_{r-m}} \\ \vdots & & \vdots \\ \frac{\partial f_l}{\partial x_1} & \cdots & \frac{\partial f_l}{\partial x_{r-m}} \end{pmatrix}$$

$$B = \begin{pmatrix} \frac{\partial f_1}{\partial \eta_1} & \cdots & \frac{\partial f_1}{\partial \eta_n} \\ \vdots & & \vdots \\ \frac{\partial f_l}{\partial \eta_1} & \cdots & \frac{\partial f_l}{\partial \eta_n} \end{pmatrix}$$

$$\vec{C} = \begin{pmatrix} f_1(\vec{\eta}_0, \vec{x}_0) \\ \vdots \\ f_l(\vec{\eta}_0, \vec{x}_0) \end{pmatrix}$$

With these definitions we can write that:

$$\vec{f} = \vec{C} + B(\vec{\eta} - \vec{\eta}_0) + A(\vec{x} - \vec{x}_0)$$

and by defining:

$$\vec{b}_0 = \vec{C} - B\vec{\eta}_0 - A\vec{x}_0$$

we can write the constraints as:

$$\vec{b}_0 + B\vec{\eta} + A\vec{x} = 0$$

We now want to minimize χ^2 with the above constraints. To do so we define a new quantity ζ^2 such that $\zeta^2 = \chi^2 + \vec{\lambda} \cdot \vec{f}$.

$$\zeta^2 = (\vec{\eta}_0 - \vec{\eta})^T G_y (\vec{\eta}_0 - \vec{\eta}) + 2\vec{\lambda}^T(\vec{b}_0 + B\vec{\eta} + A\vec{x})$$

In order to do the minimization,we set the partial derivatives of ζ^2 with respect to $\vec{\eta}$, $\vec{x}$ and $\vec{\lambda}$ equal to zero. We want to derive an iterative procedure for obtaining the minimum of ζ^2. As such, from now on a subscript on a vector will refer to the iteration number, (e.g. $\vec{\eta}_i$ is the value of $\vec{\eta}$ at the i'th iteration.)

$$\frac{\partial \zeta^2}{\partial \vec{\eta}} = 2G_y(\vec{\eta}_0 - \vec{\eta}_i) + 2(\vec{\lambda}^T B)^T \tag{E.1}$$

$$\frac{\partial \zeta^2}{\partial \vec{x}} = 2\vec{\lambda}^T A \tag{E.2}$$

$$\frac{\partial \zeta^2}{\partial \vec{\lambda}} = \vec{b}_0 + B\vec{\eta}_i + A\vec{x}_i \tag{E.3}$$

Equation 1 can be solved for $\vec{\eta}_i$ giving that:

$$\vec{\eta}_i = \vec{\eta}_0 + G_y^{-1} B^T \vec{\lambda} \tag{E.4}$$

We then take equation 3, and substitute the above equation in for $\vec{\eta}_i$. This is then solved to yield $\vec{\lambda}$.

$$\vec{\lambda} = -\underbrace{(BG_yB^T)^{-1}}_{G_B}(A\vec{x}_i + \vec{b}_0 + B\vec{\eta}_0)$$

We can now rewrite equation 2 as $A^T\vec{\lambda} = 0$, and combine with the above equation to give us an expression for $\vec{x}_i$.

$$\vec{x}_i = \vec{x}_{i-1} - (A^T G_B A)^{-1} A^T G_B \vec{C} \tag{E.5}$$

Now using equation 4,5 and the expression for $\vec{\lambda}$, we can generate an iterative expression for $\vec{\eta}_i$.

$$\vec{\eta}_i = \vec{\eta}_0 - G_y^{-1} B^T G_B \left\{ \left[I - A(A^T G_B A)^{-1} A^T G_B \right] \left[\vec{C} + B(\vec{\eta}_0 - \vec{\eta}_{i-1}) \right] \right\} \tag{E.6}$$

The errors in all quantities can now be obtained by calculating the new covariance matrix of the system. For the unmeasured quantities, $\vec{x}$ we can write that:

$$\vec{x} = T \cdot \vec{\eta}_0 + \vec{v}$$

and by taking the derivatives of both sides with respect to $\vec{\eta}_0$, we can obtain an expression for the matrix T.

$$T = -(A^T G_B A)^{-1} A^T G_B \underbrace{\frac{d\vec{C}}{d\vec{\eta}_0}}_{B}$$

The covariance matrix C_x can then be expressed as:

$$C_x = T G_y^{-1} T^T$$

$$C_x = (A^T G_B A)^{-1}$$

To calculate the covariance matrix for the measured quantities, we write that:

$$\vec{\eta} = T\vec{\eta}_0 + T'\vec{x} + \vec{v}'$$

where T and T' can be obtained with the appropriate derivatives.

$$T = -G_y^{-1} B^T G_B \underbrace{\frac{d\vec{C}}{d\vec{\eta}_0}}_{B} + I$$

$$T' = -G_y^{-1} B^T G_B A$$

The covariance matrix for η is then written as

$$C_\eta = T G_y^{-1} T^T + T' C_x T'^T$$

$$C_\eta = G_y^{-1} - G_y^{-1} B^T G_B B G_y^{-1} - G_y^{-1} B^T G_B A (A^T G_B A)^{-1} A^T G_B B G_Y^{-1}$$

For the special case where all quantities are measured, we can write that

$$\vec{\eta}_i = \vec{\eta}_0 - G_y^{-1} B^T G_B [\vec{C} + B(\vec{\eta}_0 - \vec{\eta}_{i-1})$$

and the covariance matrix is given as:

$$C_\eta = G_y^{-1} - G_y^{-1} B^T G_B B G_y^{-1}$$

In the present experiment, we have 12 measured quantities. These can be expressed as the polar form of the three momentum for the incident pion, final state pion, proton and gamma. With these, we can make the association that

$$\begin{aligned}
(p_\pi^{in}, \phi_\pi^{in}, \theta_\pi^{in}) &= (\eta_1, \eta_2, \eta_3) \\
(p_p, \phi_p, \theta_p) &= (\eta_4, \eta_5, \eta_6) \\
(p_\pi, \phi_\pi, \theta_\pi) &= (\eta_7, \eta_8, \eta_9) \\
(p_\gamma, \phi_\gamma, \theta_\gamma) &= (\eta_{10}, \eta_{11}, \eta_{12})
\end{aligned}$$

Along with the measured quantities, there are the four equations of constraint from momentum and energy balance.

$$\begin{aligned}
\eta_1 \sin\eta_3 \cos\eta_2 - \eta_4 \sin\eta_6 \cos\eta_5 - \eta_7 \sin\eta_9 \cos\eta_8 - \eta_{10} \sin\eta_{12} \cos\eta_{11} &= 0 \\
\eta_1 \sin\eta_3 \sin\eta_2 - \eta_4 \sin\eta_6 \sin\eta_5 - \eta_7 \sin\eta_9 \sin\eta_8 - \eta_{10} \sin\eta_{12} \sin\eta_{11} &= 0 \\
\eta_1 \cos\eta_3 - \eta_4 \cos\eta_6 - \eta_7 \cos\eta_9 - \eta_{10} \cos\eta_{12} &= 0 \\
\sqrt{\eta_1^2 + m_\pi^2} + m_p - \sqrt{\eta_4^2 + m_p^2} - \sqrt{\eta_7^2 + m_\pi^2} - \eta_{10} &= 0
\end{aligned}$$

A program KFITTER has been written to allow us to perform this kinematic fit on our data. With this program it is possible to treat up to four of the variables as unmeasured.

LAWRENCE BERKELEY LABORATORY
TECHNICAL INFORMATION DEPARTMENT
UNIVERSITY OF CALIFORNIA
BERKELEY, CALIFORNIA 94720